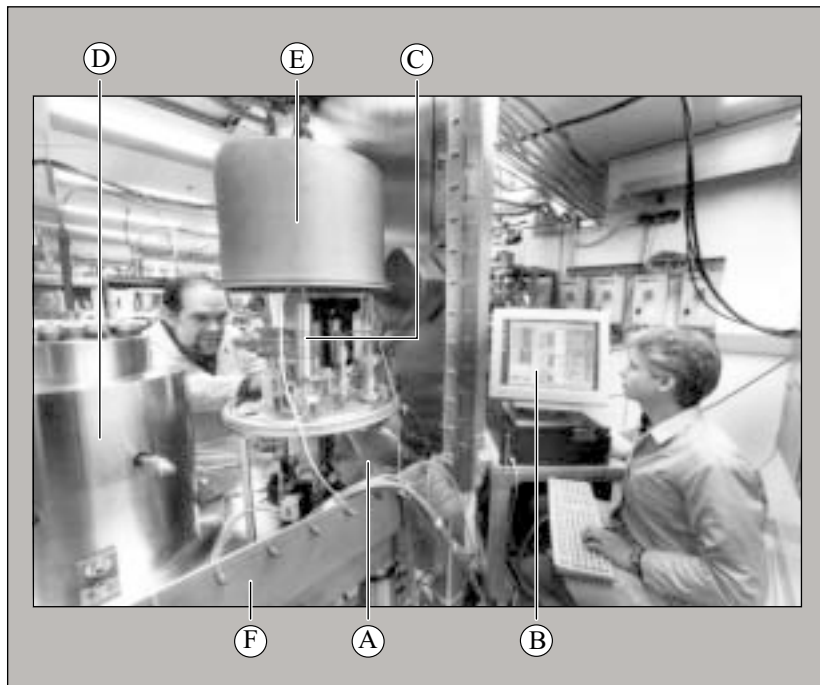


LLE Review

Quarterly Report





About the Cover:

On both the cover photo and the photo to the left, Roger Gram, research engineer, and Jason Hobler, laboratory engineer, perform tests on the high-pressure-filling portion of the cryogenic fill/transfer station, where they recently demonstrated the system's ability to fill targets to high pressures with the required rate of pressure rise. To pressurize targets, deuterium or deuterium-tritium (DT) is first condensed into a small vessel inside chamber (A) and cooled to 10°K. Using the controller (B) the temperature is slowly increased, raising the pressure around the targets inside a permeation cell (not shown). The pressure is monitored by a high-accuracy pressure transducer (C). After the targets have reached a pressure of ~150 atm, the diaphragm compressor (D) is operated, slowly raising the pressure to ~1000 atm. Chamber (E) provides secondary containment for the valves and pressure transducers that control the process. All elements containing 1 atm or more of DT will have secondary containment. The glovebox (F) will provide tertiary containment when DT is introduced.

This report was prepared as an account of work conducted by the Laboratory for Laser Energetics and sponsored by New York State Energy Research and Development Authority, the University of Rochester, the U.S. Department of Energy, and other agencies. Neither the above named sponsors, nor any of their employees, makes any warranty, expressed or implied, or assumes any legal liability or responsibility for the accuracy, completeness, or usefulness of any information, apparatus, product, or process disclosed, or represents that its use would not infringe privately owned rights. Reference herein to any specific commercial product, process, or service by trade name, mark, manufacturer, or otherwise, does not necessarily constitute or imply its endorsement, recommendation, or favoring by

the United States Government or any agency thereof or any other sponsor. Results reported in the LLE Review should not be taken as necessarily final results as they represent active research. The views and opinions of authors expressed herein do not necessarily state or reflect those of any of the above sponsoring entities.

The work described in this volume includes current research at the Laboratory for Laser Energetics, which is supported by New York State Energy Research and Development Authority, the University of Rochester, the U.S. Department of Energy Office of Inertial Confinement Fusion under Cooperative Agreement No. DE-FC03-92SF19460, and other agencies.

Printed in the United States of America
Available from
National Technical Information Services
U.S. Department of Commerce
5285 Port Royal Road
Springfield, VA 22161

Price codes: Printed Copy A03
Microfiche A01

For questions or comments, contact P. B. Radha, *Editor*, Laboratory for Laser Energetics, 250 East River Road, Rochester, NY 14623-1299, (716) 275-1453.

Worldwide-Web Home Page: <http://www.lle.rochester.edu/>

LLE Review



Quarterly Report

Contents

In Brief	iii
Stability Analysis of Directly Driven NIF Capsules	1
Initial Performance of the High-Pressure DT-Filling Portion of the Cryogenic Target Handling System	6
Modeling the Temperature and Ice-Thickness Profiles Within OMEGA Cryogenic Targets	12
Target Detection and Shroud Pull Sequencing for Cryogenic-Target Operations on the OMEGA System	21
The Effect of Optical Prepulse on Direct-Drive Inertial Confinement Fusion Target Performance	30
Design and Synthesis of Near-Infrared Absorbing Dyes for the Liquid Crystal Point-Diffraction Interferometer (LCPDI)	37
Publications and Conference Presentations	

In Brief

This volume of the LLE Review, covering the period October–December 1999, includes a report on the stability of direct-drive NIF capsules. V. N. Goncharov, R. Betti, J. A. Delettrez, P. W. McKenty, S. Skupsky, and R. P. J. Town examine the conditions under which direct-drive NIF capsules ignite. Their numerical study uses two-dimensional hydrodynamic simulations in conjunction with a model that includes the various mechanisms that can influence target performance. Inner-surface roughness of the DT ice of the direct-drive cryogenic capsules and laser nonuniformities have been identified as the principal seeds of the instabilities that can potentially quench ignition. The authors conclude that a target gain greater than 10 can be achieved for a realistic inner-surface ice roughness when beam smoothing with 2-D SSD and a bandwidth greater than 0.5 THz is used.

Additional research highlights reported in this issue are

- R. Q. Gram, J. Hobler, L. D. Lund, and D. R. Harding report on the initial performance of the high-pressure deuterium- and tritium-filling portion of the Cryogenic Target Handling System. Thick-walled plastic targets have been successfully pressurized with deuterium to the required levels by the high-pressure filling system. Adequate control of the various factors influencing the filling process has been demonstrated, indicating that even thin-walled plastic targets (such as those required by the cryogenic target designs for OMEGA) can be successfully filled to the required high pressure.
- E. L. Alfonso, I. Anteby, and D. R. Harding present a numerical study of the principal sources of target nonuniformities for a cryogenic target when placed in the layering sphere. Deviations from idealized symmetry in the capsule-wall thickness, the displacement of the capsule relative to the center of the layering sphere, and the existence of temperature gradients on the layering sphere's inner surface can result in temperature gradients across the cryogenic target. This in turn affects the uniformity of the cryogenic fuel layer. Calculations of the temperature profile in these targets will be used to guide target fabrication and layering.
- T. H. Hinterman, C. Chiesa, B. Ferkovich, S. Johns, H. J. Kramer, D. J. Lonobile, and D. Lynch describe the target detection and the shroud pull-sequencing aspects of cryogenic target operations on OMEGA. The newly designed Cryogenic Target Detection System is based on existing elements of OMEGA controls and provides the necessary sequencing, safety features, and flexibility to allow for the evolution of cryogenic target operations.
- By implementing a contrast monitoring system on OMEGA, T. R. Boehly, Y. Fisher, D. D. Meyerhofer, W. Seka, J. M. Soures, and D. K. Bradley investigate laser prepulse levels on OMEGA and establish a contrast criterion for direct-drive implosions. Control of laser prepulses can be critical since high-intensity prepulses can potentially compromise the aluminum layer and cause unwanted laser damage to direct-drive targets. The authors find that while OMEGA intermittently produces measurable prepulses, the prepulse level is not expected to significantly degrade target performance.

- K. L. Marshall, M. J. Guardalben, and S. Corsello report on the successful design of dyes for a liquid crystal-based interferometer that will be used on OMEGA for a more-accurate wavefront characterization. Using state-of-the-art computational chemistry tools they have also demonstrated the effectiveness of modeling in guiding experimental searches for new dye compounds. Their work also has potential for other liquid crystal devices used in optical communications and sensor protection.

P. B. Radha

Editor

Stability Analysis of Directly Driven NIF Capsules

Introduction

In inertial confinement fusion (ICF), a spherical shell filled with a DT-gas mixture is compressed to high densities and temperatures to achieve ignition conditions.¹ Degradation from spherical symmetry during the implosion, however, limits the achievable compression ratios and could quench the ignition of the target. The main source of such asymmetry is hydrodynamic instabilities [such as Rayleigh–Taylor (RT)² and Bell–Plesset (BP)³ instabilities] seeded by both irradiation non-uniformities and target-fabrication imperfections. We have developed an analytical model to study stability of the direct-drive cryogenic NIF targets. The drive pulse for such targets consists of two distinct temporal regions (stages): the low-intensity (a few 10^{13} W/cm²) “foot” and the main drive (up to more than 10^{15} W/cm²). During the first stage, the laser energy is absorbed by the outermost layer of the target, heating up the shell material and launching a heat wave toward the pellet center. Material behind the heat front expands outwardly, creating an ablation pressure that induces the first shock wave propagating through the shell. Since the laser intensity in the first stage is constant in time and the equilibrium pressure behind the shock is uniform, the ablation front travels at constant velocity. In the absence of acceleration, the perturbations at the ablation front could grow due to the velocity and acceleration perturbations imposed by the laser-intensity modulations (“laser imprint”) and surface roughness [Richtmyer–Meshkov (RM)⁴ instability]. When the first shock breakout occurs at the rear surface of the DT ice, the pulse ramps up to the drive region (second or acceleration stage), launching the second shock. At this time, the ablation front starts to accelerate, creating conditions for the RT instability that magnify the perturbations seeded during the first stage. If the perturbation amplitude becomes too large during the shell acceleration, the shell breaks up and fails to reach ignition conditions. The shell integrity can be quantified by the “integrity factor” defined as $Y = A_{\text{mix}}/\Delta R$, where $A_{\text{mix}} \approx \sqrt{2}\sigma$ is the mix amplitude (bubble amplitude), ΔR is the shell thickness, and σ is the rms sum of the modes. The shell remains intact during the implosion if the integrity factor is less than unity for all time. At the end of the laser pulse, the shell starts to coast inward with

a constant velocity until the pressure of the DT-gas mixture becomes high enough to slow down the shell compression (beginning of the deceleration phase). During the deceleration phase the inner DT-ice surface is RT unstable. The growth due to this instability limits the compression ratios and increases the thermal conduction losses, reducing the total energy gain. Results from 2-D *ORCHID*⁵ simulations show that the gain reduction depends on the mode spectrum at the end of the acceleration stage. In this article we estimate the integrity factor during the acceleration phase and calculate the spectral distribution of the modes by using the results of the developed model and 2-D *ORCHID* simulations.

Seeding of RT Instability: Laser Imprint, Ablative RM Instability, and “Feedout”

As mentioned earlier, at the beginning of implosion, the ablation pressure launches a shock wave toward the target center. The surface roughness (due to the target fabrication imperfections) and also modulations in the laser intensity deform the shock front and generate perturbed velocity and acceleration fields inside the compressed region. During the shock transit time, the ablation front travels with a constant velocity, and the front perturbations could grow due to imposed velocity and acceleration perturbations.

1. Laser Imprint

Nonuniformities in the laser intensity cause different parts of the beam to ablate shell material at different rates, generating an ablation-pressure modulation along the ablation front. Since the shock speed scales as a square root of the shock strength, stronger shocks launched at the peak of ablation pressure propagate faster than shocks launched at the pressure valleys. The difference in the shock speeds distorts the shock front and creates a perturbed velocity field inside the compressed region. A velocity perturbation at the ablation front, in turn, leads to a linear-in-time front distortion growth $\eta \sim t$. Then, a rippled shock generates a lateral mass flow that leads to a pressure deficiency in the convex part (which protrudes the most into the uncompressed shell) and a pressure excess in the concave part of the shock front. This creates a pressure gradient that accel-

erates fluid elements, leading to an additional growth $\eta \sim t^2$. In ICF, however, several physical processes significantly reduce the imprint growth. First, as the heat front propagates into the cold portion of the target, material heats up and expands outwardly, creating a hot plasma corona. Thus, a finite zone (conduction zone) of hot plasma exists between the energy absorption region and the ablation front. Any pressure perturbations inside such a zone are reduced by the thermal conduction. The simplest theory⁶ (“cloudy day effect”) predicts that the pressure perturbations decay exponentially away from the critical surface $\tilde{p} \sim e^{-kx}$; thus, nonuniformities in the ablation pressure are reduced by a factor of e^{-kD_c} , where D_c is a distance between the absorption region and the ablation front, and k is the wave number corresponding to a specific mode of non-uniformity. An additional reduction in the imprint growth is due to the mass ablation. The main stabilizing mechanism produced by ablation is the dynamic overpressure or “rocket effect.”^{7,8} As a result, the imprint amplitude η_{imp} , which is defined as the amplitude of the ablation-front ripple calculated at the shock breakout time, takes the following form:⁹

$$\frac{\eta_{\text{imp}}}{\Delta R(\delta I_l/I_0)} \approx 0.4 \frac{A}{l} \hat{\eta} \left(e^{-\Delta_c} - e^{-2\Delta_a} \cos \Delta_{\text{bl}} \right) + \frac{e^{-2\Delta_a}}{\Delta_{\text{bl}}} \left(0.9 + 0.8 \frac{V_c}{c_s} \hat{\eta} \right) \sin \Delta_{\text{bl}} + \eta_v^{\text{imp}}, \quad (1)$$

where δI_l is the intensity modulation, I_0 is the average intensity,

$$\hat{\eta} = c_s^2 / (V_a V_{\text{bl}} + V_c^2),$$

$$\Delta_a = 2(l/A) V_a / c_s,$$

$$\Delta_{\text{bl}} = 2(l/A) \sqrt{V_a V_{\text{bl}}} / c_s,$$

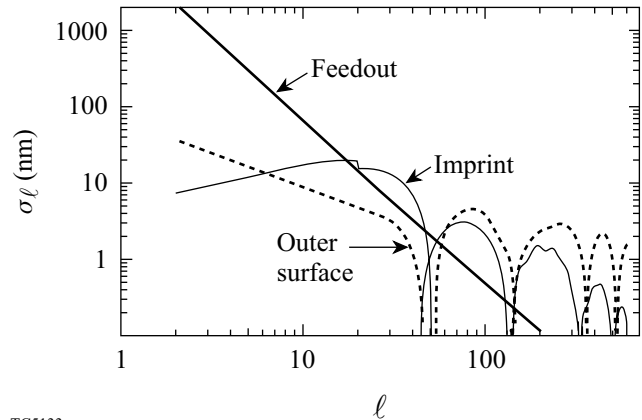
A is the shell’s in-flight aspect ratio, V_a and V_{bl} are the ablation and blow-off velocities, respectively, V_c is the velocity of the critical surface with respect to the ablation front, and c_s is the sound speed of the compressed material. The term η_v^{imp} is due to the vorticity convection from the shock front.

Using the analytical model of the RT instability (described later in the **Acceleration Phase** section), it is found that laser imprint alone can break up the shell during target acceleration and this can quench ignition; thus, an additional reduction in

imprint amplitude is critical for a successful implosion. A significant improvement in the beam uniformity has been made in recent years by introducing smoothing by spectral dispersion (SSD)¹⁰ and induced spatial incoherence (ISI)¹¹ smoothing techniques. To account for the intensity variation in a realistic laser pulse, SSD is modeled using the 2-D hydrocode *ORCHID*, where the intensity nonuniformities have been reduced by the factor $\sqrt{t_c/(t_c + 4t)}$. This gives on average a reduction in rms of laser nonuniformity $\sigma = \sqrt{t_c/t_{\text{avg}}} \sigma_0$, where the coherence time is taken to be

$$t_c = [\Delta v \sin(k\delta/2)]^{-1},$$

Δv is the bandwidth, t_{avg} is the averaging time, and δ is the speckle size. The result of 2-D *ORCHID* simulations (mode spectrum due to imprint (thin solid line) at the beginning of the acceleration phase) of the “all-DT” NIF target design¹² is plotted in Fig. 81.1. This result will be used later as an initial condition for the RT model.



TC5133

Figure 81.1
Mode spectrum at the beginning of the acceleration phase.

2. Outer-Surface Roughness

When the outer surface of the target is distorted, the ablation pressure launches a ripple shock at the beginning of implosion. The ripple shock, as discussed in the previous subsection, generates a lateral flow that leads to a perturbed pressure gradient and the perturbation growth. The theory describing the perturbation evolution at the corrugated ablation front driven by uniform laser irradiation has been described in Ref. 7. The theory shows that in the presence of ablation, the front perturbations oscillate in time with a damped amplitude. The main stabilizing mechanisms are the rocket effect and the vorticity

convection from the ablation front. Calculations⁷ show that the perturbation amplitude at the beginning of the acceleration phase normalized to the initial amplitude $\eta_0(l)$ can be written as

$$\frac{\eta^s}{\eta_0(l)} \approx \eta_v \left(\frac{2\Delta R}{c_s} \right) + \left\{ \frac{0.8c_s}{\sqrt{V_a V_{bl}}} \sin \Delta_{bl} - [0.1 + \eta_v(0)] \cos \Delta_{bl} \right\} e^{-2\Delta a}, \quad (2)$$

where the vorticity term $\eta_v(t)$ is defined in Ref. 7. Using Eq. (2) and taking the initial spectrum $\eta_0(l)$ from Ref. 12 (assuming surface finish of 840 Å), the mode spectrum due to a finite outer-surface finish is plotted in Fig. 81.1 (dashed line).

3. Inner-Surface Roughness (Feedout)

An additional seed of the RT instability is due to the rear-surface roughness that feeds out by the rarefaction wave generated at the first shock breakout time.¹³ The shock front first reaches the perturbation valleys, generating a rarefaction wave that starts to propagate toward the ablation front with the sound speed. By the time the shock reaches the perturbation peaks, the rarefaction wave originated at the perturbation valley has moved a finite distance, distorting the rarefaction wavefront. The peaks and valleys of the rarefaction wave travel at the sound speed, keeping the ripple amplitude constant. As the rarefaction wave breaks out of the shell, the ablation front starts to accelerate. Since the rarefaction front is distorted, however, there is a delay in accelerating the ablation front at the peaks and valleys. Because of such a delay, a finite velocity perturbation imprints at the ablation front, generating a seed for the RT instability. An additional seed (perturbation acceleration field) is created by the mass difference under the perturbation valleys and peaks. According to calculations,¹³ the feedout amplitude, $\eta^{f.o.}$, takes the following form:

$$\frac{\eta^{f.o.}}{\Delta_l} = \frac{0.06A}{l} + 0.15 \sqrt{\frac{A}{l}}, \quad (3)$$

where Δ_l is the initial rear-surface spectrum. Figure 81.1 shows mode spectrum due to feedout at the beginning of acceleration phase (thick solid line), assuming $\Delta_l \sim l^{-2}$ (Ref. 14) and initial total rms of the rear-surface modes $\sigma_r = 3 \mu\text{m}$.

Acceleration Phase

During the shell acceleration, the pressure and density gradients at the ablation front have opposite directions, creating a condition for the RT instability. In addition, because of the spherical convergence, the inner surface is subject to the BP instability. The RT and BP instabilities amplify the perturbations seeded during the first stage of the implosion.

Since the implosion of spherical shells is intrinsically unsteady (shell density, ablation velocity, and acceleration change in time), steady-equilibrium models cannot be used to study perturbation evolution, and a model for unsteady equilibria must be developed. The full system of conservation equations, however, is too difficult to be solved analytically. One of the simplifications that make the problem analytically tractable is an idealization of the ablation front as a surface of discontinuity [“sharp-boundary model” (SBM)]. The accuracy of such a model is compromised only when the mode wavelength is shorter than the ablation-front thickness L_0 . For ablators with small Froude numbers, such as CH or Be [the Froude number is defined as $V_a^2 / (gL_0)$, where g is acceleration], $L_0 \approx 0.1$ to $1 \mu\text{m}$; hence, for modes with the largest growth factors (the most damaging modes: $80 < l < 300$), the condition $kL_0 < 1$ is satisfied during the acceleration stage (assuming the minimum shell radius is $500 \mu\text{m}$). The density-gradient stabilization, nevertheless, can be included in simplified fashion by reducing the ablation-front acceleration by a factor $(1 + lL_m/R)^{-1}$, where L_m is the minimum density-gradient scale length and R is the shell radius. For ablation fronts with large Froude numbers, such as cryogenic DT, the unstable spectrum consists of only long-wavelength modes; thus, the SBM is valid in this case for all unstable modes. The model yields coupled differential equations describing the evolution of the outer and inner surfaces. The coefficients of these equations are functions of the ablation and the inner DT-ice interface trajectories and the ablation velocity that can be calculated using 1-D numerical simulations. To account for the nonlinear saturation, 3-D Haan’s model¹⁵ is applied after the mode amplitude reaches the saturation level $S(l) = 2R/l^2$. The accuracy of the developed RT model has been tested against 2-D *ORCHID* and *FCI2*¹⁶ simulations. For the most damaging modes, the prediction of the model is in good agreement with the numerical results.

The model shows that the shell remains intact during the implosion (the integrity factor is less than unity) if the laser nonuniformities are smoothed by 2-D SSD with the laser bandwidth larger than 0.3 THz, the outer-surface finish not exceeding $0.1 \mu\text{m}$, and the inner-surface finish $\sigma_r < 8 \mu\text{m}$ (assuming $\Delta_l \sim l^{-2}$). As shown in the next section, however,

the restriction on the minimum target gain imposes more stringent requirements for the irradiation uniformity and the surface finish.

Target Gain

As the shell accelerates inward, ablation-front perturbations grow due to the RT instability and feed through the shell approximately as $\eta_i(l) \approx \eta_a(l)(r_i/r_a)^l$, where $\eta_i(l)$ and $\eta_a(l)$ are the l -components of the inner- and ablation-surface amplitudes, respectively, and r_i and r_a are the inner- and ablation-surface radii. During the coasting and deceleration stages, the “feedthrough” grows, reducing the target compression ratio and limiting the ignition gain. To study the gain-reduction dependence on the mode spectrum, a series of 2-D *ORCHID* multimode simulations have been performed for an $\alpha = 3$ cryogenic NIF target design¹² with the distorted inner DT-ice interface. The initial power spectrum is taken in the form $\sigma_l = \sigma_0/l^\beta$ (Ref. 14), where σ_0 and β are the normalization constants. Since the spectrum of the inner-surface perturbations at the end of acceleration phase is heavily weighted toward the low mode numbers, the simulations have been performed for modes $2 < l < 50$ with the range of β and total rms 0 to 1.5 and 0.5 to 12 μm , respectively. The target gain is found to be a function of

$$\bar{\sigma} = \sqrt{0.06\sigma_{<10}^2 + \sigma_{\geq 10}^2},$$

where $\sigma_{<10}^2$ and $\sigma_{\geq 10}^2$ are rms nonuniformity of the modes below and higher than $l=10$. $\bar{\sigma}$ is calculated by using the inner-surface spectrum at the end of the acceleration phase. The simulation results are summarized in Fig. 81.2, where target gain is plotted versus $\bar{\sigma}$. Next, to take into account the laser imprint and surface roughness, the model described in the **Acceleration Phase** section is applied to the $\alpha = 3$ cryogenic NIF target design using the initial conditions derived in the **Seeding of RT Instability** section. Then, using both the derived mode spectrum and the result of Fig. 81.2, the target gain is plotted in Fig. 81.3 as a function of rear-DT-ice-surface finish and the laser bandwidth, assuming the initial outer-surface rms of 840 Å. Figure 81.3 shows that the yield reduction is less than 50% with respect to 1-D calculations if the inner-surface finish does not exceed 1.5 μm and the laser nonuniformities are smoothed by 1-THz, 2-D SSD.

Summary

An analytical model has been presented to study perturbation evolution at the ablation and inner surfaces of the imploding shell. The model describes the ablative Rayleigh–Taylor

and Bell–Plesset instabilities. The initial conditions for the model are determined by using existing theories of laser imprint, ablative Richtmyer–Meshkov instability, and feedout, and by performing a series of 2-D *ORCHID* simulations. The model and simulations showed that the direct-drive cryogenic $\alpha = 3$ NIF capsules remain intact during the implosion and the target gain is expected to be larger than 10 if laser nonuniformities are smoothed by 2-D SSD with the bandwidth $\Delta\nu > 0.5$ THz and inner-surface rms $< 1.5 \mu\text{m}$.

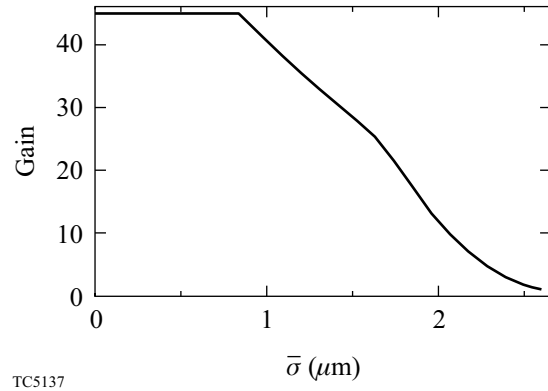


Figure 81.2
Plot of target gain G versus $\bar{\sigma}$.

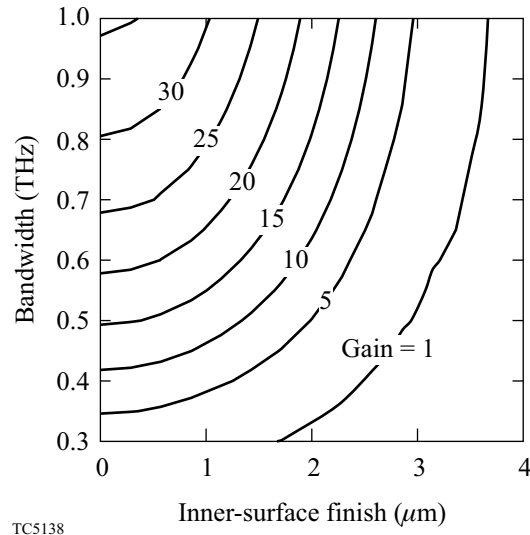


Figure 81.3
Plot of target gain versus initial rear-surface finish and laser bandwidth.

ACKNOWLEDGMENT

This work was supported by the U.S. Department of Energy Office of Inertial Confinement Fusion under Cooperative Agreement No. DE-FC03-92SF19460, the University of Rochester, and the New York State Energy Research and Development Authority. The support of DOE does not constitute an endorsement by DOE of the views expressed in this article.

REFERENCES

1. J. D. Lindl, *Inertial Confinement Fusion: The Quest for Ignition and Energy Gain Using Indirect Drive* (Springer-Verlag, New York, 1998).
2. Lord Rayleigh, in *Scientific Papers* (Cambridge University Press, Cambridge, 1900), Vol. II, p. 200.
3. M. S. Plesset, *J. Appl. Phys.* **25**, 96 (1954); G. I. Bell, Los Alamos National Laboratory, Report No. LA-1321 (1951).
4. R. D. Richtmyer, *Commun. Pure. Appl. Math.* **XIII**, 297 (1960).
5. R. L. McCrory and C. P. Verdon, in *Computer Applications in Plasma Science and Engineering*, edited by A. T. Drobot (Springer-Verlag, New York, 1991), pp. 291–325.
6. S. E. Bodner, *J. Fusion Energy* **1**, 221 (1981).
7. V. N. Goncharov *et al.*, *Phys. Rev. Lett.* **82**, 2091 (1999).
8. A. R. Piriz, J. Sanz, and L. F. Ibanez, *Phys. Plasmas* **4**, 1117 (1997).
9. V. N. Goncharov, S. Skupsky, P. W. McKenty, R. P. J. Town, T. R. Boehly, D. D. Meyerhofer, and O. V. Gotchev, “A Model of Laser Imprinting,” accepted for publication in *Physics of Plasmas*.
10. S. Skupsky, R. W. Short, T. Kessler, R. S. Craxton, S. Letzring, and J. M. Soures, *J. Appl. Phys.* **66**, 3456 (1989).
11. R. H. Lehmburg, A. J. Schmitt, and S. E. Bodner, *J. Appl. Phys.* **62**, 2680 (1987).
12. S. V. Weber, S. G. Glendinning, D. H. Kalantar, M. H. Key, B. A. Remington, J. E. Rothenberg, E. Wolfrum, C. P. Verdon, and J. P. Knauer, *Phys. Plasmas* **4**, 1978 (1997); Laboratory for Laser Energetics LLE Review **79**, 121, NTIS document No. DOE/SF/19460-317 (1999). Copies may be obtained from the National Technical Information Service, Springfield, VA 22161.
13. R. Betti, V. Lobatchev, and R. L. McCrory, *Phys. Rev. Lett.* **81**, 5560 (1998).
14. Laboratory for Laser Energetics LLE Review **79**, 131, NTIS document No. DOE/SF/19460-317 (1999). Copies may be obtained from the National Technical Information Service, Springfield, VA 22161.
15. S. W. Haan, *Phys. Rev. A* **39**, 5812 (1989).
16. E. Buresi *et al.*, *Laser Part. Beams* **4**, 531 (1986).

Initial Performance of the High-Pressure DT-Filling Portion of the Cryogenic Target Handling System

Cryogenic targets for the OMEGA laser are polymer shells of ~1-mm diameter and 1- to 5- μm wall thickness that require internal D_2 or DT solid layers of ~100- μm thickness. Targets containing D_2 may also be doped with gaseous He^3 to aid in diagnosing the implosion using the charged-particle spectrometer. To achieve the required inner ice layer, shells are first permeated to a pressure of ~1000 atm at room temperature and then cooled to ~25°K. A slow, controlled pressure ramp to avoid buckling of the target and a slow, controlled temperature ramp to 25°K are required to successfully fill targets. The thinnest-walled shells, which are of the greatest interest, have buckling pressures ≤ 0.1 atm, which imposes a requirement of considerable precision in controlling the pressure differential across the shell wall during the pressurization and cooldown. LLE has constructed a system that successfully fills thick-walled targets and demonstrates the capabilities necessary to fill thin-walled targets.

System Description

The pressurization portion of the Cryogenic Target Handling System achieves compression in two stages (as seen in Fig. 81.4): (1) by slowly heating the cryogenically concentrated D_2 or DT and (2) by using a diaphragm compressor. The process begins with valves V1, V3, and V6 open, all other valves closed, and the targets evacuated. The condensation tube (volume 12.0 cm^3) is cooled to ~10°K, and the contents (~0.3 mole) of the D_2 or DT vessel are condensed into it; then valves V4 and V5 are opened, providing a path for gas to reach the permeation cell, which contains four targets at room temperature. Next, valve V1 is closed and V2 is opened, allowing a small quantity of He^3 to flow to the targets. A pressure of ~0.03 atm of He^3 added at this point will produce a 5% concentration of He^3 in the gaseous D_2 in the center of a target at the triple point, 18.7°K. To start the first stage of compression, valve V3 is closed, and the condensation tube is slowly heated

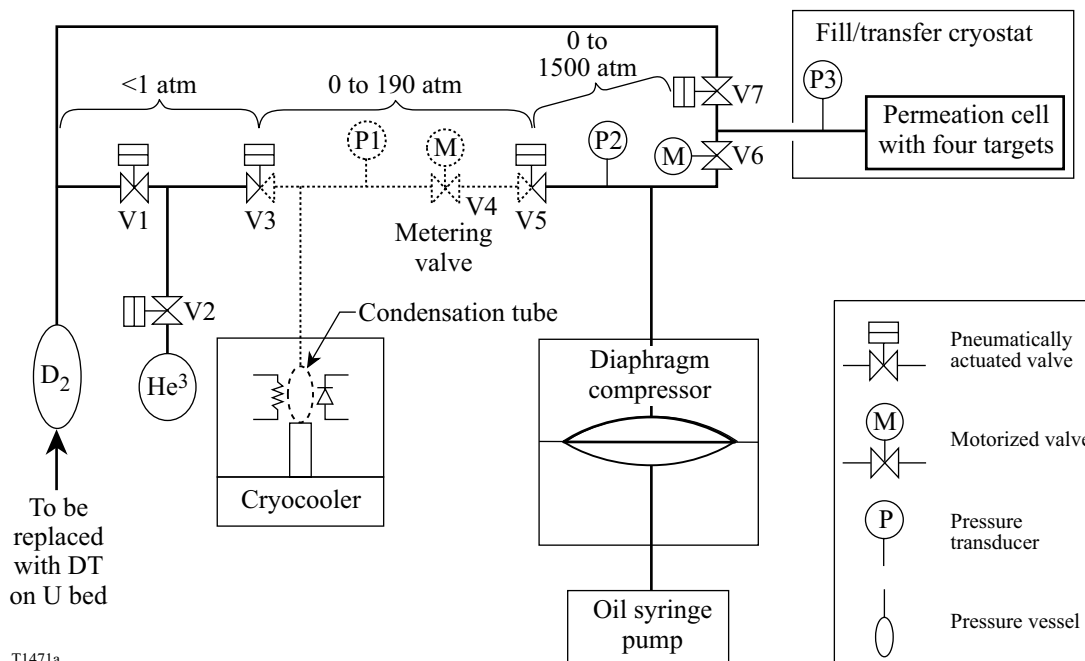


Figure 81.4

Abbreviated diagram of the pressurization portion of the system. The parts omitted include burst discs, limit switches, solenoid valves, and controllers.

until the pressure in the targets reaches ~150 atm (190 atm maximum). The second stage of compression is achieved by closing valve V5 and slowly driving the diaphragm compressor to the final pressure, typically 1000 atm (1500 atm maximum). This compressor has a flexible metal diaphragm with up to 30.9 cm³ of gas on one side and hydraulic oil on the other. The oil is compressed by a syringe pump, which uses a piston (area = 1.60 cm², stroke = 24.3 cm) linked by a gear train (126 turns/cm) to a stepper motor (1000 steps per turn). Although pressure transducers are located in both stages and on the permeation cell, system control depends primarily on the transducer P2—a highly accurate (± 0.14 atm) Bourdon tube—in the second stage.

After the targets have reached the maximum pressure, they are slowly cooled to <25°K before the D₂ or DT external to the targets is pumped out of the permeation cell. For thick-walled targets, the cooling is done with valve V6 closed. Cooling must be done slowly enough that the cooled portion of the pressurization system remains isothermal, avoiding temperature gradients that could produce a pressure differential across the target wall, causing the target to burst or buckle. Thin-walled targets, because they are weaker, require an alternative cooling strategy:* Valve V6 is left open, and the compression equipment is run in reverse to lower the pressure as the targets are cooled, keeping the measured external pressure very close to the calculated internal pressure. Once the targets are cooled to <25°K, the vapor pressure of D₂ or DT is <2 atm, and the gas external to the targets can be pumped out of the permeation cell without risk of bursting the targets. This pumping is done with valve V7 open; it continues (possibly for several hours) until the residual quantity of gas in the permeation cell will be manageable when the cell is unsealed and this residual gas is released into the cryostat.

*If valve V6 could be located inside the cryostat and cooled along with the permeation cell so that all portions of the pressurized volume remained isothermal, the pressures internal and external to the target would be nearly equal throughout the cooling process. (A small excess pressure would still arise internal to the target because the thermal contraction of a polymer shell exceeds that of the metal permeation cell.) Such a cryogenically compatible valve is not available. If valve V6 is closed prior to the cooldown, the small volume in the room-temperature plumbing (~0.3 cm³, compared to 5.0 cm³ of cooled volume) generates a pressure external to the target. This is because gas in the room-temperature portion is less dense than the cooled gas. The external pressure generated by this density difference is sufficient to cause thin-walled targets (wall thickness <5 μ m) to buckle. Success in cooling thin-walled targets with valve V6 open and the compression equipment running in reverse requires accurate determination of the target temperature and calculation of the corresponding internal pressure. Since thin-walled targets are much stronger against bursting than against buckling, the best strategy is to keep the external pressure slightly below the calculated internal pressure.

The system is controlled by a programmable logic controller (PLC), which is linked to a workstation with a graphical user interface (GUI). All valves and motors in the system are controlled by the PLC, which also monitors all pressures, temperatures, and the status of limit switches. The pressurization ramp is managed by control loops that include the high-accuracy pressure transducer, the condensation tube thermometer and heater, and the motor driving the oil syringe pump. These loops are executed and maintained by “C” programs residing in the PLC. The GUI software allows the user to monitor, log, and view data from the target-fill process in real-time. It also allows modification of the fill rate and parameters of the control loops. There are several hard-wired safeguards, such as limit switches that prevent excess piston travel in the syringe pump.

All system parts that will contain ≥ 1 atm of DT have been provided with secondary vacuum containment, with a glovebox providing tertiary containment. This secondary containment is divided into four chambers. Helium gas at ~0.5 atm will be circulated through three of these chambers with a circulation pump, while the fourth chamber is kept evacuated to insulate the condensation tube. The divisions of the secondary containment system are shown in Fig. 81.5. A modified ion gauge will detect tritium leakage with a resolution of ~10 mCi/m³ at 1 atm and ~150 mCi/m³ at <1 Torr. If a low-level tritium leak is detected, the tritium-contaminated helium will be pumped to the tritium recovery system, evacuating the contaminated chamber. High-level leakage will be routed with the circulation pump to a local uranium bed, which will absorb the DT. Volumes in the secondary containment chambers are sufficient to contain the entire DT inventory of 0.34 mole (10⁴ Ci) below 1 atm at room temperature.

Target Filling

Four targets are filled simultaneously. Each target is supported by three submicron strands of spider silk¹ as shown in Fig. 81.6. The spider silk is stretched across a beryllium wire frame, which is formed into a shape that avoids the OMEGA laser beams, and coated with a uniform, conformal layer of 0.1 μ m of parylene, which fastens the silk to the shell. The Be frame is attached to a boron fiber, which is in turn attached to an Al base. This mounting method is highly robust at cryogenic temperatures. The four targets are placed in a contoured copper holder, as shown in Fig. 81.6. The copper holder acts to improve the temperature uniformity inside the permeation cell and also provides a space filler to minimize the volume. With this holder inside the sealed permeation cell, the cooled volume is 5.0 cm³. Reducing the gap between the copper holder and the

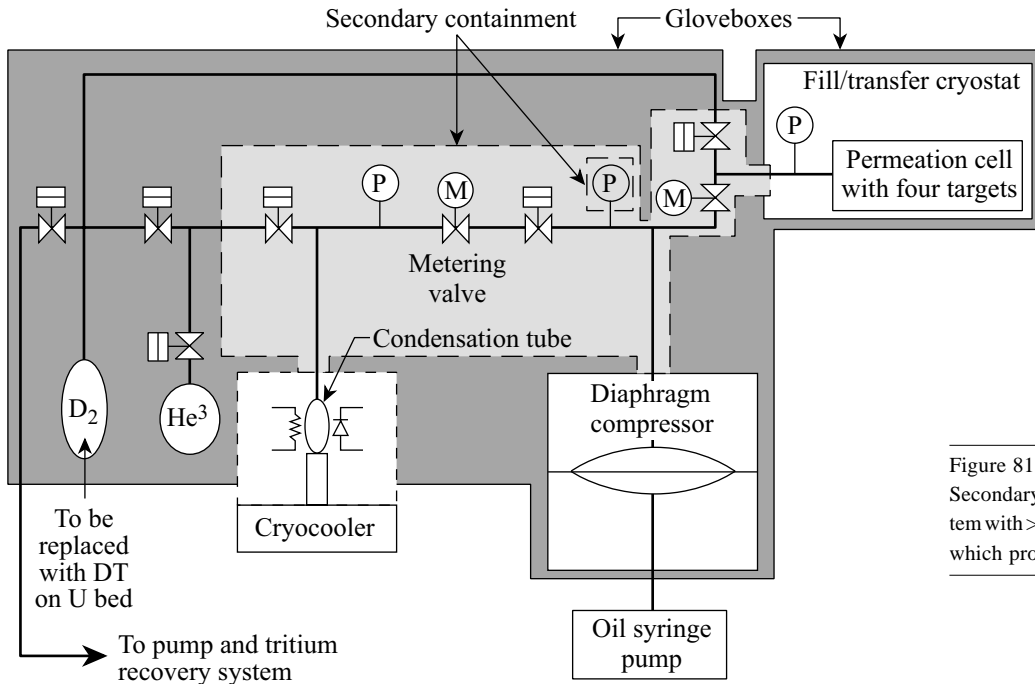


Figure 81.5
Secondary containment for all parts of the system with >1 atm of DT, and the outer gloveboxes, which provide tertiary containment.

target support elements could reduce this volume, which would reduce the percentage of the DT inventory required to fill a set of targets (currently 82%). The tighter tolerances, however, would increase the difficulty of removing targets for transport, and a higher target attrition rate might be expected.

Filling thin-walled targets will take from 8 to 60 h, depending on the specifications of the targets. To fill them as quickly as possible, the pressure is increased at a uniform rate such that the external pressure exceeds the internal pressure by an amount ΔP , which is less than the buckling pressure:²

$$\Delta P < \frac{8E}{[3(1-\mu^2)]^{1/2}} \left(\frac{w}{D}\right)^2, \quad (1)$$

where w = wall thickness, D = diameter, E = Young's modulus, and μ = Poisson's ratio. For plasma polymer shells,³ this formula was confirmed experimentally at LLE by pressurizing shells of various wall thicknesses in the 1- to 10- μm range and measuring their buckling pressures. To compare the data to Eq. (1), the value of E used was 2.1 GPa, obtained by measuring the expansion of several plasma polymer shells due to internal pressure. The value of μ used was 0.35 (the value for polystyrene, a glassy polymer with somewhat similar properties to plasma polymer). The permeation time constant for an ideal gas is given by

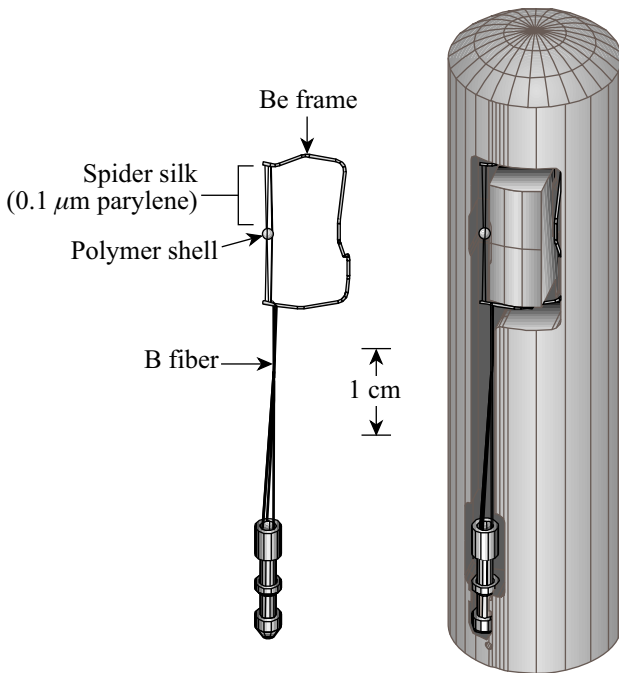


Figure 81.6
Cryogenic target supported with spider silk, and a holder for four targets (only one of the four cavities is shown); also see p. 21, Fig. 81.21, this issue.

$$\tau = \frac{wD}{6pRT}, \quad (2)$$

where p = permeability, R = gas constant, and T = absolute temperature. Since D_2 at high pressure is less dense than an ideal gas (62% of the ideal gas density for 1000 atm at 294°K), a larger time constant is expected at high pressure, suggesting that a cautious rate of pressure rise should be used. For a uniform rate of pressure rise, the pressure differential across the shell wall is proportional to the permeation time constant after a time $t \gg \tau$:

$$\Delta P = \tau \frac{dP}{dt}. \quad (3)$$

Combining Eqs. (1), (2), and (3), the maximum pressurization rate is proportional to wall thickness/(diameter)³:

$$\frac{dP}{dt} = \frac{\Delta P}{\tau} < \frac{48EpRT}{[3(1-\mu^2)]^{1/2}} \frac{w}{D^3}. \quad (4)$$

For a plasma polymer shell with $w = 1 \mu\text{m}$ and $D = 1 \text{ mm}$, the buckling pressure is 0.1 atm, $\tau = 10 \text{ s}$, and filling to 1000 atm at room temperature requires more than 30 h. The filling time may be reduced by filling at an elevated temperature.

System Performance

Several thick-walled targets have survived filling with D_2 to a pressure of 1000 atm. In the first test, two mounted targets with 1-mm diameter and wall thicknesses of 10 μm and 20 μm were filled to 1000 atm over an 8-h period, left under pressure for 3 days, and then depressurized over an 8-h period. After removing the targets from the permeation cell, microscopic examination indicated no damage to the targets or the mounts. In the second test a similar pair of plasma polymer targets along with a polyimide target were pressurized and then slowly cooled to 20°K. The permeation cell was then unsealed, and the targets were viewed at 20°K through a fiber-optic borescope. The targets were seen to be intact. One of the targets was picked up with the robot arm and deposited on the tip of the moving cryostat, where the target was warmed. A sudden spike in pressure of the expected magnitude indicated that it had exploded, as expected, and that it had retained all the D_2 from the filling process.

The performance of the two compression stages is studied by comparing experimental data to the D_2 equation of state.

This comparison requires knowledge of the volume of each part of the system. The volume of each part is determined by connecting to a known volume and observing the pressure change when gas flows to or from the volume being measured. A 24-term equation developed by NIST⁴ gives pressure as a function of density for D_2 above the critical point (38.3°K), using terms up to the seventh power of density and sixth power of temperature. At temperatures below the critical point, saturated vapor pressures⁵ are used. It is difficult to predict pressure and density accurately in the region of the critical point (and down to the point where the liquid phase begins), and it is planned to rely on data taken with the pressurization apparatus itself.

Performance of the condensation tube for pressure generation is shown in Fig. 81.7. The data are taken by condensing 0.123 moles of D_2 (determined by measuring the change in pressure in the D_2 supply reservoir and converting to moles with the equation of state), and then raising the temperature of the condensation tube slowly enough to assure isothermal conditions in the tube (the tube, made of stainless steel, is in good contact on all sides with copper of high thermal conductivity). The 0.123 moles are distributed between the 12.0-cm³ cooled volume and the 5.32-cm³ volume (tubing, burst disc, and valves) at room temperature. A good match is obtained between measured data points and the expected pressure, calculated with the NIST equation of state.

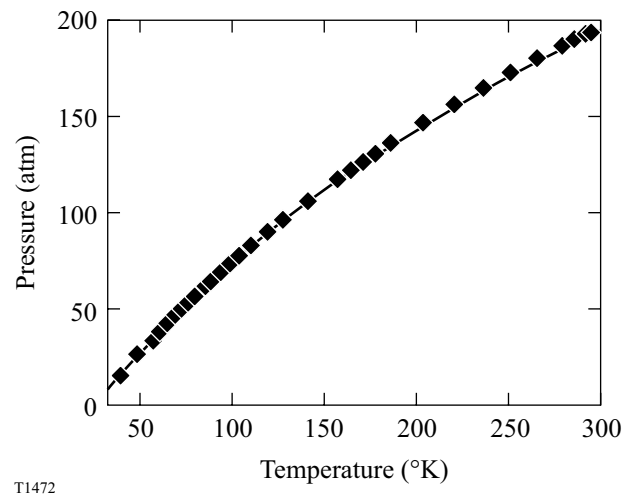


Figure 81.7

The pressure in the condensation tube (measured points) is accurately characterized by the D_2 equation of state above 38°K (used to compute the solid line).

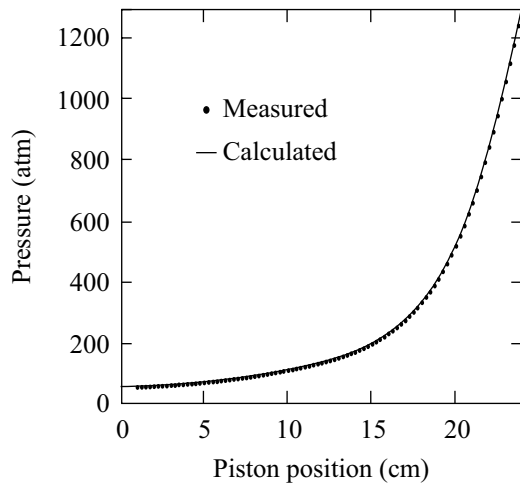
Analyzing the performance of the diaphragm compressor requires knowledge of the oil compressibility. The manufacturer of the compressor⁶ supplies compressibility data for the oil,⁷ which are fit by the equation

$$C(P) = b_1 (P/1 \text{ atm}) - b_2 (P/1 \text{ atm})^2, \quad (5)$$

where $b_1 = 5.30 \times 10^{-5}$, $b_2 = 6.4 \times 10^{-9}$, and $C(P)$ is defined as the fractional reduction in oil volume from its uncompressed value at pressure P . The expected pressure is obtained by first computing the D_2 molar density,

$$\rho = \frac{M}{V_0 - [A \cdot z - V_{\text{oil}} \cdot C(P)]}, \quad (6)$$

where M is the number of moles, V_0 is the initial volume, A is the area of the piston, z is the distance of piston travel, and V_{oil} is the uncompressed volume of oil. The pressure values entered in this equation are obtained by expressing the experimentally measured pressure data as a continuous function of z . The NIST equation of state is then used to convert density to pressure. Figure 81.8 shows good agreement between measured and calculated pressure. The fitting parameter adjusted to obtain agreement between measured and calculated pressures is $V_{\text{oil}} = 113.5 \text{ cm}^3$, which cannot easily be measured. In addition, $b_2 = 4.2 \times 10^{-9}$ provided a much better fit at high pressures than the manufacturer's data. For this analysis, it has been assumed



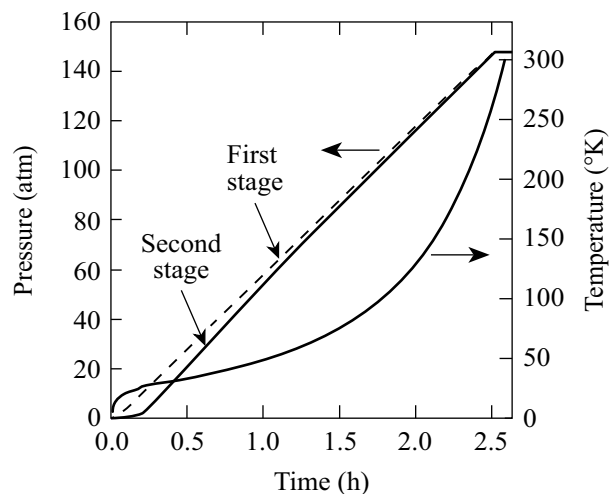
T1519

Figure 81.8

Pressure versus piston position is accurately characterized by the D_2 equation of state and oil compressibility data. Error bars for the measured points are too small to see. The maximum difference between measured and computed pressures is 8 atm for the whole data set, 2 atm at pressures <500 atm, and 0.1 atm at pressures <160 atm.

that the oil pressure and gas pressure are the same, and that the extra component of oil pressure required to deform the diaphragm is negligible.

To pressurize targets, a temperature versus time profile is calculated for the condensation tube, using vapor pressure data, and the equation of state. This calculated profile is used to program a temperature controller, which uses a PID loop to control the temperature. An example of a successful temperature profile and the resulting uniform rate of pressure rise is shown in Fig. 81.9. The difference in pressure between the first and second stages is due to the metering valve, fully open in this case. The ramp that was obtained would be suitable for a shell with a 3- μm -thick wall and a 1-mm diameter, but the method should work equally well to generate a pressure ramp suitable for a shell with a 1- μm wall. Hidden in these data are small departures from a constant rate of pressure rise, which should be correctable by adjusting the temperature profile with measured data near the critical point. This procedure's success in generating a constant rate of pressure rise offers an opportunity to eliminate the metering valve. There is strong incentive to eliminate this valve because of stem-seal leakage. Leakage through this valve stem was detected by pressurizing the system with He and was not eliminated by replacing the O-ring. The stem is sealed by a single O-ring, which appears not to be sufficiently constrained. Even if constraints on the O-ring were improved, leakage would be expected when the valve stem is moved.

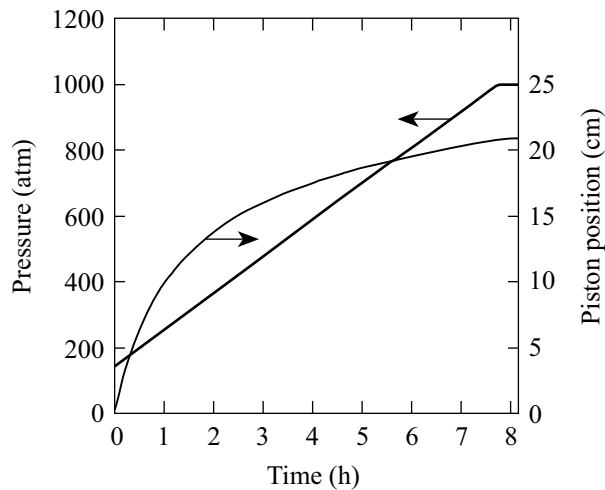


T1488

Figure 81.9

A uniform rate of pressure rise is produced by applying a calculated temperature profile to the condensation tube.

To generate the high-pressure portion of the pressure ramp, a valve is closed to isolate the diaphragm compressor from the condensation tube. The piston of the syringe pump is then given an initial velocity, and a simple algorithm is applied to the resulting rate of pressure rise to adjust the piston velocity to match the desired rate of pressure rise. The result is shown in Fig. 81.10, which shows a pressure ramp suitable for a shell with a 5- μm wall thickness. Upon magnification of the pressure versus time data in Fig. 81.10, the pressure is found to be increasing smoothly at all times, with small variations in slope due to the control algorithm. No obstacle is found to the use of a much slower rate of pressure rise, which would be suitable for filling shells with 1- μm wall thickness.



T1474

Figure 81.10

A constant rate of pressure rise is produced by controlling the piston position with a simple algorithm.

The pressurization system has proven robust, with all indications that it will be able to fill shells with the thinnest walls. Three additional observations contribute to this conclusion. The smallest motion increment of the motor driving the oil syringe pump corresponds to 0.002 atm at a pressure of 1000 atm, and less at lower pressures, much less than the 0.1-atm buckling pressure of shells with 1- μm wall thickness.

When the motor direction is reversed, as will be necessary when cooling thin-walled shells, there is one turn of backlash in the mechanical system, but no observable pressure drop that could threaten shell survival. Finally, it appears that the low rate of temperature rise required for the condensation tube ($\sim 0.1^\circ\text{K}/\text{min}$ at 40°K) is achievable by applying a slowly increasing power level ~ 12 W. To demonstrate the capacity to fill thin-walled shells, a series of increasingly slower pressure ramps will be used to fill successively thinner walled shells, followed by depressurization ramps and examination of the shells. The final and most difficult step will be to again fill such targets and reduce the external pressure while cooling the targets by running the pressurization apparatus in reverse.

ACKNOWLEDGMENT

The pressurization portion of the CTHS is based on a conceptual design by General Atomics. The use of spider silk to support targets was pioneered by S. G. Noyes of LLE, who also developed the present attachment method. This work was supported by the U.S. Department of Energy Office of Inertial Confinement Fusion under Cooperative Agreement No. DE-FC03-92SF19460, the University of Rochester, and the New York State Energy Research and Development Authority. The support of DOE does not constitute an endorsement by DOE of the views expressed in this article.

REFERENCES

1. B. A. Brinker, J. M. Cavese, J. R. Miller, S. G. Noyes, S. Sheble, and L. T. Whitaker, *J. Vac. Sci. Technol. A* **1**, 941 (1983).
2. W. C. Young, in *Roark's Formulas for Stress & Strain*, 6th ed. (McGraw-Hill, New York, 1989), p. 691.
3. S. A. Letts, D. W. Myers, and L. A. Witt, *J. Vac. Sci. Technol.* **19**, 739 (1981); S. A. Letts *et al.*, *Fusion Technol.* **28**, 1797 (1995); B. W. McQuillan *et al.*, *Fusion Technol.* **31**, 381 (1997).
4. R. Prydz, K. D. Timmerhaus, and R. B. Stewart, in *Advances in Cryogenic Engineering*, edited by K. D. Timmerhaus (Plenum Press, New York, 1968), Vol. 13, pp. 384–396.
5. P. C. Souers, *Hydrogen Properties for Fusion Energy* (University of California Press, Berkeley, 1986), p. 52.
6. Fluitron, Inc., Ivyland, PA.
7. This type of oil is "Tellus 10" made by Shell Oil Company, Houston, TX.

Modeling the Temperature and Ice-Thickness Profiles Within OMEGA Cryogenic Targets

Introduction

Cryogenic targets for direct-drive experiments on OMEGA require a 100- μm -thick layer of solid hydrogen isotopes (DT or D_2) uniformly distributed around the inside of a thin-walled (1 μm), 1-mm-diam polymer capsule. This uniformity is achieved by maintaining the capsule in a uniform and stable thermal environment where the inner and outer ice surfaces are each positioned along a single isotherm. The hydrogen fuel is layered¹⁻³ in the following sequence: the capsule is permeation-filled with gaseous DT or D_2 ; the gas is cooled to the liquid phase, then gradually cooled through the triple point; polycrystalline DT or D_2 solid expands from a single nucleation site. Heat provided during cooling through the triple point is needed to sublime the hydrogen ice from regions where the ice is thickest and redeposit it where ice is thinnest to form a uniformly thick layer. For solid DT this energy is provided by the radioactive decay of a triton atom, which produces an electron with a mean energy of 4.6 keV and provides 12 μW of uniform bulk heating in an OMEGA target. D_2 layers require an external source of heat, which is provided by an IR light source operating at the strongest vibrational-rotational absorption frequency of the D_2 lattice (3.2 cm^{-1}).

The allowed deviation of the inner ice layer from a completely smooth symmetrical geometry is less than 1- μm rms for all spherical Legendre modes $\ell < 50$.⁴ This demanding specification requires a diagnostic technique that is capable of measuring how accurately the capsule is positioned along the isotherms within the layering sphere. The only available technique with the requisite sensitivity is the interferometric technique used to measure the smoothness of the ice layer.⁵ The uniformity and smoothness of the ice are the best measures of the thermal environment in the layering sphere. Since the interferometric technique is also in development, additional information is needed to understand the thermal environment present in the layering sphere to allow us to iterate the layering and characterizing development process. This information can be obtained only by numerical simulation and is needed to define the initial layering conditions. As experimental data becomes available, the theoretical model can be refined.

This work is an initial endeavor to develop a numerical model of the thermal conditions of a cryogenic target inside the layering sphere. The layering sphere is a spherical cavity containing two sets of orthogonal windows for viewing and a hole for inserting and removing the target. The temperature gradients within the ice are calculated for specific conditions and nonuniformities inside the layering sphere. This allows the pressure inside the capsule and the ice thickness to be calculated from the measurable temperature on the layering sphere. The numerical simulations are validated against analytic solutions where possible. The sensitivity of the ice layer's uniformity to the effects of three principal nonuniformities are calculated: (1) misalignment of the capsule from the center of the layering sphere; (2) variability in the uniformity of the capsule wall thickness; and (3) temperature gradients on the internal surface of the layering sphere. Knowing the magnitude of these effects will guide our target fabrication and cryo-engineering research priorities.

A commercially available computational fluid dynamics (CFD) code *FLUENT*⁶ is used to model the cryogenic target in the layering sphere. This code employs an advanced variable-size mesh generation mechanism that provides maximum computational resolution where it is most needed. *FLUENT* also possesses two properties that are required for more sophisticated modeling: (1) it allows mass transport to be calculated concurrently with thermal calculations, and (2) it has the provision to model condensation, an integral component of the layering process.

Two-dimensional (2-D) axisymmetric models of the environment, which included the layering sphere, exchange gas, target capsule, and DT-ice layer, were used for the calculations. The models were created with *GAMBIT* (Fluent, Inc.) geometry/mesh generation software, the companion program to *FLUENT*. For these initial calculations, the target mount, layering sphere windows, and target-extraction hole were not included in the models. The geometry of the environment, along with the meshing scheme, is shown in Figs. 81.11 and 81.12. A finer mesh was used in the ice and capsule, where

greater temperature resolution was required, while a gradually coarser mesh was used in the exchange gas extending to the layering sphere's inside surface. The cell size in the ice was $10 \times 10 \mu\text{m}^2$, and the complete environment totaled over 15,000 cells.

The layering sphere had an inside diameter of 25.4 mm. The capsule, which was centered in the layering sphere (unless decentered for modeling purposes), had an outside diameter of $950 \mu\text{m}$ and a wall thickness of $2 \mu\text{m}$. The DT ice was a $100\text{-}\mu\text{m}$ -thick layer on the inside of the capsule. The geometry was considered symmetric about the vertical axis; therefore, only half the overall geometry was modeled. A 50-mTorr helium exchange gas was placed in the layering sphere to allow heat conduction between the target and the layering sphere.

With this model the dimensions (thickness) of the capsule and ice could be readily changed, simulating capsule non-uniformities and DT layering, respectively. Also, the target's position within the layering sphere could be changed easily. This flexibility allowed many situations to be modeled, and the steady-state ice-thickness profile was calculated iteratively.

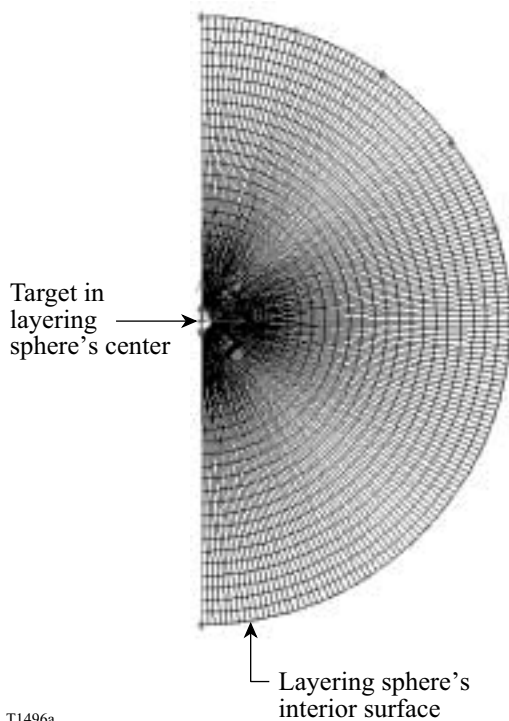


Figure 81.11
Axisymmetric 2-D geometry/mesh of the target capsule, DT ice, helium exchange gas, and layering sphere's interior surface used in the CFD simulation. The inside diameter of the layering sphere is 25.4 mm, and the outside diameter of the capsule is $950 \mu\text{m}$.

The temperature-dependent properties of the materials in the model were used at 18.5 to 20 K whenever possible. The properties of the capsule material—polyimide (Kapton)—were taken from literature and product specifications supplied from DuPont. These are listed in Table 81.I.

To first order, a uniform and stable thermal environment will produce a uniform hydrogen fuel layer if a perfectly spherical capsule with a uniformly thick wall is positioned at the center of an isothermal layering sphere. In actual operation, deviations from ideality exist, which will affect the uniformity of the ice. The following three models were generated to calculate the magnitude of these deviations from ideality on the steady-state temperature and ice-thickness profiles.

Case 1: Misalignment of the Target from the Center of the Layering Sphere.

The target can be moved within the layering sphere using a four-axis motion controller (x, y, z, θ) with an absolute encoder defining its position. The primary goal is to make fine adjustments to position the target at the center of the target chamber for the implosion. Generically, it is known that centering the

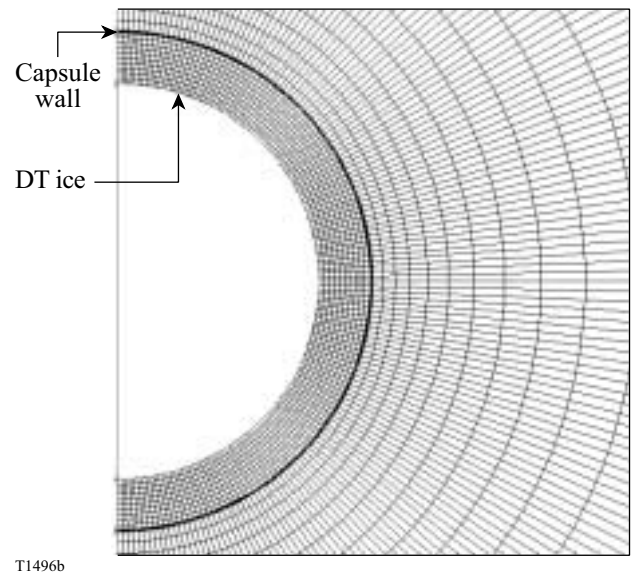


Figure 81.12
Close-up view of the geometry/mesh of the capsule and DT ice used in the CFD simulation. The DT ice is $100 \mu\text{m}$ thick, and the capsule is $2 \mu\text{m}$ thick.

Table 81.I: Properties of the materials used in the CFD simulation.

	Solid DT ⁷	Polyimide (Kapton) ^{8,9}	Helium at 50 mTorr ¹⁰
Thermal conductivity k (W/m K)	0.35	0.05	0.0227
Heat capacity C_p (J/kg K)	2720	130	5600
Density ρ (kg/m ³)	257.6	1500	0.0002
Heat-generation rate Q (W/m ³)	51000	0	0

uniform target in the layering sphere is critical to achieve a uniform ice layer; however, the sensitivity of the target’s position in the uniformity layering sphere to the ice is not known. When the center of the target does not coincide with the center of the layering sphere, the side of the capsule farthest from the layering sphere’s surface will be warmer than the side closest to the layering sphere. (The cooler walls of the layering sphere act as a heat sink for the heat-generating target.) This results in a nonisothermal inner-ice-surface temperature and a consequent thinning of the ice from the warmer side. At steady-state conditions an ice-thickness nonuniformity is created.

Case 2: Capsule-Wall-Thickness Nonuniformities.

Direct-drive target capsules have been produced with a high degree of uniformity in dimension and thickness.¹¹ The current method of measuring the variability in the wall thickness is white-light interferometry and has an accuracy of one interferometric fringe $\sim 0.3 \mu\text{m}$. This case studies the effect of a capsule nonuniformity, which is too small to be measured, on the ice thickness. (If it is found to be significant, a more accurate method will have to be used to select quality capsules.) These nonuniformities in the capsule wall can lead to thermal gradients in the ice as thinner areas in the wall offer less thermal resistance to heat loss to the exchange gas than do thick ones. As research continues on engineering precise uniform capsules, the effects that nonuniformly thick capsules have on cryogenic layers must be calculated.

Case 3: Temperature Gradients on the Inner Surface of the Layering Sphere.

During calculations for Cases 1 and 2, it was assumed that the layering sphere was isothermal; that premise will be investigated here. In this case, the effects that a temperature nonuniformity over 12% of the layering sphere’s inner surface will produce in the target at the center of the layering sphere were calculated. The source of the heat load could be (1) a localized, small thermal short to an adjacent shroud along an instrumentation sensor or the optical fiber used for IR layering and/or

(2) heating on the windows during IR layering and target viewing, and from external radiation. Depending on the magnitude of the temperature nonuniformity, polar and azimuthal temperature gradients may develop in the ice. The effects of these heat sources must be identified by calculations so they can be minimized by engineering.

The most obvious initial concern—heating caused by room-temperature radiation—is not expected to be a significant contributing factor: radiation will be absorbed in the windows (BK glass) of the first stage of the cryocooler, which are at 45 K. Less than 0.4% of the light is transmitted by these 1-mm-thick glass windows. (Re-radiation from these windows at 45 K through the layering sphere’s sapphire windows was calculated to heat the target by less than 20 nW, which is negligible.)

The Target Viewing System (TVS) is used to illuminate and view the target when it is positioned in the center of the target chamber. Absorption of this radiation in the sapphire windows is a contributor to a nonuniform layering-sphere temperature. The source is filtered to 532 nm with a bandwidth of 40 nm, and the heat load is localized around the windows. Because of the excellent thermal conductivity of the copper layering sphere, that area is expected to have a temperature nonuniformity of the order of 1 mK. (If the illumination source is unfiltered, the heat absorbed in the sapphire window is $\sim 40 \text{ mW}$.)

A nonisothermal layering-sphere surface will transmit its effects into the surrounding helium exchange gas, which will produce an uneven heat load on the capsule. The nonuniform capsule environment will result in a shift in the target isotherms to create a nonuniform cryogenic-fuel layer.

Solution Procedure

Separate models were developed to determine the sensitivity of the smoothness of the DT ice to deviations from ideal boundary conditions that may be expected in actual operations. This was done to identify those parameters that most affected

the layer's smoothness. Only heat transfer via conduction was modeled: the pressure of the helium exchange gas (50 mTorr) is too low for convection to contribute to heat flow, and the small temperature gradients between the capsule and the layering sphere preclude a significant radiation effect. (A more complicated refinement to be added later will incorporate mass transfer and the presence of helium inside the capsule into the model. This will allow the dynamics and time dependency of the layering process to be determined. These capabilities will be needed to complement the experimental observations.)

An iterative procedure was used to calculate the final ice profile. Initially, the ice was defined as a uniformly thick layer inside the capsule to calculate the heat generation and the temperature gradient over the ice thickness. Next, a new boundary condition was established to introduce a perturbation of interest, and the resultant temperature profile in the ice was calculated. The ice's void was offset, with the void remaining spherical, to alter the ice thickness and to simulate the layering process. (The solid, which has a temperature-dependent vapor pressure, sublimates and diffuses from the warmer surfaces to the colder surfaces, where it condenses). The simulation was repeated with the adjusted ice geometry, and new temperature profiles were calculated. The process was repeated until the temperature difference on the internal surface of the ice was minimized. At this approximately uniform ice temperature the net transfer of DT would be approximately zero. This convergent configuration was the best approximation of the steady-state ice profile that can be achieved with a spherical void for the prescribed boundary condition.

Results and Discussion

1. Analytical Solutions

An initial, idealized model was created to determine the temperature profile of a uniform spherical ice layer. This model was used for two reasons: (1) to determine the thermal parameter space expected inside the target layering sphere, and (2) to compare the numerical solution to the analytical result to ensure the model was functioning correctly. The model consisted of a uniform 100- μm DT-ice layer inside a 2- μm -thick polyimide capsule with the temperature of the outer layer of the ice constant at 19.5 K (the defined boundary condition). The DT was self-heated with a volumetric heating rate of 51,000 W/m^3 (about 12 μW per target). The numerical simulation calculated the steady-state inner ice temperature to be 19.50065 K. Thus, a radial temperature difference of 650 μK existed between the inner and outer ice surfaces. The temperature profile is shown in Fig. 81.13. This result compared well with the following analytical result.

The steady-state governing equation¹² of a spherical shell with heat generation is

$$\frac{1}{r} \frac{d^2}{dr^2}(rT) + \frac{Q}{k} = 0, \tag{1}$$

where r is the radius, T is the temperature, Q is the heat generation, and k is the thermal conductivity. The boundary conditions are (1) the inner surface, $r = R_i$, is at T_i and the outer surface, $r = R_o$ is at T_o ; (2) no heat transfers from the solid to the gas (assuming negligible thermal conductivity and heat generation in the gas). The solution is given by

$$T_i - T_o = \frac{1}{6} \frac{Q}{k} \left[R_o^2 - R_i^2 - 2R_i^3 \left(\frac{1}{R_i} - \frac{1}{R_o} \right) \right]. \tag{2}$$

This calculation assumes spherical symmetry, i.e., uniform ice thickness and heat transfer solely in the radial direction. Using the dimensions of the ice, $R_o = 473 \mu\text{m}$ and $R_i = 373 \mu\text{m}$, and the thermal conductivity $k = 0.35 \text{ W}/\text{m K}$, the temperature difference between the inner and outer surfaces ($T_i - T_o$) was 630 μK . This result agrees within 3% of the numerical solution, validating the mesh resolution and sensitivity of the numerical approach.

A second model was created to determine the temperature profiles from pole to pole along the outside surface of a nonuniformly thick DT-ice layer. If the ice is uniform, there is no pole-to-pole temperature difference because the heat load is

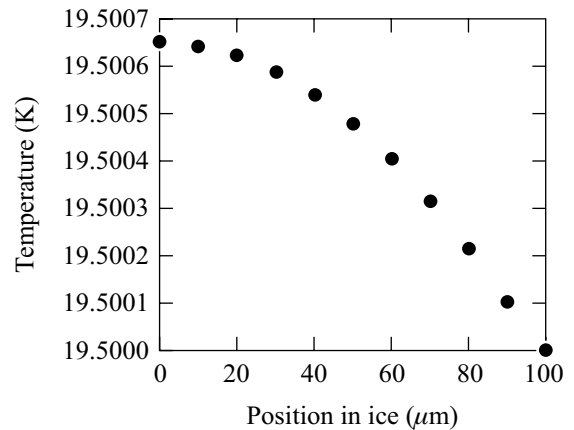


Figure 81.13 Radial temperature profile of a uniformly 100- μm -thick DT-ice layer inside an OMEGA cryo target. The outside ice surface was fixed at 19.5 K. The volumetric heating rate of DT was 51,000 W/m^3 .

symmetric. When thickness variations exist, heat can flow in the tangential direction, leading to a nonisothermal inner ice surface. To model nonuniformities, a 100- μm -thick ice layer was constructed with a 2.0- μm $\ell = 1$ nonuniformity. The model with dimensions is shown in Fig. 81.14. The isothermal boundary condition on the inner surface of the ice was 19.5 K, with all other thermal and material properties of DT the same as the previous model. The CFD simulation predicted a temperature difference ($\Delta T_o = 12 \mu\text{K}$) along the outer surface of the ice.

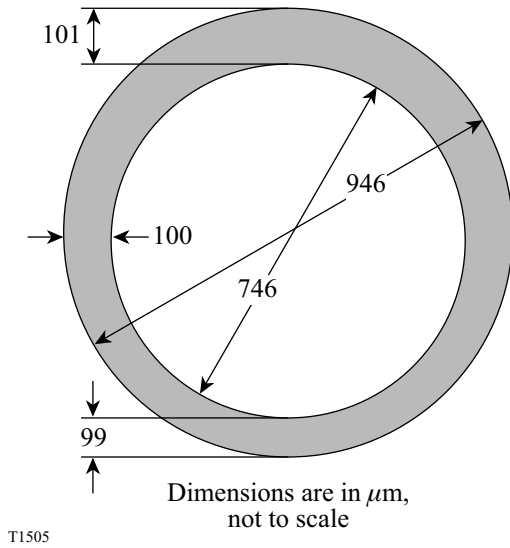


Figure 81.14
A nominal 100- μm -thick ice layer with 2- μm $\ell = 1$ nonuniformity used in the CFD simulation to determine the pole-to-pole temperature difference in nonuniformly thick DT ice.

For the analytical solution, Eq. (2) was rearranged and two calculations were performed. Each calculation gave the temperature of the outer ice surface for a given thickness. The equations were solved by using the inner-surface boundary condition:

$$T_i = \frac{1}{6} \frac{Q}{k} \left[R_o^2 - R_{i1}^2 - 2R_{i1}^3 \left(\frac{1}{R_{i1}} - \frac{1}{R_o} \right) \right] + T_{o1}$$

$$= \frac{1}{6} \frac{Q}{k} \left[R_o^2 - R_{i2}^2 - 2R_{i2}^3 \left(\frac{1}{R_{i2}} - \frac{1}{R_o} \right) \right] + T_{o2}, \quad (3)$$

where the indices “1” and “2” on the radii and temperatures indicate two different locations. By solving the equations with

real radii and properties (shown in Fig. 81.14) and allowing the indices 1 and 2 to refer to the north and south poles, respectively, the temperature difference along the outer ice surface ($\Delta T_o = T_{o1} - T_{o2}$) was 14 μK . This result agrees within 17% of the numerical solution above.

2. Numerical Simulations

The two models above determined the thermal parameter space and compared well with the analytical solutions. The next task was to calculate the effects of realistic perturbations to the system on the DT-ice temperature and thickness profiles. For these more complicated situations, no simple analytical solution existed against which to compare; instead, the numerical models were used to predict the profiles.

Case 1: Misalignment of the target from the center of the layering sphere.

In this model the target was shifted from the center of the layering sphere as shown in Fig. 81.15. The figure depicts the centers of the target and layering sphere offset by 1 mm, about one target diameter. The interior surface of the layering sphere is isothermal at 19.2 K (the prescribed boundary condition). The capsule and DT ice were initially uniform 2 μm and 100 μm thick, respectively. The calculated temperature profiles in the DT ice and vapor space prior to layering are shown in Fig. 81.16. Since the bottom of the target was farthest away from the colder layering sphere, it had the relatively warmer inner ice surface. The pole-to-pole temperature difference along the inner ice surface caused by the target misalignment of 1 mm was 85.5 μK .

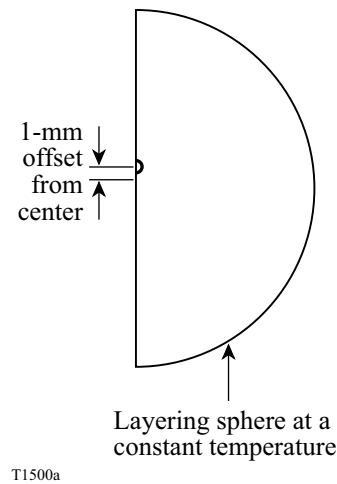


Figure 81.15
Axisymmetric model of a target offset from the center of the layering sphere.

The next step of the simulation was to determine the expected shift in ice thickness caused by the temperature difference on the inner surface. Since the bottom part of the target was warmer, the temperature-dependent vapor pressure of DT above the ice was greater than where the ice was colder. The resulting pressure gradient would create a net mass transfer of DT to the colder, upper half of the target where it condenses on the ice surface. This reduces the ice thickness at the bottom of the capsule and increases it at the top. The semi-circle that represented the inner ice surface was shifted downward to represent the thinning of the lower layer and thickening of the upper layer of DT. Following the iterative solution procedure described previously, the ice's void was manually varied to simulate layering, and the simulation was repeated until the pole-to-pole temperature difference along the ice surface was approximately zero. This occurred when the total ice $\ell = 1$ nonuniformity was $1.1 \mu\text{m}$. (The ice thicknesses at the north and south poles were $100.55 \mu\text{m}$ and $99.45 \mu\text{m}$, respectively.)

The simulation was repeated for different values of the misalignment of the target from the layering sphere's center. The inner ice pole-to-pole temperature differences before redistribution caused by different target offsets are listed in Table 81.II. The corresponding $\ell = 1$ nonuniformities in the DT layer resulting from the offsets are displayed in Fig. 81.17. Using the $\ell = 1$ mode for these analyses is a reasonable compromise as it is the dominant contribution to the total rms roughness⁴ and makes the calculation tractable. Clearly, in actual operation the change in ice thickness would be observed in additional modes of the power spectrum ($\ell > 1$); however, at

present, modeling these additional modes is beyond the scope of this article.

Case 2: Capsule $\ell = 1$ nonuniformities.

The capsule itself can produce temperature nonuniformities in the ice if the wall is not uniformly thick because the capsule's thermal conductivity is much less than that of the ice. The effects of these small perturbations required an adaption to the model. To model the sensitivity of nonuniformities of the order of tenths of microns, the scale of the area under investigation was reduced to include only the target capsule and the DT ice and vapor space. This removed the exchange gas and layering sphere from the calculations. Instead, an isothermal boundary condition on the outer capsule surface at a temperature of 19.5 K was used in all simulations.

Table 81.II: Pole-to-pole temperature difference on the inner DT-ice layer before redistribution for various offsets of the target from the center of the layering sphere.

Offset from center (μm)	Temperature difference in ice (μK)
0	0.0
500	-52.0
1000	-85.5
1500	-190.0

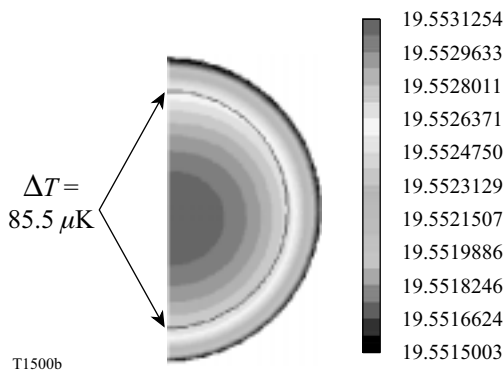


Figure 81.16 Temperature profiles in the DT ice and vapor space for a target offset from the center of the layering sphere by 1 mm. The pole-to-pole temperature difference on the inner ice surface was $85.5 \mu\text{K}$.

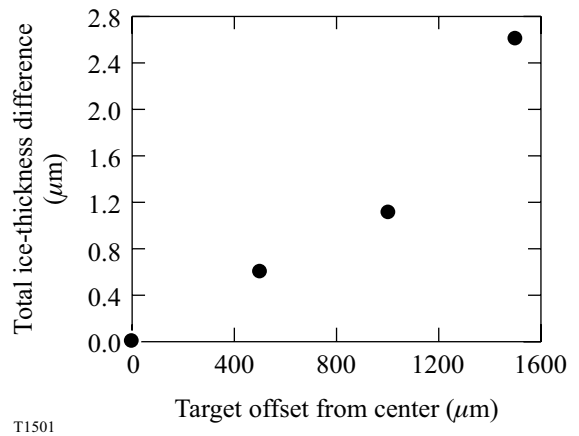


Figure 81.17 Total ice $\ell = 1$ nonuniformity in a nominal $100\text{-}\mu\text{m}$ -thick ice layer for various offsets of the target from the center of the layering sphere.

An example case is shown in Figs. 81.18–81.20. The capsule (nominal thickness $2\ \mu\text{m}$) was modeled to be nonuniform by shifting the semicircle representing the outer shell surface upward by $0.15\ \mu\text{m}$ to create a total $\ell = 1$ nonuniformity of $0.3\ \mu\text{m}$. A uniform $100\text{-}\mu\text{m}$ DT-ice layer was placed inside the nonuniform capsule; the complete geometry is shown in Fig. 81.18. Since there was a greater thermal resistance at the north pole than the south pole due to the thicker capsule wall,

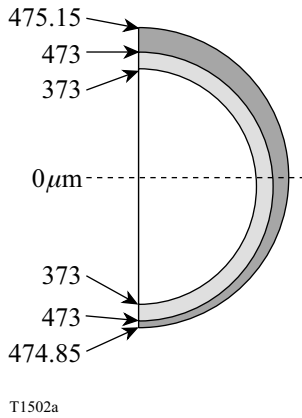


Figure 81.18
A $0.3\text{-}\mu\text{m}$ nonuniformity ($\ell = 1$) in the target-capsule thickness. The ice was $100\ \mu\text{m}$ thick. Figures are not to scale.

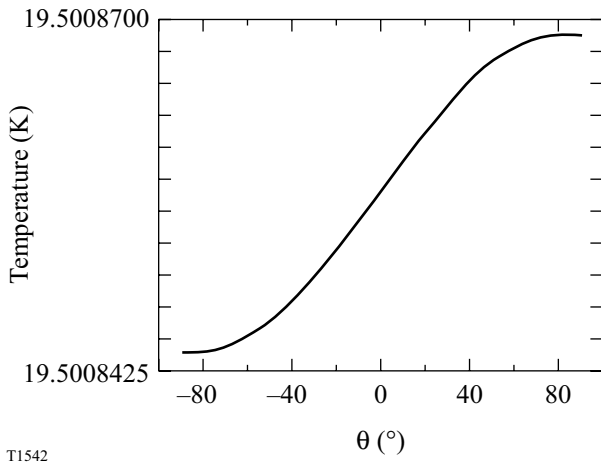


Figure 81.19
Temperature distribution along the inner surface of the ice (0° at target equator, 90° at north pole, -90° at south pole). A pole-to-pole temperature difference occurs as a result of the $\ell = 1$ nonuniformity (capsule thickness nonuniformity).

the ice was relatively warmer at the north pole. The calculated pole-to-pole temperature variation ($\sim 25\ \mu\text{K}$) along the inner ice surface is shown in Fig. 81.19. Using the iterative solution procedure, the ice thickness was shifted to simulate layering (by moving the ice’s free surface) until the temperature gradient between the poles reached zero. This result is shown in Fig. 81.20, where a total $1.86\text{-}\mu\text{m}$ ice $\ell = 1$ nonuniformity was calculated. (The ice thicknesses at the north and south poles were $99.07\ \mu\text{m}$ and $100.93\ \mu\text{m}$, respectively.) The results of simulation recreating other capsule $\ell = 1$ nonuniformities are listed in Table 81.III.

Case 3: Temperature gradients on the inner surface of the layering sphere.

In the model for this investigation, the temperature was raised by a fixed amount on an area covering 12% of the layering sphere. The remainder of the layering sphere was held at $19.2\ \text{K}$. This simulated the effect that a localized heat load on the layering sphere has on a target. The capsule and DT ice were initially uniform $2\ \mu\text{m}$ and $100\ \mu\text{m}$ thick, respectively. The resultant effects on the ice temperature and distribution were calculated for a target centered in the layering sphere.

The presence of helium exchange gas allowed temperature perturbations on the layering sphere to transmit to the target and create an uneven heat load. Naturally, the side of the capsule closer to the heat source was warmer than the opposite side. The DT ice thinned from the warmer side and redistributed on the cooler side, until the free DT surface was isothermal. The

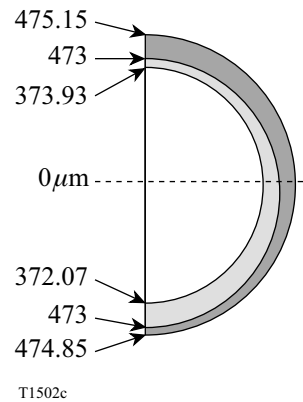


Figure 81.20
The ice’s void was shifted until zero temperature difference occurred between the poles. This was considered to be the final ice-thickness profile. Figures are not to scale.

results are listed in Table 81.IV. A 10-mK nonuniformity over 12% of the layering sphere caused a $\sim 0.5\text{-}\mu\text{m}$ ice $\ell = 1$ nonuniformity. A temperature gradient along the layering sphere greater than 10 mK must be present to change the ice thickness by a significant amount.

Summary

The temperature field within the cryogenic target is influenced by many factors, including the presence of exchange gases, target alignment within the layering sphere, target capsule thickness uniformity, temperature gradients on the layering sphere, *in-situ* target characterization methods, and external radiation. This temperature field determines the thickness uniformity of the DT-ice layer.

The temperature profile and ice $\ell = 1$ nonuniformity of the target within the OMEGA cryogenic target positioner were calculated using a thermal model in CFD simulations. The

work isolated the effect of discrete factors that affect the uniformity of the ice thickness and determined a first-order sensitivity of the ice smoothness to the effect: (1) variations in target alignment in the layering sphere, (2) capsule-thickness uniformity, and (3) temperature uniformity on the layering sphere. The resultant ice-thickness profiles were calculated for these various boundary and initial conditions.

For a target misalignment from the center of the layering sphere by 1 mm, the expected ice $\ell = 1$ nonuniformity is $\sim 1.0\ \mu\text{m}$. For a capsule $\ell = 1$ nonuniformity of $0.1\ \mu\text{m}$ in a nominal $2\text{-}\mu\text{m}$ -thick shell, the expected ice $\ell = 1$ nonuniformity is $0.6\ \mu\text{m}$. A temperature gradient along the inner surface of the layering sphere greater than 10 mK must be present to change the ice thickness more than $0.5\ \mu\text{m}$. Results from this study determine which variables have the greatest effect on the ice smoothness to guide target fabrication, layering, and cryo-engineering priorities.

Table 81.III: Pole-to-pole temperature difference before redistribution and resultant $\ell = 1$ nonuniformity for different capsule $\ell = 1$ nonuniformities.

Capsule-wall nonuniformity ($\ell = 1$) (μm)	Pole-to-pole temperature difference in ice before redistribution (μK)	Resultant ice-thickness nonuniformity ($\ell = 1$) (μm)
0.1 (1.95 to 2.05)	9.5	0.6 (99.7 to 100.3)
0.3 (1.85 to 2.15)	24.5	1.86 (99.07 to 100.93)
0.6 (1.7 to 2.3)	52.5	3.72 (98.14 to 101.86)

For an OMEGA cryo target ($2\text{-}\mu\text{m}$ capsule wall, $950\text{-}\mu\text{m}$ OD, $100\text{-}\mu\text{m}$ ice layer)

Table 81.IV: Pole-to-pole temperature difference before redistribution and resultant ice $\ell = 1$ nonuniformity for temperature gradients over 12% of the area of the layering sphere.

Temperature gradient over 12% of layer sphere area (mK)	Pole-to-pole temperature gradient in ice before redistribution (μK)	Resultant ice-thickness nonuniformity ($\ell = 1$) (μm)
5	15.4	0.34
10	28.7	0.54

ACKNOWLEDGMENT

This work was supported by the U.S. Department of Energy Office of Inertial Confinement Fusion under Cooperative Agreement No. DE-FC03-92SF19460, the University of Rochester, and the New York State Energy Research and Development Authority. The support of DOE does not constitute an endorsement by DOE of the views expressed in this article.

REFERENCES

1. J. K. Hoffer and L. R. Foreman, *Phys. Rev. Lett.* **60**, 1310 (1988).
2. A. J. Martin, R. J. Simms, and R. B. Jacobs, *J. Vac. Sci. Technol. A* **6**, 1885 (1988).
3. J. K. Hoffer and L. R. Foreman, *J. Vac. Sci. Technol. A* **7**, 1161 (1989).
4. T. R. Dittrich *et al.*, *Phys. Plasmas* **5**, 3708 (1998).
5. Laboratory for Laser Energetics LLE Review **79**, 131, NTIS document No. DOE/SF/19460-317 (1999). Copies may be obtained from the National Technical Information Service, Springfield, VA 22161.
6. Version 5.0, Fluent, Inc., Lebanon, NH.
7. P. C. Souers, *Hydrogen Properties for Fusion Energy* (University of California Press, Berkeley, 1986).
8. H. Yokoyama, *Cryogenics* **35**, 799 (1995).
9. Kapton product literature, DuPont® High Performance Polymers, Circleville, OH.
10. "NIST-Thermophysical Properties of Pure Fluids," computer code, NIST Std. Ref. Database 12 (1992).
11. F. Y. Tsai, E. L. Alfonso, S.-H. Chen, and D. R. Harding, "Mechanical Properties and Gas Permeability of Polyimide Shells Fabricated by the Vapor Deposition Method," to be published in *Fusion Technology*.
12. J. R. Welty, C. E. Wicks, and R. E. Wilson, *Fundamentals of Momentum, Heat, and Mass Transfer*, 3rd ed. (Wiley, New York, 1984), p. 247.

Target Detection and Shroud Pull Sequencing for Cryogenic-Target Operations on the OMEGA System

Introduction

The long-term plan for the upgraded OMEGA laser system includes continued improvements in beam quality, beam-to-beam energy and power balance, and the incremental addition of several beam-smoothing techniques. Incorporating the capability to shoot “cryogenic” targets is also part of the plan. Integration and activation of the Cryogenic Target Handling System is in progress as of this writing. This article introduces the elements of cryogenic-target operations and details the technique that will ensure correct and safe sequencing of cryogenic shots.

1. Cryogenic Operations

A cryogenic target is a ~1-mm-diameter spherical shell that is processed at very low temperatures and delivered to the target chamber with the fuel frozen as a layer of “ice” approximately 100 μm thick on the inside surface of the shell. These targets can contain significantly more fuel than the normal, room-temperature, gas-filled targets. Figure 81.21 illustrates how cryogenic targets are suspended by spider’s silk from a beryllium “C” mount (see description in the **Target Filling** section, p. 7, this issue).

Figure 81.22 shows the equipment installed in the OMEGA target area to allow cryogenic targets to be positioned and shot. The lower pylon, supported by the target chamber (TC), extends downward from the center of the TC and through the Target Bay floor; this lower pylon is basically a cylindrical vacuum vessel fitted with a kinematic dock inside its upper end and an isolation valve and flange at its lower end. The upper pylon extends from above the center of the TC, through a bellows joint at the top of the TC; it is supported by the bridge structure that spans the Target Bay. The linear induction motor and shroud retractor, which are housed within the upper pylon, are used to remove a thermal shroud that protects the target until shot time.

Figure 81.23 shows the elements at the center of the TC in more detail. The target is housed in a moving cryostat (MC) that is placed at the center of the TC by the lower pylon equipment.

The position of the target can be checked and adjusted using the standard OMEGA Target Viewing System and the positioner built into the MC. The OMEGA system may then be charged and sequenced to shoot the target. The charging and countdown take approximately 3 min. In the last second, the shroud retractor is commanded to pull the upper shroud upward, away from the target, so that it is clear of the beams before the laser pulse arrives.

Cryogenic targets are produced by permeating deuterium or deuterium/tritium fuel into the shell at pressures of up to 2000 atm and then cooling the assembly to below 20°K. The



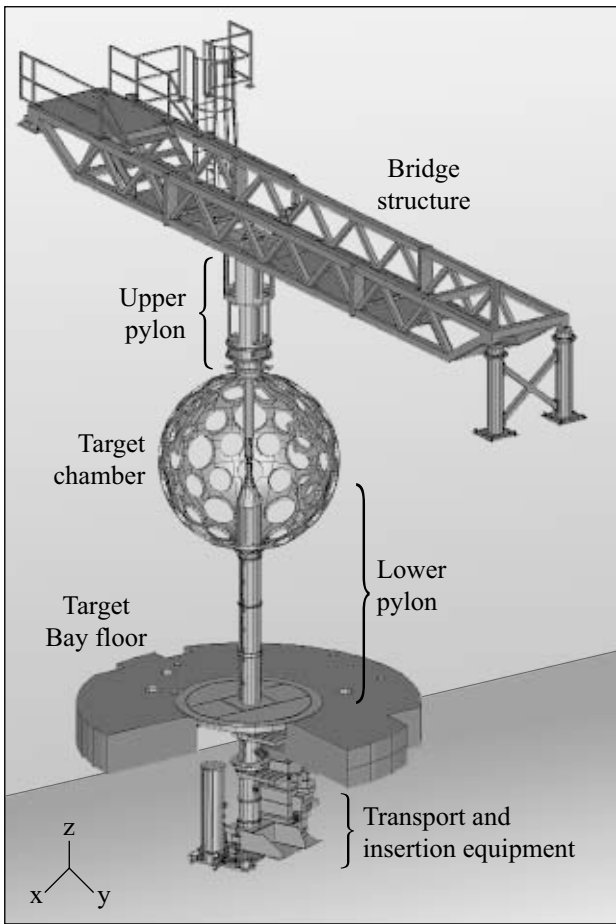
G3970

Figure 81.21
Cryogenic targets utilize a “C” mount configuration that minimizes the mass in the vicinity of the target and does not obscure any of the 60 OMEGA beams.

MC maintains a cold environment around the target while it is moved from the permeation site, completes its preparation cycle, and is moved to the center of the target chamber. Figure 81.24(a) shows the base of the MC; Fig. 81.24(b) shows the components that make up the upper shroud. The inner, middle, and outer shrouds are joined to form a single upper-shroud assembly that can move in a vertical direction over the target and mate with the lower shrouds on the base. In this configuration, the target is centered in the “layering sphere,” which is a metal cylinder with an internal spherical cavity that is controlled to provide the low-temperature, spatially uniform radiation environment that promotes formation of a smooth, concentric ice layer. Windows in the layering sphere, the middle shroud, and the outer shroud allow the target to be viewed along

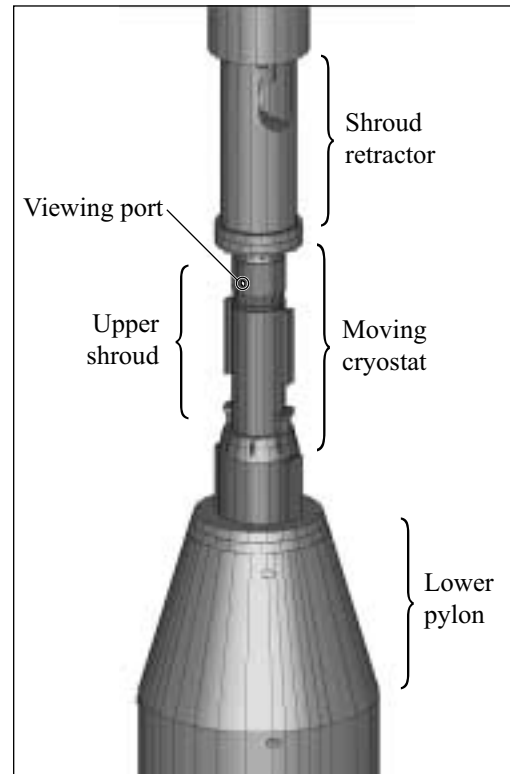
two axes by the Target Viewing System (TVS), which is used to position objects in the OMEGA target chamber.

The MC transport cart mounts all of the cooling, vacuum, and control equipment required to maintain the MC at the required low-temperature, high-vacuum condition. A major feature of the transport cart is an evacuated umbilical spool that manages the electrical and fluid lines that connect the MC to the equipment on the cart. Figure 81.25 shows the transport cart. In this view, the cryostat is located below the large gate valve near the top of the cylindrical vacuum vessel (left of center). The entire transport cart is mounted on a pneumatic bearing system that allows operators to push it from place to place within the facility. A total of five transport carts are planned.



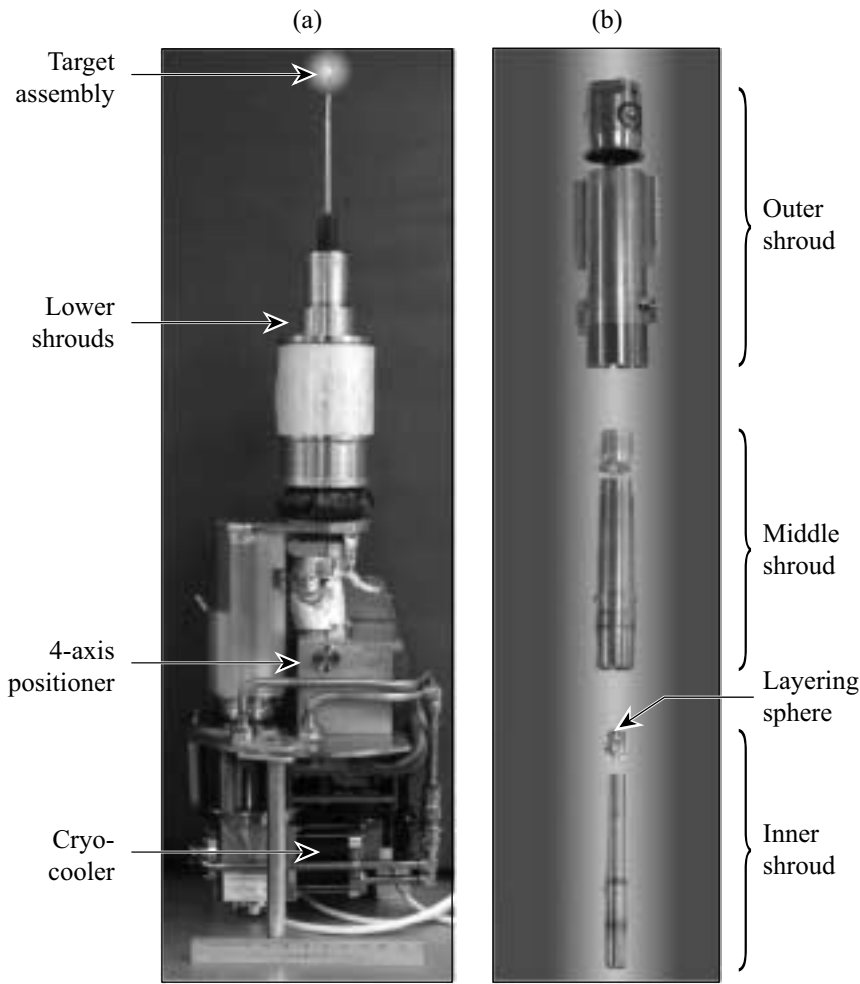
G4941

Figure 81.22
The major equipment items recently installed in the OMEGA target area to facilitate cryogenic target shots include transport and insertion equipment beneath the target chamber, upper and lower pylons, and a structural bridge.



G4942

Figure 81.23
The cryogenic target is housed in a moving cryostat (MC) that is placed at the center of the target chamber. The MC includes thermal shrouds that isolate the target from the room-temperature target chamber environment. The shroud retractor removes the upper shroud just prior to the shot.



T1461&1462

Figure 81.24

Parts of the moving cryostat: (a) The base includes a target positioner, a cooler, and the lower protective shrouds; (b) the upper shroud is a three-layer assembly. The layering-sphere element that immediately surrounds the target provides a spatially uniform radiation environment that determines the properties of the ice.

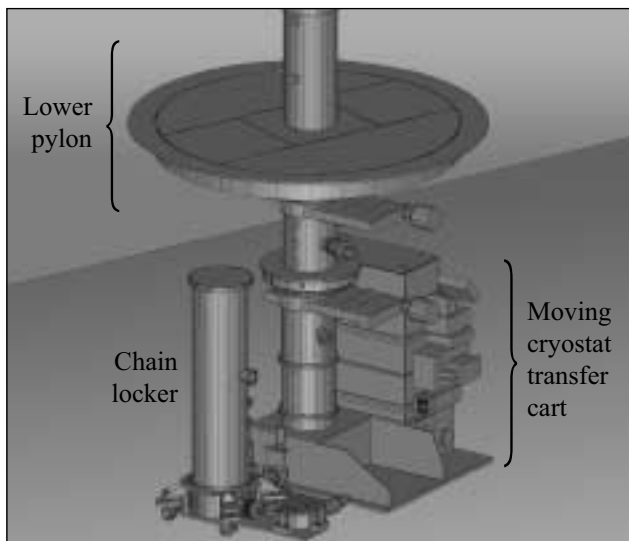
Figure 81.25
The moving cryostat transport cart carries the moving cryostat and its cooling, vacuum, and control equipment. It is moved around the facility on a pneumatic bearing system.



T1463

Figure 81.26 shows the lower pylon, in the room below the target chamber, with the transport cart docked to it. The vertical cylinder in the foreground is an evacuated “chain locker.” When the system is ready, the isolation gate valves are opened, and the MC is driven to the center of the target chamber by the action of the chain being driven out of the locker and along guide rails inside the transport cart and lower pylon vacuum vessels. When it arrives at the center of the target chamber, the MC mates with the kinematic dock built into the lower surface of the top of the lower pylon and is clamped into place. This places the layering sphere and target within approximately 100 μm at the convergence of the laser beams.

The linear induction motor (LIM) in the upper pylon can then be operated to lower the shroud retractor from above to engage the upper shroud and prepare it for removal (this configuration is shown in Fig. 81.23). The shooting sequence includes commanding the removal of the upper shroud so that it is clear of the beams before the pulse arrives, assuring that the target is intact and in place, and preventing the laser pulse from propagating if a problem is detected. The details of this final sequencing, detection, and shot authorization process are performed by the cryogenic target detection equipment described in this article.



G4943

Figure 81.26

For an OMEGA shot, the transport cart is positioned under the lower pylon and connected to it. A compression chain system is used to drive the moving cryostat upward into the target chamber.

2. Cryogenic Target Detector

Because the beam ports on OMEGA’s target chamber are arranged in opposing pairs, energy propagated forward in one beamline can pass through the chamber and propagate in the backward direction on the opposing beam train. This feature is exploited routinely in alignment procedures that use low-energy laser beams. High-value optics can be seriously damaged, however, if even a fraction of the high-energy shot pulse is allowed to pass the target and enter the opposing focus lens. “Target existence detectors” have been put into place to help prevent this from happening. The automatic imaging target existence detector (AITED)—a system used on noncryogenic target shots—protects against the situation where a properly aligned target moves or falls out of position late in the shot cycle. The cryogenic target detector (CTD) performs the same functions in the altered circumstances dictated by cryogenic-target operations. (The Target Viewing System cannot be used for target detection in either case because its lenses extend well into the target chamber and are protected from flash and debris by rugged shutters. Because these shutters require approximately 10 s to close, they are closed and verified prior to charging the laser system.)

AITED is designed to deal with targets of any shape (planar or spherical) positioned at any location near the target chamber’s center. It features a single video camera to view a backlighted image of the target using an arrangement of lenses mounted outside the target chamber. Since it functions by processing video frames at 30 Hz, AITED is useful until about 30 ms prior to the shot. After the last pre-shot frame has been acquired, a fast shutter closes to protect the camera from the flash of the target event. The presence of the shroud and the sub-frame-rate timing of events prevent the use of AITED for cryogenic shots.

The CTD uses a pair of apertured photodiodes to analyze the intensity of signals provided by dedicated laser illuminators. This technique can provide detection arbitrarily close to the shot, but it is limited to spherical targets positioned at the center of the target chamber. As the design concept for the CTD developed, it was extended to include the precision timing of the shroud-retraction (or pulling) event.

Both target detectors prevent the high-energy pulse from propagating by interrupting the 5-Hz signal that triggers the power conditioning units for the regenerative amplifiers at the beginning of the laser system. The pulse that then propagates to the power amplifier stages is too low in energy to be amplified to normal levels in the remainder of the system. As a result, essentially no energy reaches the target, and damage

due to energy passing through the center of the target chamber is prevented.

Discussion

The Cryogenic Target Detection (CTD) System has been designed to meet the following requirements:

- a. Synchronize the pulling of the shroud to the laser shot.
 - Ensure that the shroud is clear of all the beams before the energy arrives at the center of the target chamber.
 - Minimize the time that the target is exposed to the target chamber's thermal radiation environment (goal: 50 ms, max).
 - Ensure that the shot occurs before the vibration caused by stopping the shroud at the top of its travel can disturb the target.
- b. Prevent propagation of the high-energy pulse if the target is not in place at the center of the target chamber.
 - Initiate detection when the shroud has cleared the target.
 - Continue to monitor as close as possible to shot time.
- c. Prevent propagation of the high-energy pulse if the target is displaced or if shroud retraction deviates from nominal.
 - Accommodate 700- to 1100- μm -diam spherical targets at the center of the target chamber.
 - Detect displacement of the target from the center of the target chamber.
 - Detect early or late exposure of the target.
 - Detect failure of the shroud to clear the beams.
- d. Provide operability and testability features compatible with OMEGA operations.
 - Provide consistent user interface look and feel.
 - Allow operator input of setup parameters.
 - Detect and display errors.
 - Implement correct responses to shot-cycle system states including "stand-down" and "abort."
 - Include test modes and signal outputs to facilitate installation, readiness checks, and trouble shooting.
 - Provide reduced functionality with one axis inoperative.
- e. Fail to the "safe" triggers-are-interrupted mode.

The major elements of the CTD include a set of detectors installed on the target chamber; a rate interrupt module (RIM), which is located in the Driver Electronics Room (DER) below the Laser Bay; and user interface software, which creates a display in the Control Room. These are shown schematically in

Fig. 81.27. The CTD uses two orthogonal optical detectors that are similar to the TVS. These elements are co-located with the corresponding TVS equipment on the target chamber but view along slightly different axes and operate independently. Because the CTD viewing axes are blocked by the edge of the viewing port in the outer shroud of the MC, target detection is not possible until the shroud has been pulled clear of the target late in the shot sequence.

The RIM is a package of electronics that is mounted in the same rack as the primary driver-timing equipment. A dedicated RS-485 serial link relays signals between the detector packages and the rate interrupt module (RIM). In addition to those associated with the detectors and illuminators these include the three shown connecting to the upper pylon controls in Fig. 81.27. The RIM also receives the T-10 and T-0 timing marks and the three 5-Hz rates that it controls from the Hardware Timing System equipment in the DER. The RIM communicates, via a standard RS-232 serial link, with a Sun workstation that contains the video frame grabber used by AITED. CTD operator interface software running on that computer provides the Graphical User Interface that is displayed on the laser drivers workstation in the Control Room.

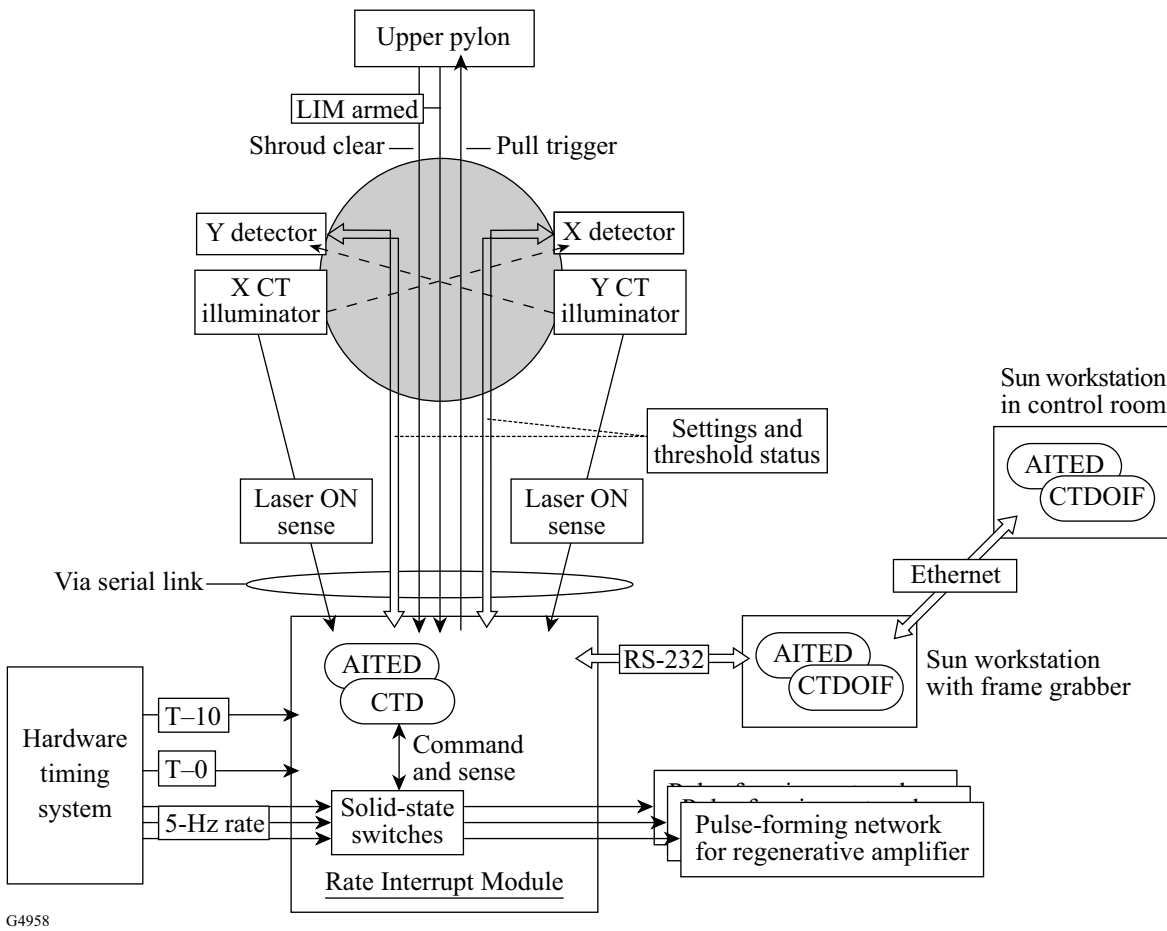
1. CTD Illuminators

Each CTD illuminator consists of a small diode laser with a collimating optical system and a fast-acting shutter. The lasers are turned on and off by a general-purpose control software item that allows the lasers to be operated manually, as needed for checkout, and automatically cued by shot-cycle software messages. The fast shutter is controlled (like the AITED camera shutter) by the hardware timing system and a dedicated controller. It closes 1 to 5 ms before every shot to prevent the flash from damaging the illuminator laser optics and re-opens automatically after the shot. A photodiode mounted in the illuminator optics provides a signal to the RIM to indicate when the laser is on, regardless of the position of the shutter.

2. Detector Packages

The CTD optics focus the illuminator laser beam into the detector package, through a manually adjustable aperture, and onto a photodiode mounted within the TVS enclosure on the opposite side of the target chamber. This system is set up so that three distinct levels of illumination can be detected:

- (a) No light means that the illuminator is either not on or is shuttered or that the MC shroud is blocking the line of sight.



G4958

Figure 81.27

The rate interrupt module (RIM) is the heart of the Cryogenic Target Detection (CTD) System. It receives signals from detectors in the target chamber, controls the triggers to the driver preamplifiers, and communicates with the Control Room operators.

- (b) A medium level means that the shroud is clear of the target and the target is in place.
- (c) A higher level means that the shroud is clear but the target is out of place.

The “low” and “high” threshold settings that make this discrimination are set by the operator and passed to the detectors for implementation. Each detector uses a Microchip PICMicro 8-bit RISC microcontroller running at 16 MHz. This microcontroller includes on-board 8-bit analog-to-digital converters that transduce the photodiode signal. I/O bits on the PICMicro’s are used to sense the illuminator status and handle the signals to and from the upper pylon. The detector packages also include RS-485 transceivers. The RS-485 standard uses differential signals that allow greater noise immunity, higher speed, and greater cable lengths than the RS-232 standard wire.

3. Rate Interrupt Module (RIM)

The RIM developed for cryogenic operations replaces the unit that was installed for AITED and is also built around the PICMicro microcontroller. The firmware running on this chip has separate AITED and CTD operating modes. The mode is determined by whether the AITED or the CTD software is running on the Sun computer. In the AITED mode, the RIM functions the same as previous versions of the RIM. In the CTD mode, the RIM implements the cryogenic target requirements. In both modes the code coordinates the activities of the RIM, including communication with the Sun, and control of the 5-Hz flashlamp triggers. Final control of the flashlamp triggers is provided by opto-isolators rather than the relays used in the previous versions of the RIM. This approach provides improved reliability and switching speed. The closed-to-open signal switching time of the rate interrupt opto-isolators has been measured as approximately 500 ns.

The overall shroud-retraction sequence must be repeatable within ± 1 ms. This allocation includes the “pull trigger” signal that originates in the RIM and is relayed over the RS-485 to the Y detector package, where it is output as a voltage level to the LIM controller in the upper pylon. The performance of the CTD elements was assessed in LLE’s Electronics Shop using the actual components connected by cables of representative lengths. The result of 20 trials is that the “pull trigger” can be timed and generated in the RIM, transmitted to the detector package, and output with an average latency of 128.8 μ s and a rms (“jitter”) of 2.6 μ s—well within the required limits.

4. CTD Operator Interface (CTDOIF)

The CTD operator interface software was developed using X/Motif Designer 5 and is designed to run under Solaris on the AITED Sun workstation to make use of the dedicated serial link to the RIM. The Graphical User Interface is displayed on the laser drivers workstation in the Control Room. Figure 81.28 illustrates the windows that are presented to the operator. The main window provides the functions for normal shot-to-shot operation of the CTD, which includes monitoring the status of

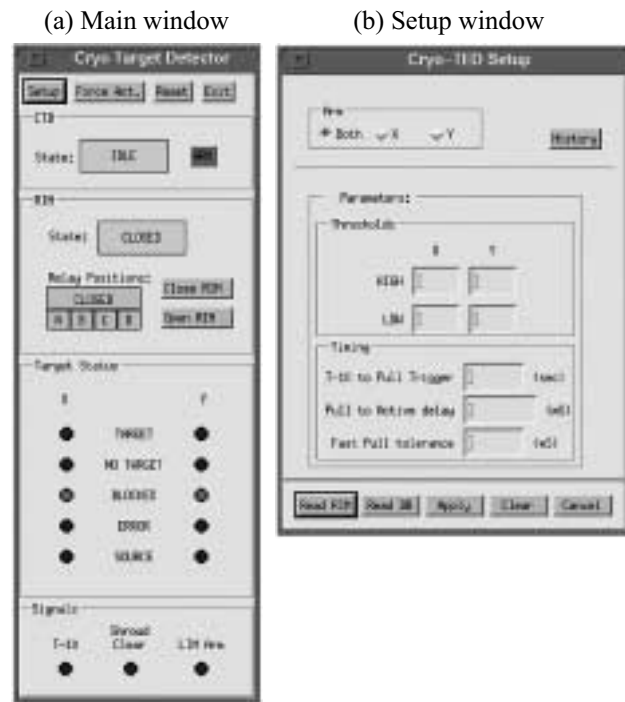
the RIM and arming the system for a shot. In particular, the status of the illuminators and the resulting signal levels at the detectors are portrayed. The setup window allows the operator to review and change the selection of axes that will be armed and the values of the RIM parameters. When revised values are applied to the RIM, they are automatically saved to the OMEGA database. The selection of one axis or both will depend on the status of the CTD hardware. Variations in target size or opacity may necessitate adjustment of the threshold values. The timing parameters will be a function of the acceleration profile that the LIM/shroud puller is commanded to follow. It is expected that once the correct set-up values have been established, they will seldom be changed.

The communication link between the Rate Interrupt Module and the Operator Interface is monitored by both elements. If communication is lost after the system has been armed for a shot, the RIM will interrupt the driver triggers. It will also abort the shroud pull if it is not too late. The OIF supports the executive-level intercommunication protocol that is used to coordinate shots. This ensures that the CTD is operated when necessary and that the operators are aware of any problems. It also allows the CTD to participate correctly in system-wide aborts or stand-downs.

5. Operating Sequence

Figure 81.29 illustrates the events in the cryogenic shot sequence. After the MC has been inserted and the target has been positioned and verified by the Experimental System operator using the Target Viewing System, the laser driver operator will verify that the CTD is set up correctly and “arm” it for the shot. In the armed state, the CTD will act in response to the events it can sense. When the CTD is not armed, the information is simply displayed to the operator.

When the entire OMEGA system is ready, the power amplifiers are charged over a period of about 2.5 min. After charging is complete, the precision timing sequence starts at T–20 s. At about T–10 s (exact timing to be determined during system activation), the pylon controller element of the Cryogenic Target Handling System initiates a “pre-pull” activity that prepares the shroud for removal. The RIM receives the “LIM armed” signal when this is complete. Meanwhile, at exactly T–10 s, the RIM computer starts a “pull timer” that counts down to the time at which the pull trigger signal must be output. Since the shroud takes about 470 ms to clear the target after it is triggered, the pull timer will run for about 9.5 s. When the pull timer expires, the RIM logic checks to ensure that it is prudent to initiate the retraction sequence. As is indicated in Fig. 81.29,



G4957

Figure 81.28 The CTD operator interface windows (a) arm the system, enable/disable the solid-state relays, and monitor status; (b) choose axes to be armed and set detection thresholds and timing values.

the pull trigger will not be output if a system-wide abort is underway or if the pre-pull did not complete successfully (as indicated by “LIM armed”) or if the CTD illuminator(s) for the axes that are armed is(are) not on at this point. (The separate function that controls the illuminators is cued by the executive-level intercommunication protocol.) In addition to inhibiting the pull trigger, these contingencies will cause the opto-isolators to be disabled, interrupting the driver pulse.

After the pull trigger has been output, the RIM logic waits until the shroud should be clear (this is timed by the “activation timer”). Figure 81.30 is a plot of the shroud trajectory that has been the baseline for the system design. The actual optimum trajectory is currently being developed on the basis of the operating performance of the LIM and its controls. The baseline features an initial constant-velocity pull that separates the upper shroud from the lower shroud. This is followed by acceleration at 2.5 g until after the time of the shot. The LIM will then decelerate the shroud to a stop at the upper end of its travel (this part of the trajectory is not shown in the plot). In Fig. 81.30, note that the shot must occur in the 4-ms window between the shroud clearing the beams (at 0.484 s) and the end of the 50-ms exposure limit (at 0.488 s). These timing values

depicted in Fig. 81.30 are also reflected in Fig. 81.29. (The critical timing parameters used by the CTD can be easily adjusted to accommodate any retraction trajectory that can be executed by the LIM.)

The shroud will clear the CTD lines of sight at the point on the trajectory marked “Target is exposed...”. This will allow the light from the illuminators to reach the detectors and will cause the lower thresholds to be exceeded. The activation timer will be set for the latest time that this can occur and still have a successful shot. If this “slow pull” limit is exceeded, the RIM will disable the opto-isolators to abort the driver pulse. This prevents shooting with the shroud in a position where it will intercept some of the high-energy laser beams. The “fast pull tolerance” [see Fig. 81.28(b)] will be set to represent the earliest time at which the shroud can clear the target and still allow a successful shot. If the illuminators are detected before the activation timer is below the fast pull tolerance, the driver pulse will be interrupted because the target could be exposed long enough to explode before the shot (the 50-ms exposure limit). In an extreme fast pull case, vibrations resulting from the shroud puller deceleration could reach the target and disturb it prior to the shot.

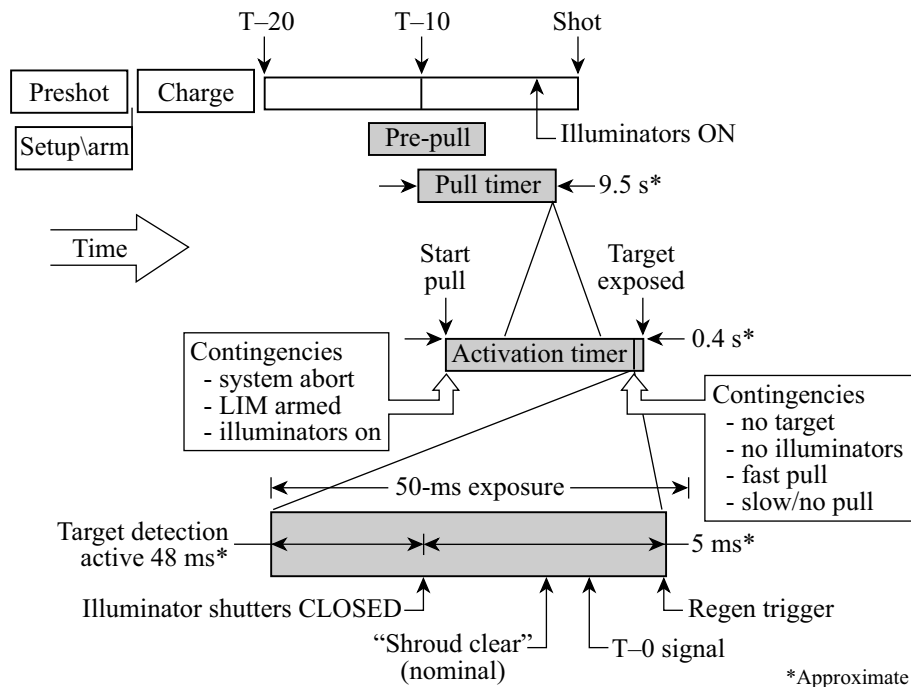


Figure 81.29 The nominal timeline for a cryogenic-target shot illustrates the increasingly precise timing of events orchestrated by the CTD system.

If the target is in place when the shroud clears the CTD lines of sight, the detector signals will be above the lower thresholds but will not exceed the upper thresholds. This is the “TARGET” situation on the operator displays and within the CTD logic. If the armed axes are in this condition, the shot and monitoring can continue until the illuminator fast shutters close a few milliseconds before $T = 0$. At that point, the signals will drop back below the lower threshold. The detection logic is then disabled. While the detection logic is active, the driver pulse will be aborted if the detector signals indicate that the target is not present or that the illuminators have failed.

The “shroud clear” signal is derived from a photosensor attached to the LIM structure. It indicates that the shroud is near the point at which it is out of the beam paths. This signal is monitored by the CTD to deal with the contingency that the shroud retractor slows down or stops after a successful initial retraction. A T-0 signal is provided to the RIM primarily as a means for disarming the target detector after the shot (so that an abort is not initiated when the target disappears due to the shot). This T-0 signal will be delayed by the timing system so that it occurs as close as possible prior to the arrival of the driver PFN triggers. If the “shroud clear” signal is received before the

T-0 signal, the shot can continue. If “shroud clear” has not been received when T-0 arrives, the opto-isolators will be disabled.

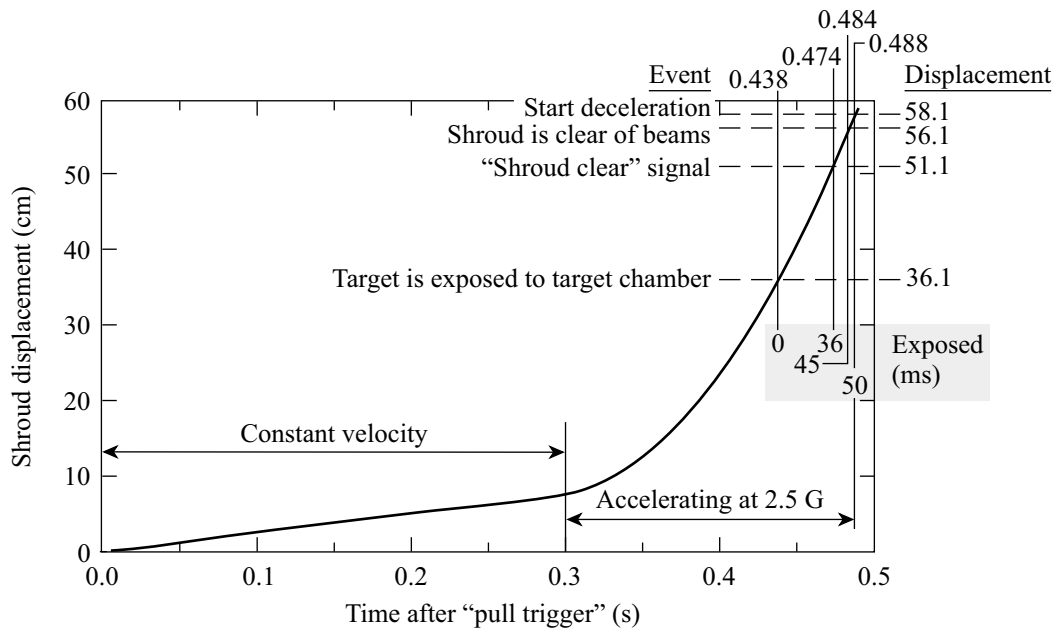
The RIM will count the time interval between the “shroud clear” and T-0 and report it to the OIF for review by the operator. These values will also be logged to the database as an indication of the shroud puller’s performance.

Conclusion

Cryogenic target detection (CTD) is a critical part of the functional integration of the Cryogenic Target Handling System into OMEGA. The newly designed CTD is based on existing elements of the OMEGA controls and will provide the necessary sequencing and safety features. The CTD setup features sufficient flexibility for the evolution of the details of cryogenic operations and target physics research.

ACKNOWLEDGMENT

This work was supported by the U.S. Department of Energy Office of Inertial Confinement Fusion under Cooperative Agreement No. DE-FC03-92SF19460, the University of Rochester, and the New York State Energy Research and Development Authority. The support of DOE does not constitute an endorsement by DOE of the views expressed in this article.



G4959

Figure 81.30 The baseline shroud-removal trajectory features constant velocity separation of the shrouds followed by constant acceleration until after the shot.

The Effect of Optical Prepulse on Direct-Drive Inertial Confinement Fusion Target Performance

Introduction

In direct-drive inertial confinement fusion (ICF), laser light directly irradiates a capsule with a pulse of less than 10-ns duration. Laser ablation of material from the capsule surface produces extreme pressure that drives the implosion of the thermonuclear fuel. Ignition target designs¹⁻³ require a temporal pulse shape tailored to produce two or more converging shocks that coalesce in the imploding core. Ideally, the implosion occurs without premature heating of the shell or the fuel contained within because preheat reduces the implosion efficiency. Since ICF targets are inherently Rayleigh–Taylor (RT) unstable, it is particularly important to direct-drive ICF that the target perturbations produced by irradiation nonuniformities³ are minimized. Another method to ameliorate the effects of this instability is to enhance ablative stabilization³ by judiciously preheating the shell with shocks produced by the rise of the drive pulse. Successful ICF implosions therefore require precise control of the temporal shape of the drive intensity and minimal perturbations of the shell by that drive.

Typically drive pulses start with a low-intensity (~2%) “foot,” several nanoseconds before the peak drive occurs. This foot is essential for producing the correct isentrope of the imploding target, i.e., one with sufficient heating to help stabilize the target but not high enough to greatly reduce its hydrodynamic efficiency. The simulations typically assume perfect optical contrast (i.e., no prepulses before the drive pulse begins). ICF lasers have high gain and experience significant saturation around the peak of the pulse; thus, low-level noise in the driver can readily produce prepulses. Since hydrodynamic target simulations generally cannot correctly model the effects of prepulses at less than 10^{-5} of the peak power, the specifications for optical contrast must be determined experimentally using target performance.

Implosion experiments^{4,5} and theoretical calculations⁶ carried out using 1054-nm lasers generally found that prepulse levels had to be kept eight to nine orders of magnitude below the peak power to obtain maximum performance (neutron yield). Corresponding optical measurement techniques^{7,8} were

also developed at that time. Since then ICF lasers and targets have changed significantly, but no new reliable experimental data exists on the effect of prepulses on target performance. Today, direct-drive targets are usually coated with a thin ($\leq 1000\text{-\AA}$) Al layer that retains the hydrogen isotopes in the gaseous fuel and prevents target damage caused by filamentation of laser light inside the target shell prior to plasma formation.^{9,10} This layer can be compromised easily by low-energy optical prepulses. Most modern ICF lasers are frequency-tripled (351-nm) Nd:glass lasers that benefit greatly from the prepulse suppression afforded by the frequency conversion. Recently Elton *et al.*¹¹ suggested that prepulses on the OMEGA laser system¹² might be higher than expected, prompting the implementation of a contrast-monitoring system on OMEGA. This work presents the measured prepulse levels on OMEGA and a contrast criterion for OMEGA direct-drive implosions. Similar contrast criteria will apply to direct-drive experiments on the National Ignition Facility (NIF).¹³

In this article several techniques for characterizing prepulses on OMEGA and their effect on target performance (i.e., neutron yield) are presented. The results indicate that the upper limit for the allowable prepulse on target is $\sim 0.1\text{ J/cm}^2$ at peak intensities of $\leq 10^8\text{ W/cm}^2$. This translates to an intensity contrast of $\sim 10^7$ between the allowable prepulse and the peak of the main laser pulse. This limit is most relevant for Al-coated targets. The allowable prepulse may be higher for uncoated targets if such targets should prove viable in the future.

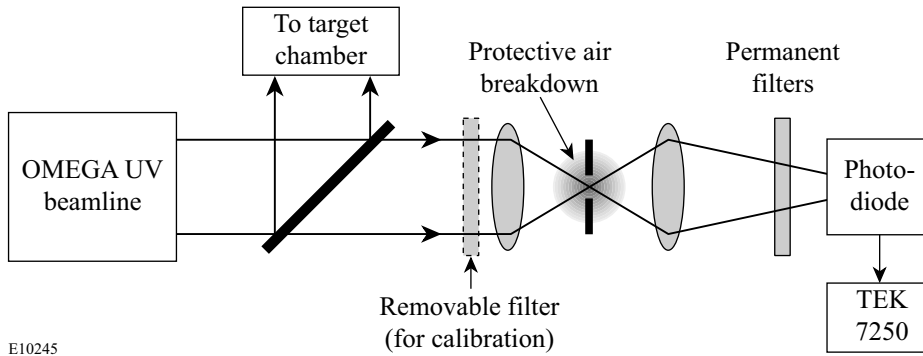
Optical Diagnostics and Their Interpretation

Optical contrast on OMEGA is measured at two places: (1) a UV contrast station located after the frequency converters and just ahead of the target chamber, and (2) an IR contrast station at the input to the amplifier chain, ahead of the first beam splitter on OMEGA. In both cases, the full beam aperture is sampled. The contrast is measured using fast vacuum photodiodes (Hamamatsu, R1328U-01-S-1 and R1328U-02-S-20) and high-speed oscilloscopes (TEK7250 or IN7101). A schematic layout of the UV contrast station is shown in Fig. 81.31. An air breakdown region is included in the design to protect the

diodes against damaging fluences during the main pulse. The prepulse monitors are calibrated with removable filters. These filters allow the main laser pulse to be fully measured on calibration shots that are typically performed daily. Removing these filters accesses the low-intensity prepulse region within 20 ns before the main laser pulse. The calibration filters have an optical density (OD) of 5.3 in the UV (2.9 in the IR), and, when removed, the detection threshold is typically around 8 orders of magnitude below the peak UV power (~5 to 6 orders of magnitude below the IR peak power). Extensive precautions have been taken to block stray light from affecting the measurements, including the spatial-filter aperture shown in Fig. 81.31. The temporal resolution of this system is better than 200 ps.

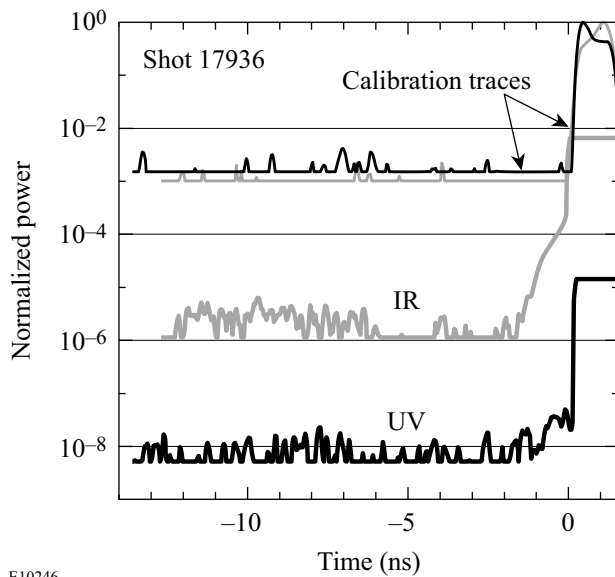
Typical prepulse records for a full-power OMEGA laser pulse are shown as the lower two curves in Fig. 81.32. The respective calibration curves with filters inserted are shown in the upper portion of this figure. (Note that their peaks are

normalized to 1.) An IR prepulse (or prepulses) can be seen rising to $\sim 10^{-4}$ of the peak IR power within ~ 1 ns of the arrival of the main pulse (the steep rise at $t=0$). The corresponding UV power is $< 10^{-7}$ of the peak UV power. The difference in contrast level between the IR and UV pulses results from both the unsaturated gain in the IR system and the nonlinear frequency conversion. [Low-power prepulses experience small-signal conversion ($I_{UV} \propto I_{IR}^3$), whereas the conversion is almost linear with the intensity near the peak of the pulse.] From simulations and experiments we have found that the prepulse contrast ratio obeys a heuristic relationship of $C_{UV} \propto (C_{IR})^2$, where $C = P_{peak}/P_{prepulse}$ (the subscripts refer to the peak and prepulse powers). This relationship is born out in the results shown in Fig. 81.32, where the UV prepulse level is mostly below the noise limit, i.e., flat portions of the trace. (The flat lines for $t > 0$ are the saturated diode signals.) The UV prepulse ($P_{prepulse} < 10^{-7} P_{peak}$) within the last nanosecond before the onset of the main pulse is very close to the detection threshold.



E10245

Figure 81.31
Schematic layout of the UV contrast monitor station. To protect the photodiode the confocal lens pair breaks down the air when the high-intensity laser pulse arrives. The removable filter pack is inserted for calibration of the prepulse monitor.



E10246

Figure 81.32
Contrast monitor traces for the UV at the output and the IR at the input to OMEGA. The thin traces on top show the calibration traces with the main pulses on scale and normalized. The thick lower traces are taken without the calibration filter (see Fig. 81.31) and permit prepulse monitoring to a contrast of 10^{-8} from the peak in the UV (10^{-6} from the peak in the IR). No prepulses are seen above the noise for times $t < -2$ ns.

The prepulse within 1 ns of the main pulse originates in either the regenerative amplifier (regen) or the pulse-shaping system before the regen. Such prepulses are only marginally affected by the Pockels cells following the regen. The general shape and position of these prepulses are reproducible although the intensity fluctuates, particularly in the UV. These observations rule out regen amplified stimulated emission (ASE), leaving spurious intracavity reflections within the regen or imperfections in the laser pulse injected into the regen as likely sources. The exact prepulse source is still under investigation.

A large number of OMEGA shots have been examined for UV prepulses; it was found that none had a prepulse in excess of 10^{-8} of the peak pulse within the time window of -17 ns and -1 ns prior to the main pulse. Within the last nanosecond the contrast degrades but the prepulse level typically does not exceed 10^{-6} of the main pulse (the corresponding cumulative time-integral of the intensity or the fluence is about 0.2 J/cm² in the prepulse) and in most cases remains at or below 10^{-7} .

Apart from UV prepulses, additional prepulses on target could be due to IR and green laser light left over from the frequency-conversion process. In each of OMEGA's 60 beams, the frequency converters are followed by two dielectric multilayer mirrors, each with nearly 100% reflectivity at 351 nm and average reflectivities of $\sim 6\%$ in the IR and $\sim 10\%$ in the green. The residual green energy is always much smaller (1%–5%) than either the UV or IR energies and can therefore be neglected. The IR intensity on target is reduced by a factor of ~ 280 because of the IR transmission of the UV mirrors. The chromatic shift of the OMEGA lenses produces IR spots of ~ 15 -mm diameter in the target plane. Since the random phase plates¹⁴ produce a UV focal spot with a FWHM of 0.5 mm and do not measurably affect the IR spot size, the IR on-target intensity is reduced by an additional factor of 900 because of this chromatic defocusing. Since there is no IR prepulse monitor at the laser output, we must estimate the IR output prepulse from the measured UV prepulse. Assuming small-signal, third-harmonic conversion efficiency for the IR prepulse [$P_{\text{IR,out}} \approx (P_{\text{UV,out}})^{1/3}$], we find that the IR on-target prepulse contrast is approximately $C_{\text{IR,on-target}} = \sim 900 \times 280 \times (C_{\text{UV}})^{1/3}$, which is $\sim 8 \times 10^7$, when the UV contrast is $\sim 3 \times 10^7$ as obtained from Fig. 81.32. Making the pessimistic assumption of 50% third-harmonic conversion efficiency for the main pulse, we find that the IR energy prepulse on target is $\sim 1/3$ of the UV prepulse energy.

An independent estimate of the IR on-target prepulse level (or contrast) can be obtained from the IR input prepulse

monitor, the ten-fold deterioration of the IR contrast due to the gain saturation in the amplifiers, and the small-signal UV conversion efficiency. Since the IR output energy can be as high as the UV energy (depending on pulse shape and duration), one can obtain an upper limit for the IR prepulse intensity on target as $I_{\text{IR,on-target,prepulse}} < [10/(900 \times 280 \times C_{\text{IR,input}})] \times I_{\text{UV,peak on-target}} \approx (4 \times 10^{-5}/C_{\text{IR}}) \times I_{\text{UV,peak on-target}}$. For $C_{\text{IR,input}} \approx 1.5 \times 10^4$ (Fig. 81.32) the upper estimate for the IR prepulse is $I_{\text{IR,on-target,prepulse}} < 10^{-8} I_{\text{UV,peak on-target}}$ which is still well below the corresponding measured UV prepulse level $\approx 5 \times 10^{-8}$ in Fig. 81.32. The two estimates of the on-target IR prepulse level (shot 17936, Fig. 81.32) lie within a factor of ~ 4 , consistent with the accuracy of these estimates.

Threshold Experiments

The thin Al coatings ($0.1 \mu\text{m}$) applied to all imploding targets on OMEGA are particularly susceptible to damage due to prepulses. To determine if prepulses had any effect on these layers, their integrity (reflectivity) was optically probed from $t \approx 15$ ns up to the arrival of the main pulse ($t = 0$). The experimental configuration for those measurements is shown schematically in Fig. 81.33. An Al-coated flat CH target was irradiated with one or six beams symmetrically arranged around the target and at $\sim 20^\circ$ with respect to the target normal (see Fig. 81.33). The Al coating was also used as one mirror of an interferometer whose fringes were temporally resolved with a streak camera.* The interferometer was illuminated with a 10-ns, second-harmonic pulse (532 nm) of a Nd:YAG laser.

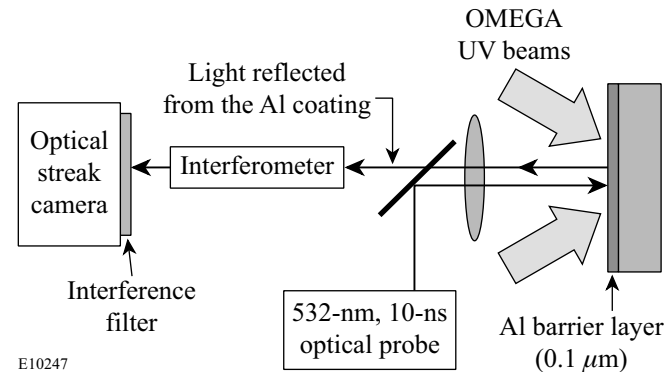
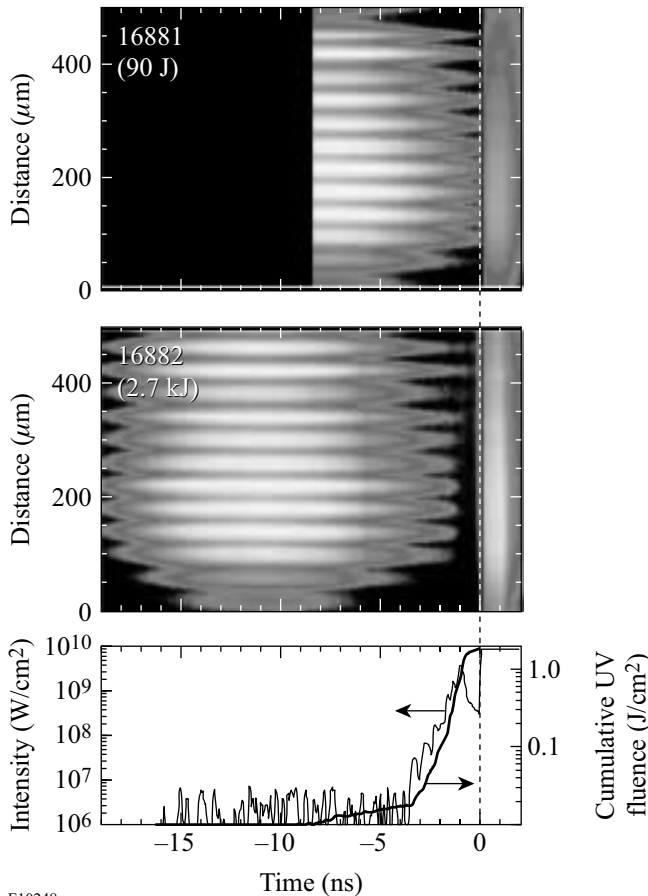


Figure 81.33 Schematic experimental setup for measuring the integrity of thin Al surface layers prior to irradiation with one or six OMEGA laser beams. The Al layer on the target acts as one end mirror for the interferometer. The target and the fringes are imaged onto a streak camera to monitor the integrity (reflectivity) of the Al. An interference filter, which protects the streak camera against excessive stray light, is required for high fringe contrast.

*This instrument [the active shock breakout (ASBO) instrument] was developed and installed on OMEGA by the Lawrence Livermore National Laboratory.

Figure 81.34 shows streaked interferometer images for two shots with Al-coated ($0.1\ \mu\text{m}$) plastic targets ($20\ \mu\text{m}$) irradiated with 1-ns square-top UV pulses containing 90 J (top image) and 2.7 kJ (lower image). The OMEGA beams were outfitted with phase plates¹⁴ that produce a spot size (FWHM) of 0.5 mm. Smoothing by spectral dispersion (SSD) was not used; OMEGA was operated with narrow bandwidth. The probe beam for the interferometer was timed primarily to determine if early prepulses ($t \leq -10\ \text{ns}$) were present, as suggested by Elton *et al.*¹¹ The beam energies for shot 16882 produced an intensity

of $8 \times 10^{14}\ \text{W}/\text{cm}^2$ on target, which is similar to that used for spherical implosion shots. (These intensities are averaged over the envelope of the beam; the actual peak intensities in the speckles can be 4 to 5 times higher.¹⁵) Shot 16881 (Fig. 81.34, top image) was a low-energy shot to test the instrument under conditions where any prepulses (if present) were expected to be below the damage threshold for the Al coating; no change in reflectivity was observed. (Note that the streak camera trigger was adjusted between the two shots in Fig. 81.34, explaining the lack of early data for shot 16881. Furthermore, the interferometer illumination beam came $\sim 1\ \text{ns}$ earlier in shot 16882 compared to shot 16881.)



E10248

Figure 81.34

Streaked interferometer fringes for two different irradiation conditions. Upper image: A low-energy shot shows interference fringes leading right up to the start of the main laser pulse. The signal to the right of $t = 0$ is due to plasma self-emission. Lower image: A high-energy shot under OMEGA implosion conditions ($I \sim 10^{15}\ \text{W}/\text{cm}^2$). The two traces are the measured UV prepulse intensity on target and the cumulative fluence on target for shot 16882. The absence of fringes in the lower part of the lower image indicates complete disruption of the Al layer at fluences $\geq 1\ \text{J}/\text{cm}^2$.

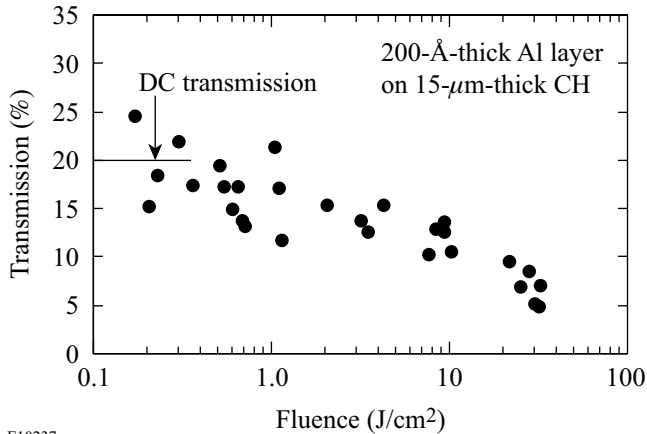
As seen in Fig. 81.34, the streaked interferometer image of shot 16882 shows no evidence of an early ($-16\ \text{ns} < t < -2\ \text{ns}$) prepulse affecting the Al surface. There is also no evidence of a prepulse in the corresponding UV diode trace for that shot. The latter, which was normalized to the peak UV intensity on target, is plotted in the graph directly below the image. The cumulative time integral (i.e., fluence) is shown in the bottom trace. This level of prepulse is higher than typical OMEGA performance but is useful because it allowed the measurement of the effects a prepulse has on the Al layer. The interferometer fringes completely disappear once the cumulative prepulse fluence reaches $\sim 1\ \text{J}/\text{cm}^2$ ($t \approx -1\ \text{ns}$ in Fig. 81.34), corresponding to a prepulse intensity of $\sim 2 \times 10^9\ \text{W}/\text{cm}^2$. Figure 81.34 also shows that the fringe contrast degrades well before the fringes disappear completely. It is likely that the disruption of the Al surface is not spatially uniform, and one expects a gradual decrease in fringe visibility as the Al layer is destroyed. Unfortunately the images in Fig. 81.34 do not allow a precise evaluation of the prepulse fluence or the intensity at which the disruption of the Al layer begins. These measurements are therefore supplemented with others to determine the effect prepulses have on target damage and target performance (see below).

Aluminum-Barrier-Layer Damage Threshold

Measurements of the UV breakdown threshold¹⁶ of thin barrier layers coated on plastic targets were carried out on LLE's tabletop terawatt laser system.¹⁷ To provide relevant interaction conditions, the output from the $1\text{-}\mu\text{m}$ -wavelength, Nd:glass laser system was frequency tripled to 351 nm and focused onto the targets with a 60-cm-focal-length lens (f number ~ 9) after passing through a binary distributed phase plate.¹⁴ In these experiments, the first minimum in the Airy pattern had a $380\text{-}\mu\text{m}$ diameter, and the characteristic speckle size was $\sim 3\ \mu\text{m}$. The experiments were carried out with 1.4-ps and 40-ps Gaussian laser pulses.

The target disruption (surface breakdown) was measured by a change in transmission through the target as a function of laser fluence. An example of the results is shown in Fig. 81.35, where the transmission as a function of laser fluence is shown for a 15- μm -thick parylene target coated with 0.02 μm of Al. The transmission was normalized to the transmission of the optical system in the absence of a target. The data show that the transmission begins to decrease when the fluence exceeds $\sim 0.1 \text{ J/cm}^2$ (defined as the damage fluence). The transmission data for both the 1.4- and 40-ps pulses were found to be indistinguishable, confirming that laser fluence, rather than intensity (factor of ~ 30 difference), determines the breakdown threshold. Other metal coatings show similar behavior.

Microscopic inspection of targets exposed to single shots showed damage to the plastic (CH) substrate at twice the threshold for observable changes in transmission.



E10237

Figure 81.35

The UV transmission as a function of laser fluence for a 15- μm -thick parylene target coated with 0.02 μm of Al. The transmission begins to decay at fluence levels above 0.1 J/cm^2 .

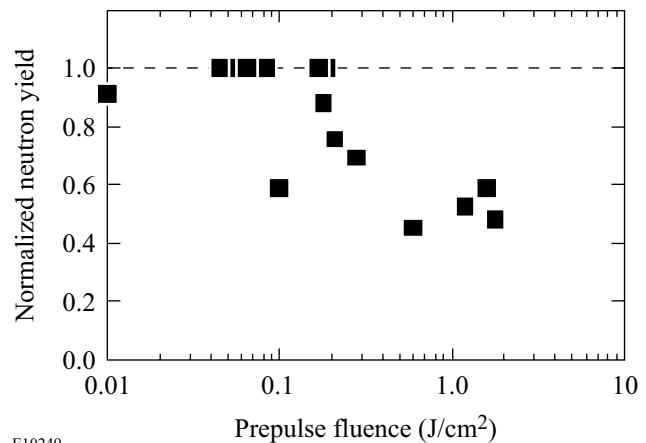
Target Performance

The effect of prepulses on capsule implosions was investigated with a series of 17 OMEGA implosions. The imploding capsules were of nearly identical diameter (896 to 908 μm) and wall thickness (19.6 to 20.5 μm) and were filled with 10 atm of D_2 . Their shells consisted of an outside CH layer ranging in thickness from 14 to 19.6 μm with an inner CH layer doped with 1% Si with a thickness ranging from 0 to 8.8 μm . All capsules were coated with 0.1 μm of Al. Two pulse shapes of 3-ns overall duration were used in these shots; one had a foot of 1 ns at the half peak intensity while the other had a similar foot at 1/8 of the peak. SSD beam smoothing was used on all

shots. The on-target UV energy ranged from 17 to 19.5 kJ for these experiments.

The prepulse monitor was used to characterize the prepulse power on these shots. The fluence was determined from the cumulative integral of that power. A scintillator-photomultiplier detector at a distance of 3 m from target center measured the DD neutron yield on these shots.

To characterize the neutron yield performance for these experiments the yields for each pulse shape and target combination were normalized to the highest neutron yield shot with that combination. In Fig. 81.36 these normalized neutron yields are plotted as a function of the measured prepulse fluence. In general, target shots with lower prepulse levels outperform those with higher prepulse levels. From this limited set of data it appears that prepulse fluence levels in excess of 0.2 J/cm^2 cause a reduction of the neutron yield by a factor of 2 compared to shots with lower prepulse levels.



E10249

Figure 81.36

Normalized neutron yield as a function of prepulse fluence level (J/cm^2) indicates degraded target performance for prepulse fluences above 0.2 J/cm^2 .

Discussion

This work quantifies the on-target irradiation contrast of the OMEGA laser and establishes an acceptable prepulse fluence criterion for high-performance ICF implosions. Of primary concern was the assertion¹¹ that, 5 to 10 ns prior to the main laser pulse, OMEGA produces prepulses that lead to plasmas with electron temperatures exceeding 100 eV. A prepulse monitor subsequently installed on OMEGA indicates that no prepulses have been observed between 20 ns and ~ 2 ns before the arrival of the main pulse; however, in the final 1 to 2 ns

before the main laser pulse, OMEGA occasionally produces a prepulse that can affect target performance.

The photodiodes that monitor the prepulse contrast in both the initial IR and final UV portions of the system are cross calibrated to the main laser pulse. The corresponding prepulse sensitivities are 10^{-6} and 10^{-8} below the main pulse intensity. Experiments that optically probe the integrity of thin Al coatings using interferometry demonstrate that the $0.1\text{-}\mu\text{m}$ Al layers are completely destroyed by prepulse fluences in excess of 1 J/cm^2 . Independent transmission measurements on plastic targets with $0.02\text{-}\mu\text{m}$ Al layers (Fig. 81.35) indicate that the transmission through these Al layers is altered when the incident fluence exceeds 0.1 to 0.2 J/cm^2 . Damage to the plastic substrate was typically observed, however, at two times higher fluences.

The neutron yields of imploding targets (Fig. 81.36) indicate that prepulse fluences of $\geq 0.2\text{ J/cm}^2$ measurably affect and decrease target performance. This prepulse “threshold” fluence is consistent with that necessary to change the transmission through thin Al layers (Fig. 81.35). This threshold fluence is significantly lower than that required to completely destroy the fringe contrast of the interferometer experiments testing the integrity of the Al layer (Fig. 81.34). The interferometer experiments show decreased contrast, however, well before the fringe visibility disappears completely. Thus the transmission experiments and the interferometer experiments support each other and are consistent with the target performance data. We conjecture that the small-scale perturbations in the Al surface layer likely serve as seed for the RT instability during the ablation phase of the implosion. These perturbations are thus amplified to levels that affect the symmetry of the implosion and thus reduce the neutron yield.

Conclusions

The contrast monitors for the OMEGA laser system are capable of sensing UV prepulses that are $\geq 10^{-8}$ of the main laser pulse. Our observations indicate that the prepulse level is below the detection threshold of 10^{-8} of the main pulse for all shots up to ~ 2 ns before the onset of the main pulse. During the last 1 or 2 ns before the main pulse, OMEGA intermittently produces prepulses up to 10^{-6} of the main-pulse intensity (with a fluence $\sim 0.2\text{ J/cm}^2$). The source of this problem is under investigation.

Optical probe experiments using interferometry show that the thin Al layers on the target surface maintain measurable fringe visibility until the prepulse fluence reaches $\sim 1\text{ J/cm}^2$,

which is attained when the prepulse reaches $\sim 2 \times 10^{-6}$ of the peak laser power. These findings are consistent with independent transmission measurements on thin ($0.02\text{-}\mu\text{m}$) Al layers that exhibit decreased transmission at fluences exceeding 0.1 or 0.2 J/cm^2 . Imploding targets also have decreased neutron yields for prepulse fluences exceeding 0.1 or 0.2 J/cm^2 . This is believed to be the result of small-scale perturbations created by laser damage in the target surface.

From the experiments reported here we conclude that precision ICF experiments on OMEGA require that the cumulative prepulse fluences be kept below 0.2 J/cm^2 corresponding to an optical intensity contrast $\geq 10^7$ on OMEGA. Prepulse requirements for NIF direct-drive targets are expected to be similar to these requirements if Al barrier layers are necessary.

ACKNOWLEDGMENT

This work was supported by the U.S. Department of Energy Office of Inertial Confinement Fusion under Cooperative Agreement No. DE-FC03-92SF19460, the University of Rochester, and the New York State Energy Research and Development Authority. The support of DOE does not constitute an endorsement by DOE of the views expressed in this article.

REFERENCES

1. R. L. McCrory, R. E. Bahr, T. R. Boehly, T. J. B. Collins, R. S. Craxton, J. A. Delettrez, W. R. Donaldson, R. Epstein, V. N. Goncharov, R. Q. Gram, D. R. Harding, P. A. Jaanimagi, R. L. Keck, J. P. Knauer, S. J. Loucks, F. J. Marshall, P. W. McKenty, D. D. Meyerhofer, S. F. B. Morse, O. V. Gotchev, P. B. Radha, S. P. Regan, W. Seka, S. Skupsky, V. A. Smalyuk, J. M. Soures, C. Stoeckl, R. P. J. Town, M. D. Wittman, B. Yaakobi, J. D. Zuegel, R. D. Petrasso, D. G. Hicks, and C. K. Li, “OMEGA Experiments and Preparation for Direct-Drive Ignition on the National Ignition Facility,” to be published in *Inertial Fusion Sciences and Applications 1999*, Bordeaux, France, 12–17 September 1999.
2. S. V. Weber *et al.*, *ICF Quarterly Report* **7**, 43, Lawrence Livermore National Laboratory, Livermore, CA, UCRL-LR-105821-97-2 (1997).
3. S. E. Bodner, D. G. Colombant, J. H. Gardner, R. H. Lehmborg, S. P. Obenschain, L. Phillips, A. J. Schmitt, J. D. Sethian, R. L. McCrory, W. Seka, C. P. Verdon, J. P. Knauer, B. B. Afeyan, and H. T. Powell, *Phys. Plasmas* **5**, 1901 (1998).
4. E. B. Goldman *et al.*, *J. Appl. Phys.* **45**, 1158 (1974).
5. J. M. Soures, T. C. Bristow, H. Deckman, J. Delettrez, A. Entenberg, W. Friedman, J. Forsyth, Y. Gazit, G. Halpern, F. Kalk, S. Letzring, R. McCrory, D. Peiffer, J. Rizzo, W. Seka, S. Skupsky, E. Thorsos, B. Yaakobi, and T. Yamanaka, in *Laser Interaction and Related Plasma Phenomena*, edited by H. J. Schwarz (Plenum Press, New York, 1981), Vol. 5, pp. 463–481.
6. Yu. V. Afanas'ev and O. N. Krokhin, *Sov. Phys.-JETP* **25**, 639 (1967).
7. J. Bunkenburg, J. Boles, D. C. Brown, J. Eastman, J. Hoose, R. Hopkins, L. Iwan, S. D. Jacobs, J. H. Kelly, S. Kumpan, S. Letzring,

- D. Lonobile, L. D. Lund, G. Mourou, S. Reformat, W. Seka, J. M. Soures, and K. Walsh, *IEEE J. Quantum Electron.* **QE-17**, 1620 (1981).
8. G. Mourou, J. Bunkenburg, and W. Seka, *Opt. Commun.* **34**, 252 (1980).
9. J. E. Balmer, T. P. Donaldson, W. Seka, and J. A. Zimmermann, *Opt. Commun.* **24**, 109 (1978).
10. D. K. Bradley, T. Boehly, D. L. Brown, J. Delettrez, W. Seka, and D. Smith, in *Laser Interaction and Related Plasma Phenomena*, edited by H. Hora and G. Miley (Plenum Press, New York, 1991), Vol. 9, pp. 323–334.
11. R. C. Elton, H. R. Griem, and E. J. Iglesias, *Bull. Am. Phys. Soc.* **44**, 38 (1999).
12. T. R. Boehly, R. S. Craxton, T. H. Hinterman, P. A. Jaanimagi, R. L. Keck, J. H. Kelly, T. J. Kessler, R. L. Kremens, S. A. Kumpan, S. A. Letzring, R. L. McCrory, S. F. B. Morse, W. Seka, S. Skupsky, J. M. Soures, and C. P. Verdon, in *Proceedings of the IAEA Technical Committee Meeting on Drivers for Inertial Confinement Fusion*, edited by J. Coutant (IAEA, Vienna, 1995), pp. 79–86.
13. J. R. Murray, in *Third Annual International Conference on Solid State Lasers for Application to Inertial Confinement Fusion*, Supplement to *Proceedings of SPIE, Volume 3492* (SPIE, Bellingham, WA, 1998), pp. 1–10.
14. T. J. Kessler, Y. Lin, J. J. Armstrong, and B. Velazquez, in *Laser Coherence Control: Technology and Applications*, edited by H. T. Powell and T. J. Kessler (SPIE, Bellingham, WA, 1993), Vol. 1870, pp. 95–104.
15. H. A. Rose and D. F. DuBois, *Phys. Fluids B* **5**, 590 (1993).
16. Y. Fisher, T. R. Boehly, D. K. Bradley, D. R. Harding, D. D. Meyerhofer, and M. D. Wittman, *Bull. Am. Phys. Soc.* **43**, 1784 (1998).
17. Y.-H. Chuang, D. D. Meyerhofer, S. Augst, H. Chen, J. Peatross, and S. Uchida, *J. Opt. Soc. Am. B* **8**, 1226 (1991).

Design and Synthesis of Near-Infrared Absorbing Dyes for the Liquid Crystal Point-Diffraction Interferometer (LCPDI)

Introduction

Although considerable progress in achieving the goals of ICF has been made in recent years, considerable work still remains in improving direct-drive laser systems to the point where fuel ignition can occur. Because of difficulties in manufacturing large-aperture optical elements such as those used in OMEGA, these optics can add aberrations to each laser beam that can result in wavefront errors in the incident beams. Such wavefront errors can manifest themselves in unequal illumination of the target, which in turn reduces the uniformity of the energy being delivered by the laser. Although numerous diagnostic instruments are used on OMEGA to analyze beam-uniformity problems, a more effective method of measuring wavefront aberrations than is currently available is required. Shearing interferometry is currently used to analyze OMEGA beamlines, but the method suffers from (1) an inability to perform gradient measurements in more than two directions; (2) a low sensitivity to high-order phase errors; and (3) low spatial resolution. One approach taken to avoid these difficulties is to use a point-diffraction interferometric setup that relies on a liquid crystal (LC) electro-optical device as the primary modulation element. The fundamental design of this liquid crystal point-diffraction interferometer (LCPDI), as first introduced by Mercer and Creath,^{1,2} is similar to that of the general PDI design. In the LCPDI, however, an LC layer replaces the semitransparent filter of the conventional design, and the point used for diffraction (i.e., creation of the reference beam) is a microsphere embedded in the liquid crystal layer (Fig. 81.37). The incident beam is focused on the area of the cell that contains the microsphere, and optical interference occurs between the portions of the beam that pass through the glass microsphere and the liquid crystal fluid.

Phase shifting is accomplished by applying a voltage to the LC device, which undergoes a change in birefringence with applied voltage. A distinct advantage of the LCPDI is its common-path nature, i.e., both object and reference beams follow the same path as opposed to two different paths as in interferometers such as the Mach-Zehnder. This attribute makes the LCPDI less sensitive to environmental disturbances such

as mechanical vibration, temperature fluctuations, and air turbulence. It is also inherently phase shifting, allowing higher spatial sampling and generally more accurate wavefront characterization than other interferometric techniques. The single-path design also requires fewer optical elements than the Mach-Zehnder, thereby reducing size and cost of the instrument. Mercer, Rashidnia, and Creath³ have shown that for operation in the visible region the LCPDI is significantly more robust when compared with a phase-shifting Mach-Zehnder interferometer.³

Because the imaged area of the LCPDI device is substantially larger than the cross-sectional area of the microsphere, the portion of the beam that passes through the LC fluid must be attenuated to obtain sufficient contrast to analyze output images. In practice, this attenuation has been accomplished by adding a “guest” dye to the LC fluid “host” material used in the device. The LC host material is a commercial nematic LC

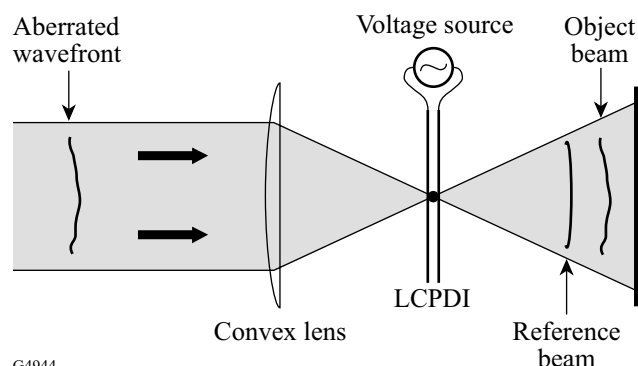


Figure 81.37 Schematic diagram of the liquid crystal point-diffraction interferometer (LCPDI). The laser beam is focused onto an area of the liquid crystal electro-optical device containing a glass or plastic sphere in the LC fluid gap. The portion of the beam passing through the microsphere functions as the reference arm of the interferometer. Application of an electric field to the birefringent LC material produces controlled molecular reorientation with subsequent generation of interference fringes. (Microsphere not drawn to scale.)

mixture of cyanobiphenyl and cyanoterphenyl components (Merck E7), which possesses a relatively high birefringence and positive dielectric anisotropy (Fig. 81.38).

For successful device operation, the guest dye must meet a number of important criteria:

- a strong absorbance maximum at or near the wavelength of incident laser radiation;
- high solubility in the liquid crystal host to maximize contrast and avoid long-term precipitation;
- excellent chemical and thermal stability; and
- low impact on the long-range molecular ordering in the LC host.

Two additional properties that would be highly desirable in dyes intended for LCPDI devices are (1) a low or nonexistent dichroism of the absorption band of interest so as to assure a constant attenuation with applied electric field, and (2) a liquid crystalline phase to allow larger amounts of the dye to be added without degrading the inherent molecular ordering of the host.

Although hundreds of dyes for visible-region LCPDI devices are commercially available, the selection of available dyes for the near IR is considerably more limited, and only a small subset of these absorb at the required 1054-nm wave-

length for operation in OMEGA. A further complication is that nearly all of these commercially available near-IR dyes are ionic or highly polar and, as such, show poor solubility in hydrocarbon-like liquid crystal hosts (0.01 to 0.05 wt%). One such example of this type of dye is shown in Fig. 81.39. The low solubility of these dyes essentially limits them to a maximum blocking extinction, or optical density (OD), in the LC host of <0.1, which is two decades less than required for producing acceptable fringe contrast for diagnostic purposes. The lack of a suitable near-IR dye candidate with sufficient LC host solubility dictated that a new dye or series of dyes be synthesized for the LCPDI device to meet its design goals.

Dye Selection and Design

The dye systems that were chosen for study are based on zerovalent transition metal dithiolene complexes,^{4,5} which are known to exhibit strong absorbance bands in the 600- to 1500-nm region of the spectrum and to be soluble in nonpolar organic solvents, depending on the dye's molecular structure. Our investigations focused on compounds using nickel as the central transition element (Fig. 81.40). Nickel dithiolenes are of special interest for this application because of their high solubility (up to 10 wt%) in liquid crystalline hosts⁶ and because the dyes themselves can possess liquid crystalline properties if appropriate terminal functional groups are selected.^{6,7} The latter is a distinct advantage because it would allow higher concentrations of the dye to be added to the liquid crystalline host without substantially reducing its degree of order.

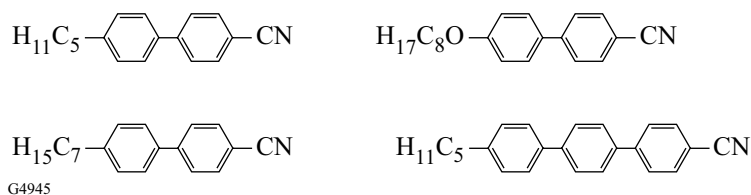


Figure 81.38

Composition of Merck E7, a high-birefringence nematic LC mixture with positive dielectric anisotropy used as the active host medium for the LCPDI device.

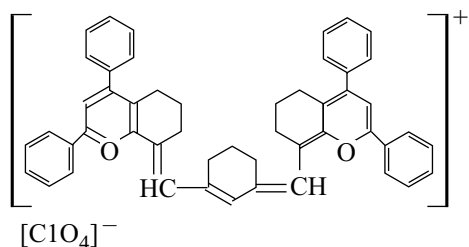


Figure 81.39

Molecular structure of a commercially available laser dye *Q*-switch 5 (Exciton, Inc). Because of their ionic and highly polar nature, nearly all laser dyes exhibit poor solubility in hydrocarbon-like liquid crystal host materials such as E7.

The strong near-infrared absorbance maxima observed in the nickel dithiolenes is a function of both extensive electron delocalization within the dithiolenene ring system and interaction of this delocalized system with available d-orbitals on the

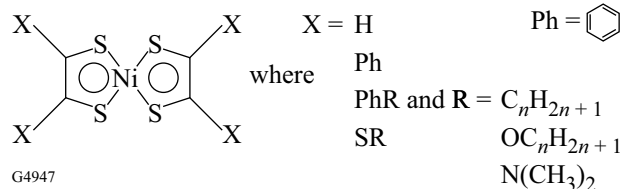


Figure 81.40

The molecular structure of transition metal dithiolenes with nickel as the central metal. The physical properties of the complex are determined by the nature of the terminal functional groups, designated as X, in the figure.

central metal.⁸ This interaction can be depicted both graphically and mathematically by using the linear combination of the atomic orbital–molecular orbital (LCAO–MO) theory. Here the atomic orbitals of the individual atoms are combined to form a series of lower-energy “bonding” and higher-energy “anti-bonding” molecular orbitals. Absorption of photons of sufficient energy results in promotion of electrons from occupied (bonding) molecular orbitals to unoccupied (anti-bonding) molecular orbitals. The lowest-energy transition, and thus the one that occurs at the longest wavelength, occurs between the highest occupied molecular orbital (HOMO) and the lowest unoccupied molecular orbital (LUMO) and is referred to as the bandgap. This HOMO/LUMO transition is responsible for the strong near-IR absorption in the nickel dithiolenes.^{4,8} Figures 81.41 and 81.42 show ground-state electronic-charge-distribution maps and HOMO/LUMO electron-density-

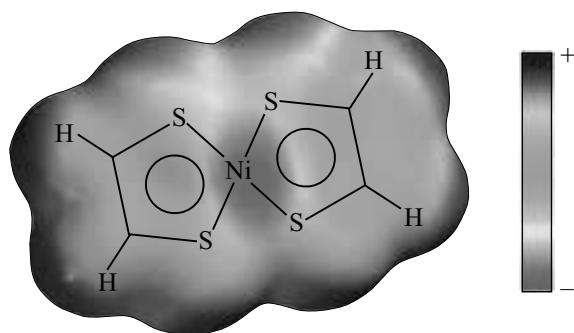


Figure 81.41

Ground-state electronic-charge-distribution map of the nickel dithiolenene core. The shaded areas indicate electron-rich areas in the molecule.

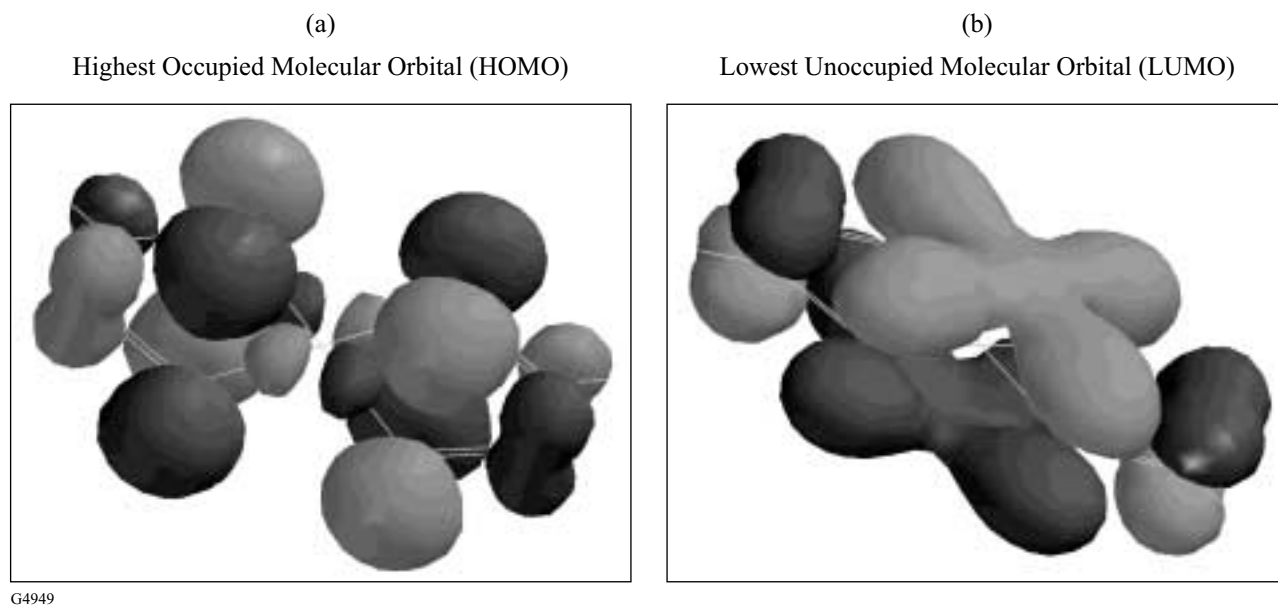


Figure 81.42

Electron-density probability maps of HOMO (left) and the LUMO (right) for the nickel dithiolenene core.

probability maps, respectively, over the nickel dithiolenene core as generated by Spartan 5.0 computational chemistry software (Wavefunction, Inc.). The energy levels in electron volts for each molecular orbital can also be represented graphically, as shown in Fig. 81.43 for the nickel dithiolenene core of Fig. 81.41. The nature of the functional groups attached to the nickel dithiolenene core has a large effect on both the position of the electronic absorbance maximum and the solubility of the dye in the host matrix. Figure 81.44 compares the spectroscopic and solubility properties of two *para*-substituted nickel dithiolenenes that have been previously studied in liquid crystal host systems.⁶

Because the above two compounds represented nearly the sum total of literature data on the behavior of near-IR dyes in LC hosts, we chose to use these materials as the basis of our design and synthesis efforts. Our goal was to test different combinations of functional groups on the nickel dithiolenene core, both empirically and computationally, to observe their effect on both solubility and optical absorbance. To this end, we initiated the synthesis of a series of materials based on compound (a) in Fig. 81.44 with terminal alkyl and alkoxy groups

for initial studies of solubility and spectroscopic properties in the E7 LC host. In a parallel effort, we attempted to use computational chemistry methods to aid in predicting the appropriate functional group combinations that would yield materials with the desired solubility and spectroscopic parameters. These calculations were performed using the computational chemistry software packages Spartan 5.0 for molecular geometry optimization and Jaguar 3.5 (Schrödinger, Inc.) for solubility calculations.

Structural energy minimization calculations using semiempirical methods were undertaken using Spartan 5.0 prior to conducting the solubility calculations to ensure that the structural geometry of the compounds under evaluation was in its lowest-energy conformation. We chose the semiempirical approach because it can accurately predict equilibrium geometry using much less computing resources than *ab initio* and density functional methods and, when proper parameters for transition metals are applied, can also take into account contributions from bonding to d-orbitals. All calculations were conducted using a DEC AlphaServer running the Digital UNIX operating system.

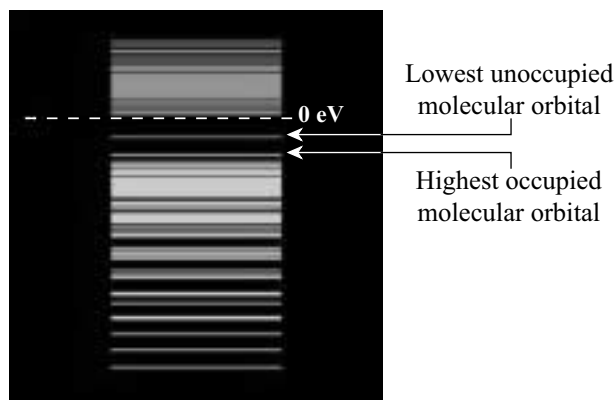
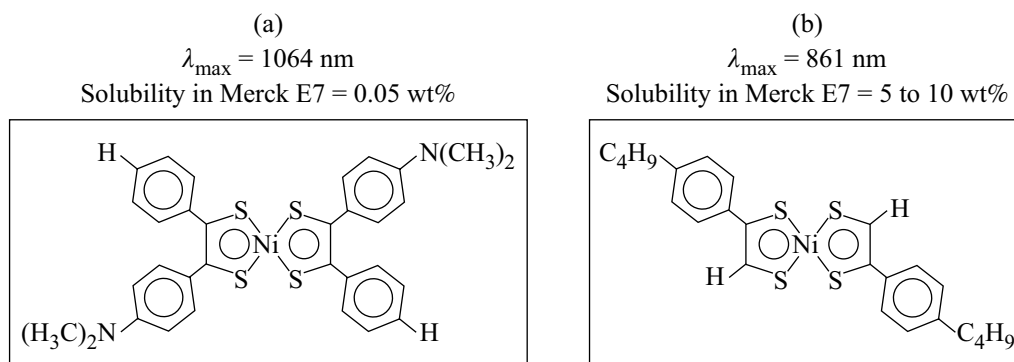


Figure 81.43

Energy levels for bonding (HOMO) and antibonding (LUMO) molecular orbitals in the nickel dithiolenene core shown in Fig. 81.41. The energy difference between the HOMO and LUMO is termed the bandgap and determines the portion of the spectrum (UV, visible, or near IR) where the electronic absorbance bands are observed.

G4950



G4951

Figure 81.44

Effect of molecular structure on solubility and spectroscopic properties of two substituted nickel dithiolenenes.

The solubility of a given solute in a solvent can be approximated by calculating its solvation energy and comparing this value with the bonding, or “reorganization,” energy. The solvation energy ΔG_{solv} is defined in Eq. (1) as⁹

$$\begin{aligned} \Delta G_{\text{solv}} = & \Delta G_{\text{elec}} + \Delta G_{\text{cav}} + \Delta G_{\text{disp}} \\ & + \Delta G_{\text{vib}} + \Delta G_{\text{lib}} + \Delta G_{\text{other}}, \end{aligned} \quad (1)$$

where ΔG_{solv} = solvation energy, ΔG_{elec} = electrostatic solute–solvent interaction, ΔG_{cav} = energy to form a solute shaped cavity, ΔG_{disp} = London and van der Waals interactions, ΔG_{vib} = change in vibrational energy due to damping, ΔG_{lib} = conversion of rotations and translations to librations, and ΔG_{other} = solvent enthalpic and entropic structure (PV term, etc.).

Although Spartan 5.0 has the ability to conduct geometry optimization in solution, it is not capable of dealing with d-orbitals in the solvation calculations. Because the metal d-orbitals play an extremely important role in determining the properties of the nickel dithiolenes, they must be taken into account in these calculations in order to obtain valid results. For these solubility calculations we instead opted to use Jaguar 3.5, a UNIX-based modeling package that does have this capability. Using the dielectric constant, molecular weight, and density of the solvent, Jaguar determines a “probe radius” parameter that is used to calculate the solvation energy.¹⁰

Solvated molecular systems are treated by Jaguar by means of a self-consistent reaction field method using its own Poisson–Boltzmann solver. The Poisson–Boltzmann equation [Eq. (2)]¹¹ sets the sum of the internal and external potentials equal to zero, allowing the program to solve for the elements of the solvation energy according to the three-dimensional grid mapped out by the equation using the finite difference method:

$$\nabla \cdot \epsilon(r) \nabla \phi(r) - \epsilon \kappa^2 \sinh[\phi(r)] + 4\pi q \rho^f(r) / kTf(\phi) = 0, \quad (2)$$

where ϵ = dielectric constant, q = proton charge, k = Boltzmann’s constant, T = absolute temperature, ρ^f = fixed charge density, $\phi(r)$ = dimensionless electrostatic potential in units of kT/q , r = position vector, and $\kappa^2 = 1/\lambda^2 = 8\pi q^2 I / \epsilon kT$, where λ = Debye length, and I = ionic strength of the bulk solution.

Because currently available software is incapable of conducting these calculations in solvent systems that are either (1) anisotropic in their physical properties or (2) mixtures of compounds, a direct calculation of dye solubility in the E7 nematic host mixture was not feasible. Our approach was instead to use single-component, *isotropic* solvents with molecular structures similar to that of the components in the E7 host so as to establish qualitative solubility trends with changes in terminal functional groups. Cyclohexane (a common organic solvent) and Merck CB-15 (an isotropic chiral cyanobiphenyl compound structurally similar to the components of E7) were chosen as the solvent host media for the calculations (Fig. 81.45). One difficulty encountered early in the solubility calculations was that the probe radius calculation assumes that the solvent host molecules are rigid and spherical. Although cyclohexane nicely fits this description (Fig. 81.45), CB-15 is a relatively long, cigar-shaped molecule and as such has a substantially larger probe radius value (3.647 Å, as calculated by Jaguar). Unfortunately, current limitations in the Jaguar software package restrict the maximum probe radius for the solvent host to a value of <3.1 Å, and we found it necessary to artificially limit the probe radius value for CB-15 to 2.8 Å in order for the calculations to proceed. The required reduction in probe radius has a minimal impact on the calculation, as the dielectric constant is the parameter that has the greatest influence on the calculated result. Table 81.V shows the calculated solvation energies obtained for compounds containing the nickel dithiolenes with a selected group of terminal functional groups as solutes in cyclohexane and CB-15. The value ΔG_{solv} can be used as a qualitative indicator of general solubility of the dye solutes in the same host, with a larger positive value generally indicating a greater solubility in the solvent host matrix. As shown in Table 81.V, the calculated ΔG_{solv} values imply that sulfur-containing substituents are expected to provide a substantial enhancement in solubility, with the greatest enhancement expected for alkylthio (-SR) terminal groups bonded directly to the nickel dithiolenes core.

Dye Synthesis

The synthesis of the nickel dithiolenes dyes and their precursors were conducted using literature methods^{12–15} with some modifications. The structural identity of synthesized products was verified using UV-visible–near-IR spectrophotometry, Fourier transform infrared (FTIR) spectrometry, and nuclear magnetic resonance (NMR) spectrometry. Product purity was assessed by high-performance liquid chromatography (HPLC) and, for crystalline products, by melting point via hot-stage polarizing microscopy. Phase transitions were

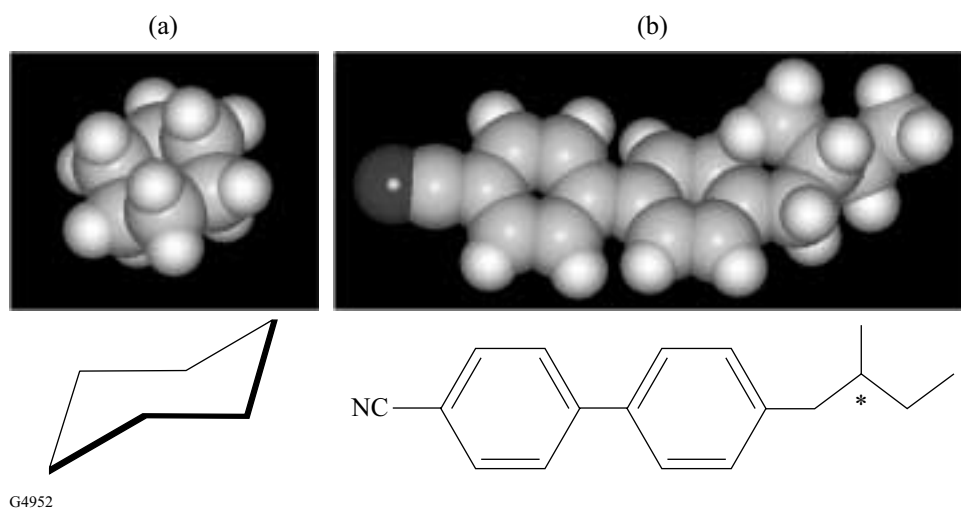


Figure 81.45

The solvent hosts used for the solubility calculations: (a) cyclohexane and (b) Merck CB-15. A space-filling graphical model of each solvent host is shown at the top of the figure, with the chemical structure drawn below. Note that the hydrogen atoms have been omitted in the structural formulas for clarity. The asterisk in the CB-15 structure indicates the presence of an asymmetric (chiral) carbon.

characterized by both differential scanning calorimetry (DSC) and hot-stage polarizing microscopy.

For materials with terminal substituents containing phenyl groups (-PhR and -PhOR), we used the method of Ohta *et al.*,¹² as shown in Fig. 81.46. Compounds with terminal alkylthio substituents (-SR) were synthesized based on methods reported by Wainwright and Underhill,¹³ N. Svenstrup *et al.*,¹⁴ and A. Charlton *et al.*,¹⁵ which are shown in Fig. 81.47. Our modifications to the original published procedures afforded

Table 81.V: Results of solvation energy calculations on nickel dithiolene cores with various terminal functional groups in cyclohexane and CB-15 using Jaguar. A larger positive value indicates a greater solubility in the host matrix.

	ΔG_{solv} Cyclohexane (kcal/mole)	ΔG_{solv} Merck CB-15 (kcal/mole)
X = SC ₈ H ₁₇	6.9435	-7.6725
X = SC ₇ H ₁₅	6.2764	-7.7164
X = SC ₄ H ₉	3.9248	-7.7190
X = PhC ₄ H ₉	3.2985	-14.4373
X = PhN(CH ₃) ₂	0.0812	-17.4080
X = PhOC ₉ H ₁₉	5.2212	-21.6724
X = PhOC ₄ H ₉	0.9780	-21.6950

substantial improvements in yields of pure product in most cases. Table 81.VI gives the physical properties and yields of dyes synthesized by these two methods.

Solubility Studies

Prior to generation of a suitable mixture for use in the LCPDI device, the solubility limits of selected nickel dithiolene dyes in three host systems (cyclohexane, Merck CB-15, and Merck E7) were determined by means of a time-based sedimentation experiment. Samples of each dye chosen for study were prepared in the three host materials at select concentrations between 0.3 wt% to 1 wt%. Each dye was dissolved into 2 ml of each host by heating the host/dye mixture to an elevated temperature (40°C for cyclohexane and 100°C for CB-15 and E7) and stirring for several hours. Upon cooling, each sample was filtered through a 0.45- μm Teflon membrane filter to remove any insoluble material. All samples were checked periodically, both visually and by microscopic inspection at 100 \times magnification, for evidence of dye precipitation. For samples that showed precipitation at 0.3%, new mixtures at lower concentrations were prepared until a stable dye concentration was achieved. The results are shown in Table 81.VII, along with the ΔG_{solv} values previously calculated from Table 81.VI. Because such a large number of mixtures were required in the sedimentation experiment and only limited quantities of each dye were available, we were unable to determine an absolute upper solubility limit for each dye mixture combination. Experiments are currently underway to

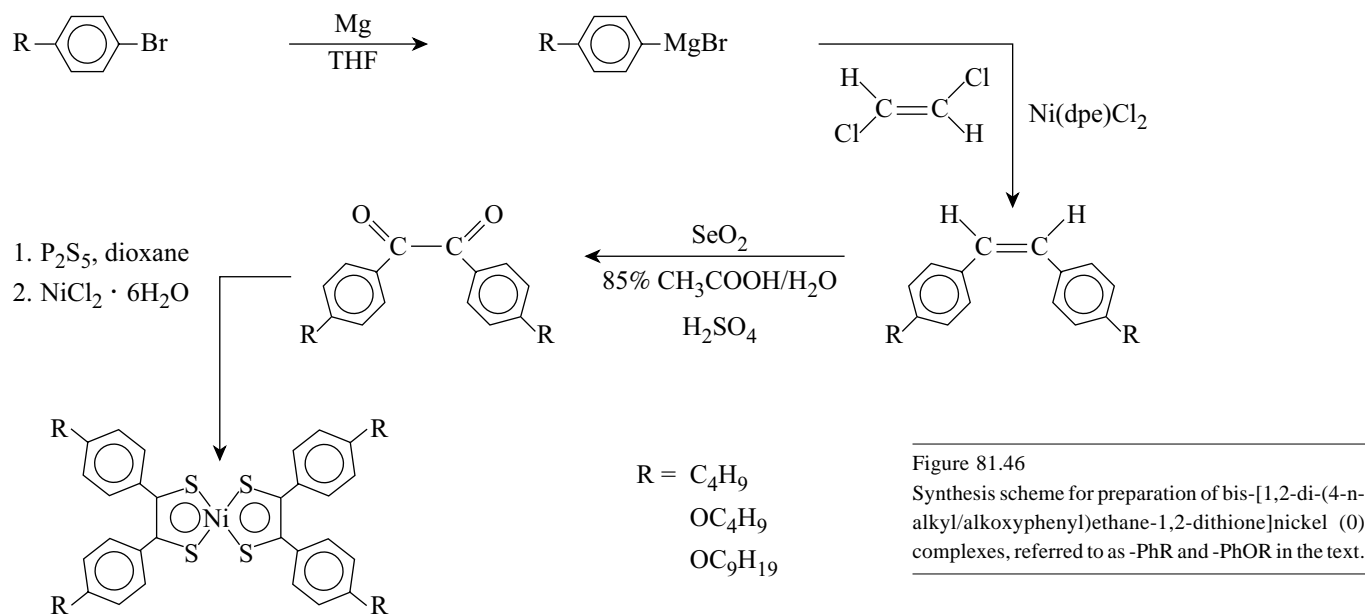


Figure 81.46
 Synthesis scheme for preparation of bis-[1,2-di-(4-n-alkyl/alkoxyphenyl)ethane-1,2-dithione]nickel (0) complexes, referred to as -PhR and -PhOR in the text.

G4953

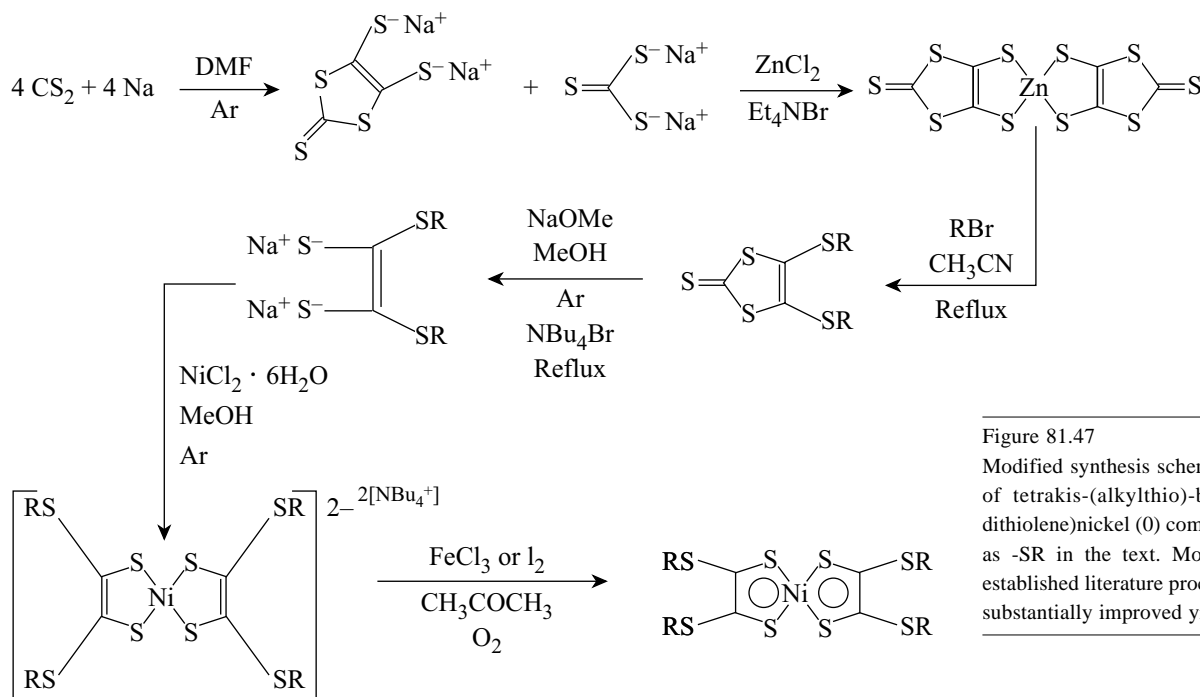


Figure 81.47
 Modified synthesis scheme for preparation of tetrakis-(alkylthio)-bis-(ethylene-1,2-dithiolene)nickel (0) complexes, referred to as -SR in the text. Modifications to the established literature procedures resulted in substantially improved yields of product.

G4954

more accurately determine the absolute solubility limit using only one supersaturated mixture for each dye/host pair by employing near-IR spectroscopic techniques.

A review of Tables 81.VI and 81.VII shows that there are substantial differences not only in the solubility of each dye in the different hosts but also in the position of its λ_{\max} as the host matrix is changed. In general, a 20- to 47-nm bathochromic

(red) shift is observed for these dyes in the anisotropic, ordered LC host as compared to an isotropic host such as acetone or cyclohexane.⁶ With regard to solubility, the experimental solubility data for the nickel dithiolenes in cyclohexane and CB-15 shows a substantial improvement in solubility when terminal -PhOR substituents are replaced with -SR groups, as was predicted by the computational modeling. This trend is also observed, but to a somewhat lesser degree, in the anisotropic

Table 81.VI: Properties of the substituted nickel dithiolenes synthesized for study as dye “guest” dopants for the LCPDI.

Terminal Group	Yield (%)		Melting point (°C)	λ_{\max} , acetone (nm)	Purity %
	Observed	Literature			
-PhC ₄ H ₉	51	N.R.	228.3–230.6	870	99.4
-PhOC ₄ H ₉	60	59	246.3–248.7	910	94.0
-PhOC ₉ H ₁₉	53	57	184.3–189.1	912	90.0
-SC ₄ H ₉	68	15	101	1002	99.3
-SC ₅ H ₁₁	64	15	95–98	1002	98.8
-SC ₆ H ₁₃	27	20	68.5–71.1	1002	98.1
-SC ₇ H ₁₅	41	27	81.5	1002	99.2
-SC ₈ H ₁₇	56	31	73	1002	99.3
-SC ₉ H ₁₉	29	30	80.4–81.2	1002	98.9
-SC ₁₀ H ₂₁	11	25	69.4–70.3	1002	96.5

N.R. = not reported

Table 81.VII: Comparison of calculated solvation energies and experimentally determined solubility limits of nickel dithiolenes in three host systems. For some dye mixture combinations, an absolute upper solubility limit has not been determined due to limited dye quantities.

Terminal (X) group	λ_{\max} in E7 (nm)	Cyclohexane		CB-15		Merck E7
		Solubility limit (wt%)	ΔG_{solv} (kcal/mole)	Solubility limit (wt%)	ΔG_{solv} (kcal/mole)	Solubility limit (wt%)
-SC ₈ H ₁₇	1020	≥0.5%	6.9435	≥1.0%	-7.6725	≤0.5%
-SC ₇ H ₁₅	1020	≥0.5%	6.2764	≤1.0%	-7.7164	≤0.5%
-SC ₄ H ₉	1020	≤0.5%	3.9248	≤1.0%	-7.7190	≤0.5%
-PhC ₄ H ₉	910	≤0.05%	3.2985	≤0.5%	-14.4373	≥0.3%
-PhN(CH ₃) ₂	1056	<0.5%	0.0812	≤0.5%	-17.4080	<0.1%
-PhOC ₉ H ₁₉	970	≤0.025%	5.2212	≤0.3%	-21.6724	<0.3%
-PhOC ₄ H ₉	970	<0.001%	0.9780	≤0.3%	-21.6950	≤0.3%

< = substantial precipitation at indicated value

≤ = marginal precipitation at indicated value

≥ = no precipitation at indicated value; actual upper solubility limit not determined

E7 LC host mixture intended for use in the LCPDI. The -SR materials will provide a larger blocking extinction at the same solution concentration than will their -PhOR counterparts since the λ_{max} of the -SR compounds in E7 is 70 to 110 nm closer to the 1054-nm operational wavelength of OMEGA than is the λ_{max} of the -PhOR substituted materials. The commercial dye with -PhN(CH₃)₂ substituents, although its λ_{max} is closest to 1054 nm and is nearly as soluble as the other dyes in cyclohexane and CB-15, displays the lowest solubility of the group in the E7 host.

Because no single dye has sufficient solubility in the E7 host to achieve the required OD of 1.8 to 2, it became necessary to use a mixture of several dyes to increase the total dye concentration past the general solubility limit of 0.3%–0.5% for each dye component.

LCPDI Guest–Host Mixtures

Multicomponent mixtures of various dyes from Table 81.VII were formulated and evaluated for their performance characteristics with regard to optical absorbance capability and stability in the E7 host LC fluid. Table 81.VIII gives the composition of these mixtures. The dye mixtures were prepared in the same manner as described earlier in the solubility experiments. LCPDI test cells were assembled from glass substrates bearing a 500-Å, transparent, conductive indium tin oxide (ITO) coating. The ITO surfaces were spin coated with a polyimide alignment coating, which, after baking and buffing, served as an alignment layer for the guest–host LC mixture. Glass spheres (25- μm diam) were deposited onto the coated, buffed surface of one substrate, and a second coated, buffed substrate was placed on top of the spheres with its rub direction anti-parallel

to the bottom substrate to define a 25- μm gap. The substrates were bonded together using Master Bond UV15-7TK1A UV curable epoxy, and the cells were filled with the LCPDI guest–host mixture by capillary action. Absorbance spectra of the devices were determined using a Perkin-Elmer Lambda 9 UV-VIS-NIR spectrophotometer with the incident beam polarized parallel to the cell alignment axis. Figure 81.48 compares the optical properties of the three mixtures. As is evident from Fig. 81.48, the mixture containing six -SR substituted dyes and one commercial -PhN(CH₃)₂ dye achieves the desired OD requirements for the LCPDI.

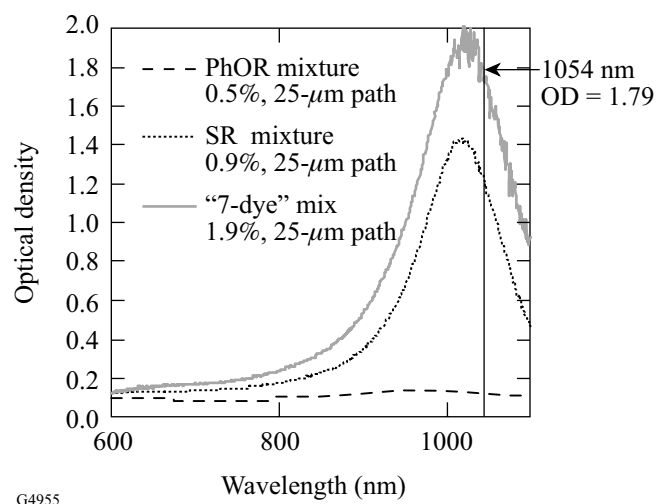


Figure 81.48 Optical-density data on three guest-host dye mixtures for the LCPDI. The measurements were made with the cell alignment axis parallel to the polarized incident beam of the spectrophotometer.

Table 81.VIII: Composition of three dye mixtures formulated for optical density (OD) evaluation in LCPDI test cells.

-PhOR mix		-SR mix		"7-dye" mix	
-PhOC ₄ H ₉	0.25%	-SC ₄ H ₉	0.3%	-SC ₄ H ₉	0.3%
-PhOC ₉ H ₁₉	0.25%	-SC ₇ H ₁₅	0.3%	-SC ₅ H ₁₁	0.3%
Total	0.5%	-SC ₈ H ₁₇	0.3%	-SC ₇ H ₁₅	0.3%
		Total	0.9%	-SC ₈ H ₁₇	0.3%
				-SC ₉ H ₁₉	0.3%
				-SC ₁₀ H ₂₁	0.3%
				-PhN(CH ₃) ₂	0.1%
				Total	1.9%

To date, there has been no evidence of crystallization or phase separation of dye components in this mixture after storage periods of several months, either in the bulk mixtures or in fabricated devices. In most-recent developments, a dye mixture containing a new nickel dithiolene compound that is a *liquid* at room temperature as an eighth dye component is being evaluated in an LCPDI device for its performance in the near IR. Devices containing this new mixture have displayed OD values of 2.77 and 1.85 for a 25- μm and 15- μm path length, respectively. The substantial improvement in OD afforded by this new compound now opens the possibility of fabricating thinner LCPDI devices that will exhibit improved contrast, reduced scattering losses, and faster electro-optic temporal response over previous-generation, near-IR devices.

Summary

The LCPDI device has exceptional potential for use in OMEGA due to a number of important attributes. Its inherently phase-shifting nature allows higher spatial sampling and generally more-accurate wavefront characterization than other interferometric techniques, while the single-path design requires fewer optical elements than other types of interferometers, thereby reducing size and cost requirements. The compact and “solid-state” nature of the device provides additional benefits in the form of reduced sensitivity to environmental disturbances such as mechanical vibration, temperature fluctuations, and air turbulence. The largest single obstacle to deployment of the LCPDI in OMEGA has been the availability of a near-IR dye with sufficient LC host solubility; chemical, thermal, and optical stability; and electronic absorbance properties to produce devices capable of sufficient contrast for output image analysis. Here, we have shown that, through selection of appropriate functional groups, zerovalent transition metal dithiolenes can be designed and synthesized that will allow the LCPDI to realize its design goals for deployment in OMEGA.

Although present computational chemistry methods and software are somewhat limited in scope for organometallic compounds, they can still provide useful qualitative guidance in the design and development of new dye compounds with solubility and optical absorbance requirements tailored to a specific host material. Using this approach, we demonstrated

both theoretically and experimentally that sulfur-containing alkyl terminal groups are superior to alkoxy, alkylphenyl, and alkoxyphenyl substituents both in enhancing the solubility of the nickel dithiolene core in the host medium and in optimizing the location of the dye λ_{max} for maximum absorbance efficiency. Employing a mixture of dyes rather than just a single-dye substance was shown to have two benefits: (1) a larger overall host dye concentration allows construction of thinner LCPDI devices with better performance characteristics, and (2) thermodynamic stability of the guest–host mixture is substantially enhanced since the relatively low concentration of each dye component reduces the risk of long-term dye precipitation from the host.

In addition to the pending evaluation of the capabilities of current near-IR LCPDI devices, experiments are also underway to more accurately determine the solubility limit of the dyes by spectroscopic techniques and to further refine the dye mixture composition so as to achieve additional gains in OD without sacrificing mixture stability. Our recent modeling efforts have generated a library of over 40 new transition metal dithiolene compounds that await further synthesis efforts to evaluate their potential as dye candidates for the LCPDI as well as for other near-IR LC device applications in optical communications and sensor protection.

ACKNOWLEDGMENT

The authors gratefully acknowledge the contributions of the following individuals and organizations: Dr. Julie R. Wright (Schroedinger, Inc.); Dr. W. Thomas Pollard (Schroedinger, Inc.); Dr. Wayne Huang (Wavefunction, Inc.); and Dr. Ansgar W. Schmid (LLE) for guidance and helpful discussions regarding computational chemistry methods and applications; Prof. Ulrich Muller-Westerhoff (Department of Chemistry, University of Connecticut) and Prof. Alan E. Underhill (Department of Chemistry, University of Wales) for helpful discussions on transition metal dithiolene syntheses; Irene Lippa (LLE) for determination of dye solubilities in host systems; Malia Moore, Awista Ayub, Scott Kinsella, and Kendra Bussey (LLE) for assistance in synthesis of metal complexes and precursors; and Tanya Kosci, Nathan Bickel, Ryan Brecker, and Markar Naradikian (LLE) for construction and characterization of the LCPDI devices. This work was supported by the U.S. Department of Energy Office of Inertial Confinement Fusion under Cooperative Agreement No. DE-FC03-92SF19460, the University of Rochester, and the New York State Energy Research and Development Authority. The support of DOE does not constitute an endorsement by DOE of the views expressed in this article.

REFERENCES

1. C. R. Mercer and K. Creath, *Opt. Lett.* **19**, 916 (1994).
2. C. R. Mercer and K. Creath, *Appl. Opt.* **35**, 1633 (1996).
3. C. R. Mercer, N. Rashidnia, and K. Creath, *Exp. Fluids* **21**, 11 (1996).
4. U. T. Mueller-Westerhoff, B. Vance, and D. I. Yoon, *Tetrahedron* **47**, 909 (1991).
5. P. Espinet *et al.*, *Coord. Chem. Rev.* **117**, 215 (1992).
6. K. L. Marshall and S. D. Jacobs, *Mol. Cryst. Liq. Cryst.* **159**, 181 (1988).
7. U. T. Mueller-Westerhoff *et al.*, *Mol. Cryst. Liq. Cryst. Lett.* **56**, 249 (1980).
8. U. T. Mueller-Westerhoff and B. Vance, in *Comprehensive Coordination Chemistry: The Synthesis, Reactions, Properties, and Applications of Coordination Compounds*, 1st ed. (Pergamon Press, Oxford, England, 1987), Vol. 2, pp. 595–631.
9. M. Colvin, "Continuum Models of Solvation," Lawrence Livermore National Laboratory (2000), available on the Internet at <http://gutenberg.llnl.gov/~colvin/solvation/solv.html>.
10. B. Lee and F. M. Richards, *J. Mol. Biol.* **55**, 379 (1971).
11. B. Honig, K. Sharp, and A. S. Yang, *J. Phys. Chem.* **97**, 1101 (1993).
12. K. Ohta *et al.*, *Mol. Cryst. Liq. Cryst.* **147**, 15 (1987).
13. C. E. A. Wainwright and A. E. Underhill, *Mol. Cryst. Liq. Cryst.* **234**, 193 (1993).
14. N. Svenstrup *et al.*, *Synthesis* **8**, 809 (1994).
15. A. Charlton *et al.*, *J. Mater. Chem.* **4**, 1861 (1994).

Publications and Conference Presentations

Publications

S. R. Arrasmith, I. A. Kozhinova, L. L. Gregg, H. J. Romanofsky, A. B. Shorey, S. D. Jacobs, D. Golini, W. I. Kordonski, P. Dumas, and S. Hogan, "Details of the Polishing Spot in Magnetorheological Finishing (MRF)," in *Optical Manufacturing and Testing III*, edited by H. Stahl (SPIE, Bellingham, WA, 1999), Vol. 3782, pp. 92–100.

J. L. Chaloupka and D. D. Meyerhofer, "Observation of Electron Trapping in an Intense Laser Beam," *Phys. Rev. Lett.* **83**, 4538 (1999).

S.-H. Chen, J. C. Mastrangelo, and R. J. Jin, "Glassy Liquid-Crystal Films as Broadband Polarizers and Reflectors via Spatially Modulated Photorecimization," *Adv. Mater.* **11**, 1183 (1999).

F. Dahmani, J. C. Lambropoulos, A. W. Schmid, S. Papernov, and S. J. Burns, "Crack Arrest and Stress Dependence of Laser-Induced Surface Damage in Fused-Silica and Borosilicate Glass," *Appl. Opt.* **38**, 6892 (1999).

S. D. Jacobs, S. A. Arrasmith, I. A. Kozhinova, L. L. Gregg, A. B. Shorey, H. J. Romanofsky, D. Golini, W. I. Kordonski, P. Dumas, and S. Hogan, "Magnetorheological Finishing (MRF): Computer-Controlled Optics Manufacturing," *The American Ceramic Society Bulletin*, December 1999, pp. 42–48.

D. Katsis, P. H. M. Chen, J. C. Mastrangelo, S.-H. Chen, and T. N. Blanton, "Vitrified Chiral-Nematic Liquid Crystalline Films for Selective Reflection and Circular Polarization," *Chem. Mater.* **11**, 1590 (1999).

R. S. Knox, "Physical Aspects of the Greenhouse Effect and Global Warming," *Am. J. Phys.* **67**, 1227 (1999).

C. J. McKinstrie and E. A. Startsev, "Forward and Backward Stimulated Brillouin Scattering of Crossed Laser Beams," *Phys. Rev. E* **60**, 5978 (1999).

A. B. Shorey, L. L. Gregg, H. J. Romanofsky, S. R. Arrasmith, I. Kozhinova, J. Jubregsen, and S. D. Jacobs, "Study of Material Removal During Magnetorheological Finishing (MRF)," in *Optical Manufacturing and Testing III*, edited by H. Stahl (SPIE, Bellingham, WA, 1999), Vol. 3782, pp. 101–111.

A. B. Shorey, W. I. Kordonski, S. R. Gorodkin, S. D. Jacobs, R. F. Gans, K. M. Kwong, and C. H. Farny, "Design and Testing of a New Magnetorheometer," *Rev. Sci. Instrum.* **70**, 4200 (1999).

Forthcoming Publications

R. Adam, M. Currie, C. Williams, R. Sobolewski, O. Harnack, and M. Darula, "Direct Observation of Subpicosecond Single-Flux-Quantum in Pulse-Driven Y-Ba-Cu-O Josephson Junctions," to be published in *Applied Physics Letters*.

S. R. Arrasmith, S. D. Jacobs, I. A. Kozhinova, A. B. Shorey, D. Golini, W. I. Kordonski, S. Hogan, and P. Dumas, "Devel-

opment and Characterization of Magnetorheological Fluids for Optical Finishing," to be published in the *Proceedings of Fine Powder Processing '99*, University Park, PA, 20–22 September 1999.

R. Betti, "Radial Discontinuities in Tokamak MHD Equilibria with Poloidal Flow," to be published in *Physics of Plasmas*.

R. Betti and J. P. Freidberg, "Low- β , Magnetohydrodynamic Tokamak Equilibria with Poloidal Transonic Flow," to be published in *Physical Review Letters*.

T. R. Boehly, A. Babushkin, D. K. Bradley, R. S. Craxton, J. A. Delettrez, R. Epstein, T. J. Kessler, J. P. Knauer, R. L. McCrory, P. W. McKenty, D. D. Meyerhofer, S. P. Regan, W. Seka, S. Skupsky, V. A. Smalyuk, R. P. J. Town, and B. Yaakobi, "Laser-Uniformity and Hydrodynamic-Stability Experiments at the OMEGA Laser Facility," to be published in *Laser and Particle Beams*.

D. P. Butler, Z. Celik-Butler, and R. Sobolewski, "Y-Ba-Cu-O as an Infrared Radiation Sensing Material," to be published in the *Handbook of Advanced Electronic and Photonic Materials* (Academic Press, NY).

J. L. Chaloupka and D. D. Meyerhofer, "Characterization of a Tunable Single-Beam Ponderomotive-Optical Trap," to be published in the *Journal of the Optical Society of America B*.

S.-H. Chen, R. J. Jin, D. Katsis, J. C. Mastrangelo, S. Papernov, and A. W. Schmid, "Selective Reflection and Polarization Band of Glassy Chiral-Nematic Films Broadened by Photoracemization," to be published in *Liquid Crystals*.

T. J. B. Collins, H. L. Helfer, and H. M. VanHorn, "Oscillations of Accretion Disks and Boundary Layers in Cataclysmic Variables: I. Unperturbed, Steady-Flow Models," to be published in *Astrophysical Journal*.

T. J. B. Collins, H. L. Helfer, and H. M. VanHorn, "Oscillations of Accretion Disks and Boundary Layers in Cataclysmic Variables: II. A Local, Linear Stability Analysis of Accretion Disk Boundary Layers," to be published in *Astrophysical Journal*.

M. Currie, C.-C. Wang, R. Sobolewski, and T. Y. Hsiang, "Picosecond Nodal Testing of Centimeter-Size Superconducting Nb Microstrip Interconnects," to be published in *Applied Superconductivity*.

F. Dahmani, A. W. Schmid, J. C. Lambropoulos, and S. J. Burns, "Lifetime Prediction of Laser-Pre-cracked Fused Silica Subjected to Subsequent Cyclic Laser Pulses," to be published in the *Journal of Materials Science*.

F.-Y. Fan, J. C. Mastrangelo, D. Katsis, and S.-H. Chen, "Novel Glass-Forming Liquid Crystals V. Nematic and Chiral-Nematic Systems with an Elevated Glass Transition Temperature," to be published in *Liquid Crystals*.

R. E. Giaccone, C. J. McKinstrie, and T. Kolber, "Angular Dependence of Stimulated Brillouin Scattering in a Homogeneous Two-Dimensional Plasma," to be published in *Physics of Plasmas*.

V. N. Goncharov, S. Skupsky, P. W. McKenty, J. A. Delettrez, R. P. J. Town, and C. Cherfils-Clérouin, "Stability Analysis of Directly Driven OMEGA and NIF Capsules," to be published in the *Proceedings of the 1999 Inertial Fusion Sciences and Applications Conference*, Bordeaux, France, 12–17 September 1999.

V. N. Goncharov, S. Skupsky, P. W. McKenty, R. P. J. Town, T. R. Boehly, D. D. Meyerhofer, and O. V. Gotchev, "A Model of Laser Imprinting," to be published in *Physics of Plasmas* (invited).

V. N. Goncharov, J. A. Delettrez, S. Skupsky, and R. P. J. Town, "Modeling Laser Imprint for Inertial Confinement Fusion Targets," to be published in *Physical Review Letters*.

K. Green and R. Sobolewski, "Extending the S-Parameter Approach to Linear Time-Varying Microwave Devices: Part I. Analysis," to be published in *IEEE Microwave Theory and Techniques*.

K. S. Il'in, M. Lindgren, M. Currie, A. D. Semenov, G. N. Gol'tsman, R. Sobolewski, S. I. Cherednichenko, and E. M. Gershenson, "Picosecond Hot-Electron Energy Relaxation in NbN Superconducting Photodetectors," to be published in *Applied Physics Letters*.

J. P. Knauer, R. Betti, D. K. Bradley, T. R. Boehly, T. J. B. Collins, V. N. Goncharov, P. W. McKenty, D. D. Meyerhofer, V. A. Smalyuk, C. P. Verdon, S. G. Glendinning, D. H. Kalantar, and R. G. Watt, "Single-Mode Rayleigh–Taylor Growth-Rate Measurements on the OMEGA Laser System," to be published in *Physics of Plasmas*.

C. K. Li, D. G. Hicks, F. H. Séguin, R. D. Petrasso, J. M. Soures, P. B. Radha, V. Yu. Glebov, C. Stoeckl, J. P. Knauer, R. Kremens, F. J. Marshall, D. D. Meyerhofer, S. Skupsky, S. Roberts, C. Sorce, T. C. Sangster, T. W. Phillips, and M. D. Cable, “D-³He Proton Spectra for Diagnosing Shell ρR and Fuel T_i of Imploded Capsules at OMEGA,” to be published in the *Journal of Plasma Physics*.

F. J. Marshall, J. A. Delettrez, R. Epstein, V. Yu. Glebov, D. R. Harding, P. W. McKenty, D. D. Meyerhofer, R. D. Petrasso, P. B. Radha, W. Seka, S. Skupsky, V. A. Smalyuk, J. M. Soures, C. Stoeckl, R. P. J. Town, B. Yaakobi, D. G. Hicks, C. K. Li, and F. H. Séguin, “Direct-Drive, High-Convergence-Ratio Implosion Studies on the OMEGA Laser System,” to be published in *Physics of Plasmas*.

F. J. Marshall, “Direct-Drive, Hollow-Shell Implosion Studies on the 60-Beam, UV OMEGA Laser System,” to be published in *Physics of Plasmas*.

R. L. McCrory, R. E. Bahr, T. R. Boehly, T. J. B. Collins, R. S. Craxton, J. A. Delettrez, W. R. Donaldson, R. Epstein, V. N. Goncharov, R. Q. Gram, D. R. Harding, P. A. Jaanimagi, R. L. Keck, J. P. Knauer, S. J. Loucks, F. J. Marshall, P. W. McKenty, D. D. Meyerhofer, S. F. B. Morse, O. V. Gotchev, P. B. Radha, S. P. Regan, W. Seka, S. Skupsky, V. A. Smalyuk, J. M. Soures, C. Stoeckl, R. P. J. Town, M. D. Wittman, B. Yaakobi, J. D. Zuegel, R. D. Petrasso, D. G. Hicks, and C. K. Li, “OMEGA Experiments and Preparation for Direct-Drive Ignition on the National Ignition Facility,” to be published in the *Proceedings of the 1999 Inertial Fusion Sciences and Applications Conference*, Bordeaux, France, 12–17 September 1999.

P. W. McKenty, M. D. Wittman, and V. N. Goncharov, “Characterization of Thick Cryogenic Fuel Layers Using Convergent-Beam Interferometry: a Numerical Investigation,” to be published in the *Journal of Applied Physics*.

P. B. Radha, S. Skupsky, R. D. Petrasso, and J. M. Soures, “A Novel Charged-Particle Diagnostic for Compression in ICF Targets,” to be published in *Physics of Plasmas*.

D. J. Smith, J. A. Warner, N. E. LeBarron, T. J. Kessler, S. LaDelia, J. P. Knauer, D. D. Meyerhofer, D. Oron, and D. Shvarts, “The Development of Ion-Etched Phase Plates,” to be published in *Applied Optics*.

R. Sobolewski, “Time-Resolved Nonequilibrium Phenomena in High-Temperature Superconductors,” to be published in the *Proceedings of the International Workshop on Superconductivity, Magneto-Resistive Materials, and Strongly Correlated Quantum Systems, Reccontres du Vietnam, June 1999* (invited).

J. M. Soures, R. L. McCrory, R. Betti, W. Bittle, T. R. Boehly, R. Boni, D. K. Bradley, T. J. B. Collins, R. S. Craxton, J. A. Delettrez, W. R. Donaldson, R. Epstein, V. Glebov, V. N. Goncharov, D. R. Harding, P. A. Jaanimagi, R. L. Keck, J. H. Kelly, T. J. Kessler, J. P. Knauer, C. K. Li, S. J. Loucks, F. J. Marshall, P. W. McKenty, D. D. Meyerhofer, S. F. B. Morse, S. Padalino, R. Petrasso, P. B. Radha, S. P. Regan, W. Seka, R. W. Short, A. Simon, S. Skupsky, D. J. Smith, R. P. J. Town, B. Yaakobi, and J. D. Zuegel, “Recent Advances in Direct-Drive ICF Target Physics at the Laboratory for Laser Energetics,” to be published in the *Proceedings of the 1998 IAEA Conference*, Yokohama, Japan, 19–24 October 1998.

E. A. Startsev and C. J. McKinstrie, “Relativistic Ponderomotive Dynamics of a Test Particle in a Plasma,” to be published in *Physical Review E*.

F.-Y. Tsai, E. L. Alfonso, S.-H. Chen, and D. R. Harding, “Mechanical Properties and Gas Permeability of Polyimide Shells Fabricated by the Vapor Deposition Method,” to be published in *Fusion Technology*.

B. Yaakobi, V. A. Smalyuk, J. A. Delettrez, R. P. J. Town, F. J. Marshall, V. Yu. Glebov, R. D. Petrasso, J. M. Soures, D. D. Meyerhofer, and W. Seka, “Spherical Implosion Experiments on OMEGA: Measurements of the Cold, Compressed Shell,” to be published in the *Proceedings of the 1999 Inertial Fusion Sciences and Applications Conference*, Bordeaux, France, 12–17 September, 1999.

Conference Presentations

J. L. Chaloupka and D. D. Meyerhofer, "Observation of Electron Trapping in an Intense Laser Beam," International Conference on Multiphoton Processes, Monterey, CA, 3–8 October 1999.

A. V. Okishev, M. D. Skeldon, J. H. Kelly, A. Babushkin, J. D. Zuegel, R. G. Roides, S. F. B. Morse, and W. Seka, "Front-End Laser System for the OMEGA Laser Fusion Facility," Optics '99, St. Petersburg, Russia, 19–21 October 1999.

The following presentations were made at the 13th Annual Target Fabrication Meeting, Catalina Island, CA, 8–11 November 1999:

E. L. Alfonso, I. Anteby, and D. R. Harding, "Temperature and Ice-Thickness Profiles Within Cryogenic ICF Targets."

M. Bonino, L. Elasky, R. Q. Gram, S. Noyes, and D. R. Harding, "Stress–Strain Performance of Spider Silk."

R. Q. Gram, J. Hobler, L. Lund, and D. R. Harding, "Initial Performance of the High-Pressure DT Filling Portion of the Cryogenic Target-Handling System."

P. W. McKenty and M. D. Wittman, "Characterization of Thick Cryogenic Layers Using an Interferometric Imaging System and Legendre Mode Decomposition."

F.-Y. Tsai, E. L. Alfonso, S.-H. Chen, and D. R. Harding, "Mechanical Properties and Gas Permeability of Polyimide Shells Fabricated by the Vapor Deposition Method."

The following presentations were made at the 41st Annual Meeting of the American Physical Society Division of Plasma Physics, Seattle, WA, 15–19 November 1999:

T. R. Boehly, O. Gotchev, V. N. Goncharov, J. P. Knauer, D. D. Meyerhofer, S. Skupsky, V. A. Smalyuk, R. P. J. Town, Y. Srebro, and D. Shvarts, "Measurements of Laser Imprinting on the OMEGA Laser System."

T. J. B. Collins and S. Skupsky, "The Effects of Pulse Shaping on Imprint."

R. S. Craxton and S. Skupsky, "Pulse Shapes and Beam Smoothing for OMEGA and the NIF."

J. A. Delettrez, V. Yu. Glebov, F. J. Marshall, C. Stoeckl, B. Yaakobi, and D. D. Meyerhofer, "Effect of Beam Smoothing and Pulse Shape on the Implosion of DD-Filled CH Shell Targets on OMEGA."

R. Epstein, J. A. Delettrez, V. N. Goncharov, P. W. McKenty, P. B. Radha, and S. Skupsky, "One-Dimensional Simulation of the Effects of Unstable Mix on Neutron and Charged-Particle Spectra from Laser-Driven Implosion Experiments."

V. Yu. Glebov, J. A. Delettrez, R. Epstein, P. W. McKenty, F. J. Marshall, D. D. Meyerhofer, P. B. Radha, V. A. Smalyuk, and C. Stoeckl, "Evidence for Fuel-Pusher Mixing in OMEGA Direct-Drive Implosions by Neutron Diagnostic."

V. N. Goncharov, S. Skupsky, P. W. McKenty, R. P. J. Town, T. R. Boehly, D. D. Meyerhofer, and O. V. Gotchev, "A Model of Laser Imprinting" (invited).

O. V. Gotchev, J. P. Knauer, D. D. Meyerhofer, and V. A. Smalyuk, "Characterization of an X-Ray Radiographic System for Measuring the Evolution of Broadband Imprint in Laser-Driven Planar Targets."

D. R. Harding, L. D. Lund, S. J. Loucks, D. J. Lonobile, R. Q. Gram, M. D. Wittman, M. J. Shoup III, G. Gerspacher, U. Kamal, L. Folsbee, A. Nobile, G. Besenbruch, K. Schultz, and I. Anteby, "The OMEGA Cryogenic Target-Handling System."

D. G. Hicks, C. K. Li, F. H. Séguin, R. D. Petrasso, J. M. Soures, C. Stoeckl, J. P. Knauer, D. D. Meyerhofer, W. Seka, R. W. Short, A. Simon, T. W. Phillips, T. C. Sangster, and M. D. Cable, "Measurement of Accelerated Ions from OMEGA Targets."

P. A. Jaanimagi, R. Boni, and R. L. Keck, "Neutron-Induced Background in CCD Detectors."

- A. V. Kanaev and C. J. McKinstrie, “Numerical Two-Dimensional Studies of Near-Forward Stimulated Brillouin Scattering of a Laser Beam in Plasmas.”
- D. Keller, T. J. B. Collins, J. A. Delettrez, P. W. McKenty, P. B. Radha, R. P. J. Town, B. Whitney, and G. A. Moses, “*DRACO*—A New Multidimensional Hydrocode.”
- J. P. Knauer, R. Betti, T. R. Boehly, V. N. Goncharov, D. D. Meyerhofer, and R. P. J. Town, “Feed-Out of Rear-Surface Perturbations to the Ablation Interface and Subsequent Growth.”
- M. V. Kozlov and C. J. McKinstrie, “Numerical Simulation of Sound-Wave Generation in Two-Ion Plasma.”
- C. K. Li, R. D. Petrasso, D. G. Hicks, F. H. Séguin, J. M. Soures, P. B. Radha, V. Yu. Glebov, J. P. Knauer, F. J. Marshall, S. Roberts, S. Skupsky, C. Sorce, C. Stoeckl, T. C. Sangster, T. W. Phillips, and M. D. Cable, “ $T\text{-}^3\text{He}$ Deuterons as a Diagnostic for Capsule Implosions on OMEGA.”
- V. Lobatchev and R. Betti, “Numerical Study of Feed-Out of Short-Wavelength Rear-Surface Perturbations in Planar Targets.”
- F. J. Marshall, J. A. Delettrez, R. Epstein, V. Yu. Glebov, D. R. Harding, P. W. McKenty, D. D. Meyerhofer, R. D. Petrasso, P. B. Radha, W. Seka, S. Skupsky, V. A. Smalyuk, J. M. Soures, C. Stoeckl, R. P. J. Town, B. Yaakobi, D. G. Hicks, C. K. Li, and F. H. Séguin, “Direct-Drive, High-Convergence-Ratio Implosion Studies on the OMEGA Laser System.”
- D. D. Meyerhofer, P. W. McKenty, V. N. Goncharov, J. A. Delettrez, V. Yu. Glebov, F. J. Marshall, P. B. Radha, S. P. Regan, V. A. Smalyuk, J. M. Soures, C. Stoeckl, R. P. J. Town, B. Yaakobi, and R. D. Petrasso, “Performance of Spherical Target Implosions on the OMEGA Laser System.”
- P. B. Radha, S. Cremer, J. A. Delettrez, R. Epstein, R. D. Petrasso, S. Skupsky, and J. M. Soures, “Charged-Particle Spectra Using Particle Tracking on a Two-Dimensional Grid.”
- S. P. Regan, J. A. Delettrez, D. K. Bradley, V. Yu. Glebov, D. D. Meyerhofer, and C. Stoeckl, “Burnthrough Experiments on OMEGA to Study Effects of Laser Irradiation Uniformity and Shinethrough Layers on Spherical Target Performance.”
- F. H. Séguin, R. D. Petrasso, C. K. Li, D. G. Hicks, J. M. Soures, P. B. Radha, V. Yu. Glebov, F. J. Marshall, D. D. Meyerhofer, C. Stoeckl, S. Roberts, C. Sorce, T. C. Sangster, T. W. Phillips, M. D. Cable, S. Padalino, and K. Fletcher, “Diagnostic Use of Secondary $D\text{-}^3\text{He}$ Proton Spectra for DD OMEGA Targets.”
- W. Seka, D. D. Meyerhofer, S. P. Regan, B. Yaakobi, R. E. Bahr, R. S. Craxton, R. W. Short, and A. Simon, “Interaction Experiments Under Direct-Drive NIF Conditions.”
- R. W. Short, “Stability of Self-Focused Filaments in Laser-Produced Plasmas.”
- A. Simon, “Relativistic Electron Beams, Forward Thomson Scattering, and Raman Scattering.”
- V. A. Smalyuk, B. Yaakobi, V. N. Goncharov, J. A. Delettrez, F. J. Marshall, and D. D. Meyerhofer, “Imaging of Compressed Pure-CH Shells and CH Shells with Titanium-Doped Layers on OMEGA.”
- E. A. Startsev and C. J. McKinstrie, “Particle-in-Cell Simulations of Particle Acceleration.”
- C. Stoeckl, J. A. Delettrez, V. Yu. Glebov, D. D. Meyerhofer, W. Seka, V. A. Smalyuk, S. Sublett, and J. D. Zuegel, “Measurements of Hard X-Ray Emission from Laser-Plasma Instabilities on OMEGA.”
- R. P. J. Town, J. A. Delettrez, R. Epstein, V. N. Goncharov, P. W. McKenty, P. B. Radha, and S. Skupsky, “OMEGA Cryogenic Target Design.”

UNIVERSITY OF
ROCHESTER